

AD-A203 354

10. FILE COPY

(1)

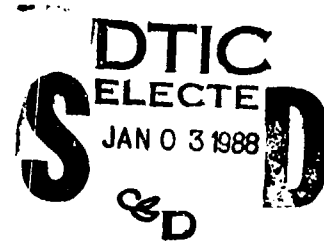
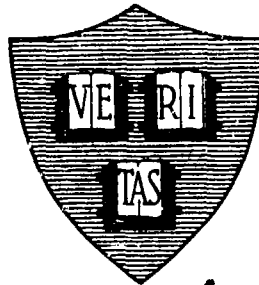
Office of Naval Research

Contract N00014-83-K-0383

Contract N00014-84-K-0465

National Sciences Foundation Grant DMR-84-04489

QUANTUM PHENOMENA IN  
MESOSCOPIC SUPERCONDUCTING TUNNEL JUNCTIONS



By

Marco Iansiti

December 1988

Technical Report No. 27

This document has been approved for public release and sale; its distribution is unlimited. Reproduction in whole or in part is permitted by the U.S. Government.

Division of Applied Sciences  
Harvard University · Cambridge, Massachusetts

89 1 03 062

Unclassified  
SECURITY CLASSIFICATION OF THIS PAGE (When Data Entered)

REPORT DOCUMENTATION PAGE		READ INSTRUCTIONS BEFORE COMPLETING FORM
1. REPORT NUMBER Technical Report No. 27	2. GOVT ACCESSION NO.	3. RECIPIENT'S CATALOG NUMBER
4. TITLE (and Subtitle) Quantum Phenomena in Mesoscopic Superconducting Tunnel Junctions		5. TYPE OF REPORT & PERIOD COVERED
		6. PERFORMING ORG. REPORT NUMBER
7. AUTHOR(s) Marco Iansiti		8. CONTRACT OR GRANT NUMBER(s) Contracts N00014-83-K-0383 N00014-84-K-0465, NSF Grant DMR-84-04489
9. PERFORMING ORGANIZATION NAME AND ADDRESS		10. PROGRAM ELEMENT, PROJECT, TASK AREA & WORK UNIT NUMBERS
11. CONTROLLING OFFICE NAME AND ADDRESS Division of Applied Sciences Harvard University Cambridge, MA 02138		12. REPORT DATE December, 1988
		13. NUMBER OF PAGES 184
14. MONITORING AGENCY NAME & ADDRESS (if different from Controlling Office)		15. SECURITY CLASS. (of this report) unclassified
		15a. DECLASSIFICATION/DOWNGRADING SCHEDULE
16. DISTRIBUTION STATEMENT (of this Report) Reproduction in whole or in part is permitted for any purpose of the United States Government. Approved for public release; distribution unlimited.		
17. DISTRIBUTION STATEMENT (of the abstract entered in Block 20, if different from Report)		
18. SUPPLEMENTARY NOTES		
19. KEY WORDS (Continue on reverse side if necessary and identify by block number)		
20. ABSTRACT (Continue on reverse side if necessary and identify by block number) We report a low temperature study of very small superconducting tunnel junctions. The samples were fabricated by using electron-beam lithography and thermal evaporation in single-junction, double-junction and eleven-junction-array configurations. The junctions had normal resistances between 0.5 and 140 $\Omega$ and areas between 0.1 and 0.02 $(\mu\text{m})^2$ . We measured the current-voltage characteristics of the devices at low temperatures (20 mK - 4 K), using a dilution refrigerator.		

DD FORM 1 JAN 73 1473

EDITION OF NOV 65 IS OBSOLETE  
S/N 0102-014-6601

SECURITY CLASSIFICATION OF THIS PAGE (When Data Entered)

TOP SECRET

In general, the devices had a large single electron charging energy  $E_C$  of order 1 K. By varying the ratio of  $E_C$  to the Josephson coupling energy  $E_J$ , we studied the crossover between the conventional Josephson regime, in which  $E_J \gg E_C$ , and the Coulomb blockade regime, in which charging effects are dominant. For comparable charging and Josephson energies the I-V curve is resistive at all currents, and exhibits a novel low-voltage resistance  $R_0$  at currents less than the critical current  $I_C$ . Moreover,  $I_C$  is greatly reduced when compared to conventional Josephson junction results, and scales at low temperatures with  $R_n^{-2}$ . If a magnetic field is applied to the junctions, reducing  $E_J$  so that  $E_J \ll E_C$ , we find a striking regime in which aspects of the Coulomb blockade of tunneling coexist with features typical of Josephson tunneling.

We develop a number of semiquantitative models which appear to explain the salient new features of our observations. In the high temperature regime, thermal activation and damping effects are very important, since  $E_C$  and  $E_J$  are only of order 1 K, and the experimental results are fitted by extending well established classical models. At low temperatures, however, quantum fluctuations of the phase appear to become much more important, as thermal fluctuations and quasiparticle damping freeze out. We then turn to quantum mechanical methods to analyze our measurements. We use the semiclassical WKB approach, valid in the low  $E_C/E_J$  limit (and extend it to regions nearer the  $E_C-E_J$  limit by a numerical method), to obtain estimates of  $R_0$  in reasonably good agreement with our measurements. Moreover, by assuming that  $I_C$  scales with the binding energy of the ground state phase wavefunction in the Josephson potential, we account for its experimental  $R_n^{-2}$  dependence. Finally, we use a charge-space model to provide a semiquantitative account of the measurements in the high  $E_C/E_J$  limit.

Identical to

SECRET

Accession For	
NTIS CRA&I	<input checked="" type="checkbox"/>
DTIC TAB	<input type="checkbox"/>
Unannounced	<input type="checkbox"/>
Justification	
By	
Distribution /	
Availability Codes	
Dist	Avail and/or Special
A-1	



**Office of Naval Research**

**Contract N00014-83-K-0383**

**Contract N00014-84-K-0465**

**National Sciences Foundation Grant DMR-84-04489**

**QUANTUM PHENOMENA IN  
MESOSCOPIC SUPERCONDUCTING TUNNEL JUNCTIONS**

by

**Marco Iansiti**

**Technical Report No. 27**

Reproduction in whole or in part is permitted for any purpose of the United States Government. Approved for public release; distribution unlimited.

**December 1988**

The research reported in this document was made possible through support extended the Division of Applied Sciences, Harvard University, by the Office of Naval Research, under Contracts N00014-83-K-0383, N00014-84-K-0465 and by the National Sciences Foundation Grant DMR-84-04489.

**Division of Applied Sciences  
Harvard University · Cambridge, Massachusetts**

## ABSTRACT

We report a low temperature study of very small superconducting tunnel junctions. The samples were fabricated by using electron-beam lithography and thermal evaporation in single-junction, double-junction and eleven-junction-array configurations. The junctions had normal resistances between 0.5 and 140 k $\Omega$  and areas between 0.1 and 0.02 ( $\mu\text{m}$ )<sup>2</sup>. We measured the current-voltage characteristics of the devices at low temperatures (20 mK - 4 K), using a dilution refrigerator.

In general, the devices had a large single electron charging energy  $E_c \equiv e^2/2C$  of order 1 K. By varying the ratio of  $E_c$  to the Josephson coupling energy  $E_J$ , we studied the crossover between the conventional Josephson regime, in which  $E_J \gg E_c$ , and the Coulomb blockade regime, in which charging effects are dominant. For comparable charging and Josephson energies the I-V curve is resistive at all currents, and exhibits a novel low-voltage resistance  $R_0$  at currents less than the critical current  $I_c$ . Moreover,  $I_c$  is greatly reduced when compared to conventional Josephson junction results, and scales at low temperatures with  $R_n^{-2}$ . If a magnetic field is applied to the junctions, reducing  $E_J$  so that  $E_J \ll E_c$ , we find a striking regime in which aspects of the Coulomb blockade of tunneling coexist with features typical of Josephson tunneling.

We develop a number of semiquantitative models which appear to explain the salient new features of our observations. In the high temperature regime, thermal activation and damping effects are very important, since  $E_c$  and  $E_J$  are only of order 1 K, and the experimental results are fitted by extending well established classical models. At low temperatures, however, quantum fluctuations of the phase appear to become much more important, as thermal fluctuations and quasiparticle damping freeze out. We then turn to quantum mechanical methods to analyze our measurements. We use the semiclassical WK3 approach, valid in the low  $E_c/E_J$  limit (and extend it to regions nearer the  $E_c \sim E_J$  limit by a numerical method), to obtain estimates of  $R_0$  in reasonably good agreement with

our measurements. Moreover, by assuming that  $I_c$  scales with the binding energy of the ground state phase wavefunction in the Josephson potential, we account for its experimental  $R_n^{-2}$  dependence. Finally, we use a charge-space model to provide a semiquantitative account of the measurements in the high  $E_c/E_J$  limit.

## TABLE OF CONTENTS

	page
ABSTRACT	iii
LIST OF FIGURES	viii
LIST OF TABLES	xi
CHAPTER ONE: INTRODUCTION	1
CHAPTER TWO: THEORETICAL OVERVIEW	11
2.1 The Josephson Hamiltonian	11
2.2 The Basic Hamiltonian $H_0$	13
2.2.1 $\phi$ - space solutions	14
2.2.2 $Q$ - space solutions	18
2.3 The Effect of Dissipation	21
2.3.1 The harmonic oscillator Lagrangian	22
2.3.2 The case of strictly linear dissipation	23
2.3.3 Microscopic model of dissipation in a Josephson junction	31
2.4 The Effect of the External Source	35
2.4.1 $\phi$ - space approach	35
2.4.2 $Q$ - space approach	37
2.5 The Classical Limit	39
2.5.1 The RCSJ model	40
2.6 Junction Dynamics	45
2.6.1 The classical regime	46
2.6.2 Effect of small thermal fluctuations	48
2.6.3 Effect of small quantum fluctuations	50

2.7	Summary	51
CHAPTER THREE: EXPERIMENTAL TECHNIQUES		52
3.1	Fabrication Techniques	52
3.1.1	Fabrication of contact pads	55
3.1.2	Electron-beam lithography: general concepts	58
3.1.3	Electron-beam lithography: junction patterning procedures	61
3.1.4	Evaporation procedures	66
3.2	Measurement Techniques	71
3.2.1	Mounting procedures	71
3.2.2	Measurement set-up	71
3.2.3	Low temperature considerations	75
CHAPTER FOUR: EXPERIMENTAL RESULTS		78
4.1	Basic Junction Characterization	78
4.1.1	Current-voltage characteristics	78
4.1.2	The junction critical currents	83
4.1.3	The junction resistances	86
4.1.4	Junction "intrinsic" capacitance	89
4.2	Measurements in a Magnetic Field	92
4.2.1	Field dependence of $I_c$ and $R_o$	92
4.2.2	Coexistence of Josephson tunneling and the Coulomb blockade	97
4.2.3	Normal-insulator-normal junction regime	103
4.3	Measurement of Eleven-Junction Array	107
4.4	Summary of Experimental Results	112



CHAPTER FIVE: DISCUSSION: THE CLASSICAL REGIME	113
5.1 Definition of the Basic Model	113
5.2 Failure of Standard Approaches	117
5.3 Extension of Standard Models	120
5.3.1 The role of damping in the classical case	120
5.3.2 The effect of thermal fluctuations on the critical currents	121
5.3.3 Classical estimates of $R_0$	126
5.4 Summary and First Conclusions	132
CHAPTER SIX: DISCUSSION: THE QUANTUM REGIME	133
6.1 Interpretation of the Resistance $R_0$	133
6.2 Interpretation of the Critical Current $I_c$	142
6.3 Analysis in $Q$ - space	147
6.4 Coexistence of Coulomb Blockade and Josephson Tunneling	150
CHAPTER SEVEN: CONCLUSIONS	153
REFERENCES	158
APPENDIX ONE: The Electron-Beam-Lithography System	163
APPENDIX TWO: A Schematic of the Computer-Controlled Data-Acquisition System	
ACKNOWLEDGEMENTS	

## LIST OF FIGURES

	page
Fig. 1.1 (a) Josephson junction schematic	2
(b) Josephson potential	2
Fig. 1.2 (a) Classic Josephson junction I-V curve	5
(b) The Coulomb blockade: NIN regime	5
(c) The Coulomb blockade: SIS regime	5
Fig. 1.3 Experimental I-V curve: regime of comparable $E_c$ and $E_J$	7
Fig. 1.4 Experimental I-V curve at intermediate magnetic fields	8
Fig. 1.5 Experimental I-V curve at high magnetic fields	9
Fig. 2.1 (a) Variational ground state energy values for the Josephson system	17
(b) Variational ground state wavefunctions	17
Fig. 2.2 Charging energy vs. $Q$	19
Fig. 2.3 Energy spectrum for the Josephson system:	20
Fig. 2.4 A very simple model for the thermal oscillator bath	25
Fig. 2.5 Sketch of the classical "bounce" trajectory	29
Fig. 2.6 The charge-space energy spectrum, including the effect of quasiparticles	34
Fig. 2.7 The tilted "washboard" potential	36
Fig. 2.8 The RCSJ model	41
Fig. 2.9 Sketch of the quasiparticle I-V response	43
Fig. 2.10 Sketch of the typical underdamped RCSJ model I-V response	47
Fig. 2.11 Sketch of thermally activated and tunneling escape mechanisms	49
Fig. 3.1 Outline of the fabrication process	54
Fig. 3.2 The liftoff technique	56

Fig. 3.3	Sketch of the contact pad pattern	57
Fig. 3.4	The electron beam exposure process	60
Fig. 3.5	Resist undercut profile and the photoresist "bridge"	62
Fig. 3.6	SEM field of view during sample exposure	65
Fig. 3.7	Scanning electron photograph of a single-junction sample	68
Fig. 3.8	Scanning electron photograph of an eleven-junction array	69
Fig. 3.9	Close-up of the eleven-junction array	70
Fig. 3.10	Sketch of the dilution refrigerator top-loading slug	72
Fig. 3.11	Sketch of measurement set-up	73
Fig. 3.12	Sketch of dilution refrigerator inner vacuum chamber set-up	74
Fig. 4.1	Low temperature I-V characteristic of a high resistance junction: coarse scales	80
Fig. 4.2	Low temperature I-V characteristic of a high resistance junction: fine scales	82
Fig. 4.3	$I_c$ vs. $T$ for a high resistance junction	84
Fig. 4.4	$I_c$ vs. $T$ for different samples	85
Fig. 4.5	$R_o$ vs. $T$ for a high resistance junction	87
Fig. 4.6	$R_o$ vs. $T$ for different samples	88
Fig. 4.7	$R_L$ vs. $T$ for a typical sample	90
Fig. 4.8	$R_L(0)$ vs. $R_n$	91
Fig. 4.9	Typical $I_c$ vs. $H$ curve	93
Fig. 4.10	Low temperature $I_c$ vs. $T$ , for different magnetic field values	95
Fig. 4.11	Low temperature $R_o$ vs. $T$ , for different magnetic field values	96
Fig. 4.12	Sequence of I-V curves for a high resistance sample, taken at fixed temperature, for different magnetic fields	98
Fig. 4.13	Sequence of I-V curves for a high resistance sample, taken at	

fixed field, for different temperatures	99
Fig. 4.14 Measured "blockade voltage" $V_b$ vs. sample area	101
Fig. 4.15 Threshold fields $H_1$ and $H_{12}$ vs. $T$	102
Fig. 4.16 Gap voltage $V_g$ vs. $H$	104
Fig. 4.17 $dV/dI$ vs. $V$ , for different magnetic field values	106
Fig. 4.18 Low temperature I-V characteristic of the eleven-junction array	108
Fig. 4.19 $I_c$ vs. $T$ for the eleven-junction array	109
Fig. 4.20 Low temperature $I_c$ vs. $T$ for the eleven-junction array, for different magnetic field values	111
Fig. 5.1 Schematic of the basic model used	114
Fig. 5.2 Comparison of measured and predicted $I_c$ vs. $T$ , for a typical sample	122
Fig. 5.3 Sketch of the effect of large thermal fluctuations on $I_c$ and $I_r$	124
Fig. 5.4 Comparison of measured and predicted $R_0$ vs. $1/T$ , for a low resistance sample	129
Fig. 5.5 Comparison of measured and predicted $R_0$ vs. $T$ , for a high resistance sample	131
Fig. 6.1 Comparison of measured low temperature $R_0$ values with predictions from WKB and numerical estimates	135
Fig. 6.2 Model potentials used in the numerical estimate for $R_0$	137
Fig. 6.3 Comparison of escape rates calculated numerically and with the WKB formula	139
Fig. 6.4 Comparison of measured $R_0$ vs. $T$ , with quantum mechanical $T=0$ estimate	141
Fig. 6.5 Comparison of low temperature $I_c$ vs. $R_n$ with theoretical estimates	145
Fig. 6.6 Comparison of low temperature $I_c$ vs. $E_c/E_J$ with theoretical estimates	146

Fig. 6.7	Josephson junction energy spectrum, in the large $E_C/E_J$ limit	148
Fig. 7.1	Configuration of Fulton and Dolan's three terminal experiment	156
Fig. 7.2	Possible alternate Josephson three terminal device	156

#### LIST OF TABLES

Table 4.1:	Sample parameters	79
------------	-------------------	----

## CHAPTER ONE

### INTRODUCTION

One of the main technical trends in the twentieth century has been towards miniaturization. Physicists and engineers have sought to decrease the size of their devices to permit an increase in their complexity and flexibility. As the characteristic size of a device decreases, new physical phenomena are sometimes discovered which give rise to new applications, and illuminate fundamental physical questions.

Due to the technical breakthroughs of electron-beam lithography and dilution refrigeration, it has now become possible to study devices of such small size that their behavior is affected by the quantum mechanical properties of single electrons. An example is the measurement of the Aharonov-Bohm effect and of quantum conductance fluctuations due to the interference of electron wavefunctions, observed in metallic wires and semiconducting devices [see, for example, Umbach, *et al.*, 1984; Skocpol *et al.*, 1986; Lee *et al.* 1987]. A second example is the observation of discrete electronic states in small "zero dimensional" GaAs quantum well structures known as "quantum dots" [Reed *et al.*, 1988]. These systems are *mesoscopic*: while they are composed of a macroscopic number of particles, they are small enough so that their behavior is directly associated with microscopic phenomena.

This work is an experimental study of mesoscopic Josephson junctions. A Josephson junction is composed of two superconducting electrodes separated by an insulating barrier, as shown schematically in Fig. 1.1(a). Since the early 1960's, when the first theoretical predictions and experimental observations were made, this system has been well studied both theoretically and experimentally [see, for example, Tinkham, 1975, and Barone and Paterno, 1982]. The Josephson junction, in its usual configurations, is now well understood, and models have been developed which successfully predict its behavior. The most important variable which describes the system is the phase difference  $\phi$

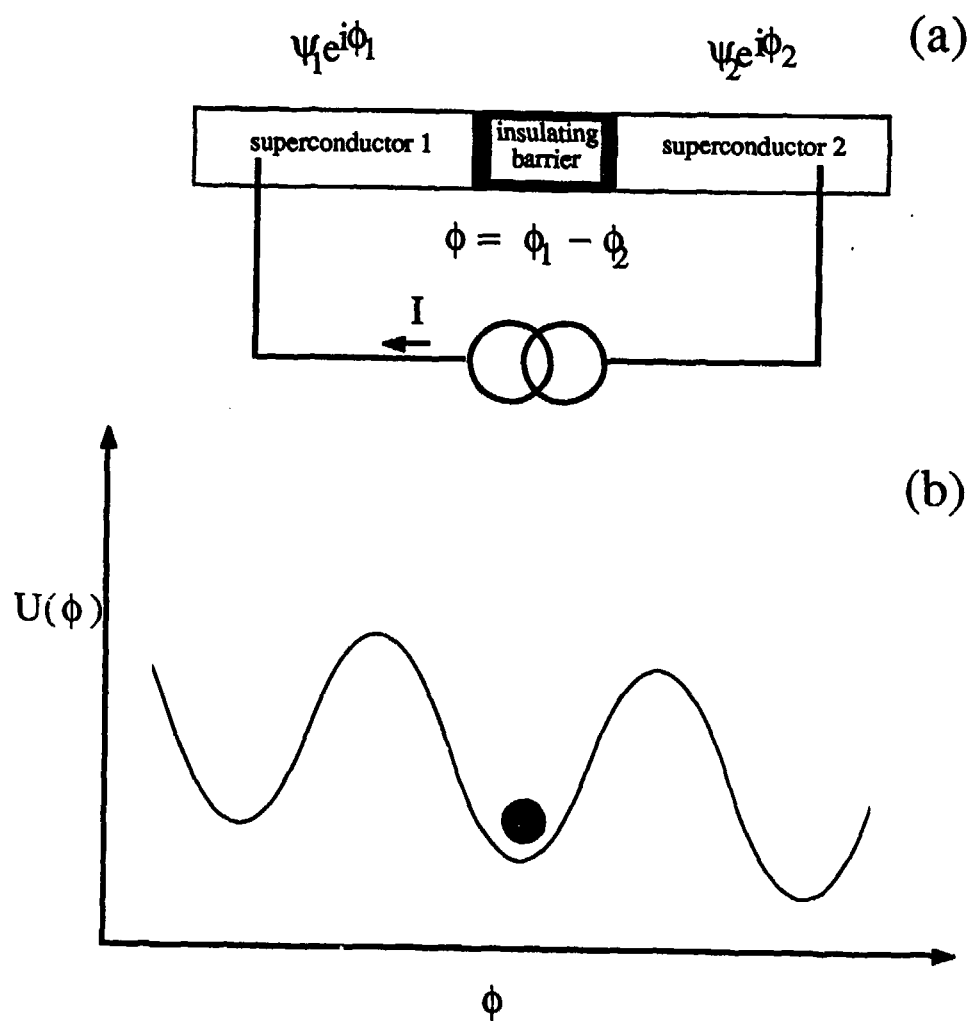


Figure 1.1: (a) Schematic of a Josephson junction and current biasing scheme. (b) The Josephson potential:  $U(\phi) = -E_J \cos \phi - (\hbar/2e) I \phi$ .

between the superconducting wavefunctions describing the two junction electrodes. The two electrodes are coupled, with characteristic energy  $E_J$ , as the two wavefunctions overlap near the barrier, resulting in the Josephson effect.  $E_J = (\hbar/8e^2)(\Delta/R_N)$ , at low temperatures, for an ideal junction, where  $\Delta$  is the superconducting energy gap, and  $R_N$  is the normal resistance.  $\phi$  is a *macroscopic* variable, describing the behavior of a large system, since the phase of each wavefunction is associated with the whole macroscopic superconducting electrode.  $\phi$  has a quantum mechanical conjugate:  $Q$ , the Cooper pair charge difference between the superconducting electrodes. The characteristic energy associated with the charge is the single electron charging energy  $E_C$ , the capacitive energy associated with a difference of one electron across the junction barrier.  $E_C = e^2/2C$  where  $C$  is the capacitance. In conventional Josephson devices,  $E_J \gg E_C$ , and the junction behavior is well described by semiclassical models.

The contribution of this thesis to the extensive literature on Josephson devices is in understanding some of the novel physical phenomena encountered when the single electron charging energy is made comparable to the Josephson energy. Our study is based on low temperature measurements of the current-voltage (I-V) characteristics of high resistance, low capacitance Josephson junctions, with  $E_C$  of order  $E_J$ . If  $E_C \sim E_J$ , the system can no longer be described by well known macroscopic physics, since a single electron transfer contributes a very significant energy change. On the other hand, if  $E_J$  is still significant, the macroscopic phase difference  $\phi$  plays a role in the system's behavior. The Josephson junction is then a mesoscopic system.

The dynamics of a Josephson device, in its simplest form, may be described by a hamiltonian  $H_0$ , which is a function of the phase difference  $\phi$  between the wavefunctions of the two electrodes, and the charge  $Q$  transferred between the electrodes. Ignoring dissipation, we write



$$H_o(\phi, Q) = E_c \frac{Q^2}{2} - E_J \cos \phi \quad (1)$$

The effect of a current bias can be incorporated by adding a term equal to  $-(\hbar/2e)I\phi$ , where  $I$  is the bias current. For conventional junctions, the dominant energy in the problem is the Josephson coupling energy and the most important term in  $H(\phi, Q)$  is the one associated with  $E_J$ . The dynamics of the problem at low currents are then simply obtained by the minimization of energy by a classically well-defined  $\phi$  value at a minimum of a well of the tilted cosinusoidal potential shown in Fig. 1.1 (b). The phase  $\phi$  is thus "trapped" in a potential well until the tilt imposed on the Josephson potential by the current bias is enough to allow it to escape. This results in the I-V characteristic features shown in Fig. 1.2(a); a zero resistance branch at low currents, and a very sharp jump to the dissipative voltage state at a critical current  $I_c$ .

In recent years, by fabricating granular films or very small tunnel junctions, it has been possible to study devices in which the charging energy is dominant over the other energies of the system (such as  $k_B T$  or  $E_J$ ). [Giaever and Zeller, 1968; Lambe and Jaklevic, 1969; Cavicchi and Silsbee, 1985 and 1988; Barner and Ruggiero, 1987; Fulton and Dolan, 1987; van Benthum *et al.*, 1988.] This has been achieved in samples with both normal and superconducting electrodes. In normal samples, a typical low temperature I-V response is shown in Fig. 1.2(b). At low voltages charge is trapped, and the resistance is very high, until the system acquires enough energy from the biasing source to enable an electron to tunnel to the other electrode. At this point ( $V \approx e/2C$ ) the dynamic resistance decreases producing a knee in the I-V curve. This effect is known as the "Coulomb blockade".

Fulton and Dolan [1987] observed a similar effect in superconducting samples in which the charging energy is much larger than the Josephson coupling energy. As a result the knee at  $V \approx e/2C$  is superimposed on the superconducting energy gap, as shown

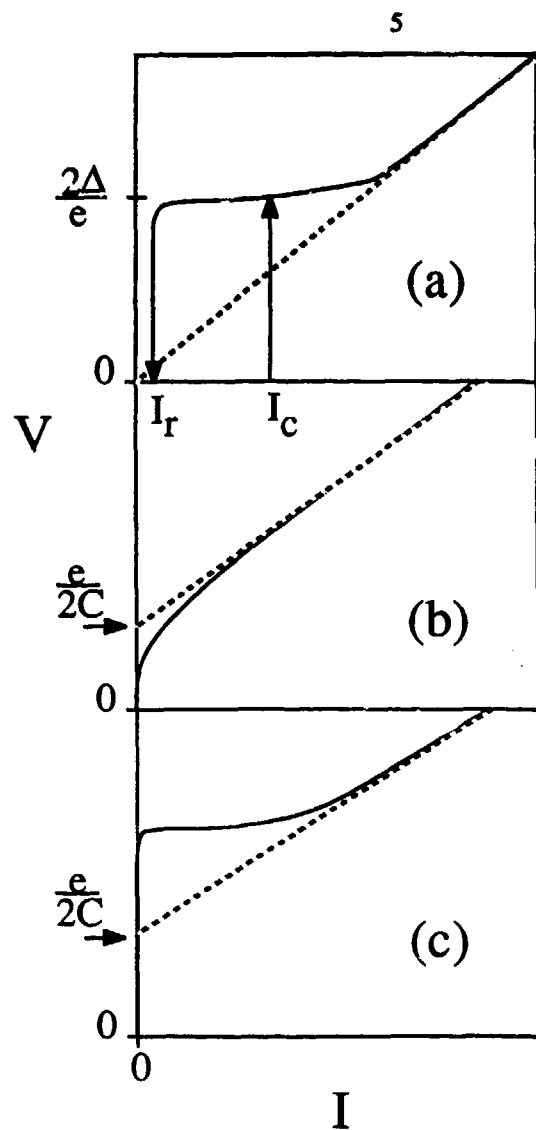


Fig. 1.2: Schematics of typical tunnel junction I-V characteristics: (a) underdamped superconductor-insulator-superconductor tunnel junction with  $E_J \gg E_c, k_B T$ . (b) normal-insulator-normal tunnel junction with  $E_c \gg k_B T$ . (c) superconductor-insulator-superconductor tunnel junction with  $E_c \gg E_J, k_B T$ .

schematically in Fig 1.2(c). In a broad sense, this effect is *conjugate* to the Josephson effect described above. In conventional devices  $\phi$  is a "well defined" semiclassical variable, while  $Q$  is ill defined. When the charging energy is dominant and the Josephson coupling energy is insignificant, quantum fluctuations in  $\phi$  are very large and the quantum mechanical conjugate  $Q$  may now be treated classically. The resulting dynamics are very different: the zero resistance branch up to  $I=I_c$  of the Josephson effect I-V curve is replaced by a very high resistance branch with no critical current.

Our study explores the crossover region *between* the two extremes described above. [Iansiti *et al.* 1987a, 1987b, 1988a, and 1988b.] By varying the ratio  $x=E_c/E_J$ , we sweep from a regime in which the Josephson coupling energy is large, well into the regime in which the charging energy appears to dominate. Experimentally, we have achieved this in two different ways: First, we have constructed samples of different areas and oxide barrier thicknesses, which has allowed us to go from  $E_c/E_J \approx 1/100$  to  $E_c/E_J \approx 10$ . Second, we have further decreased  $E_J$  by applying a magnetic field, which has enabled us to study the system with  $x$  values in principle approaching infinity, as  $E_J \rightarrow 0$ .

If the Josephson energy is much larger than  $e^2/2C$ , we obtain results typical of conventional Josephson devices. As the Josephson and charging energy become of comparable magnitude, however, we observe two novel regimes. First, we find that as  $E_J$  becomes of order  $E_c$ , the critical current is greatly reduced and the I-V curve becomes resistive, even at very low bias currents, as shown in Fig. 1.3. Second, if the Josephson coupling is reduced further by applying a magnetic field, we observe the new type of I-V curve shown in Fig. 1.4. The striking feature is the *coexistence* of a plateau beginning at  $V=e/2C$ , reminiscent of Coulomb blockade measurements made on samples in which  $E_c$  is completely dominant, with other features common to Josephson tunneling, such as a sharp jump from the plateau voltage to the superconducting energy gap voltage at a "critical current"  $I_c$ . If the magnetic field is increased further, the electrodes become normal, and we observe the Coulomb blockade I-V characteristic shown in Fig. 1.5.

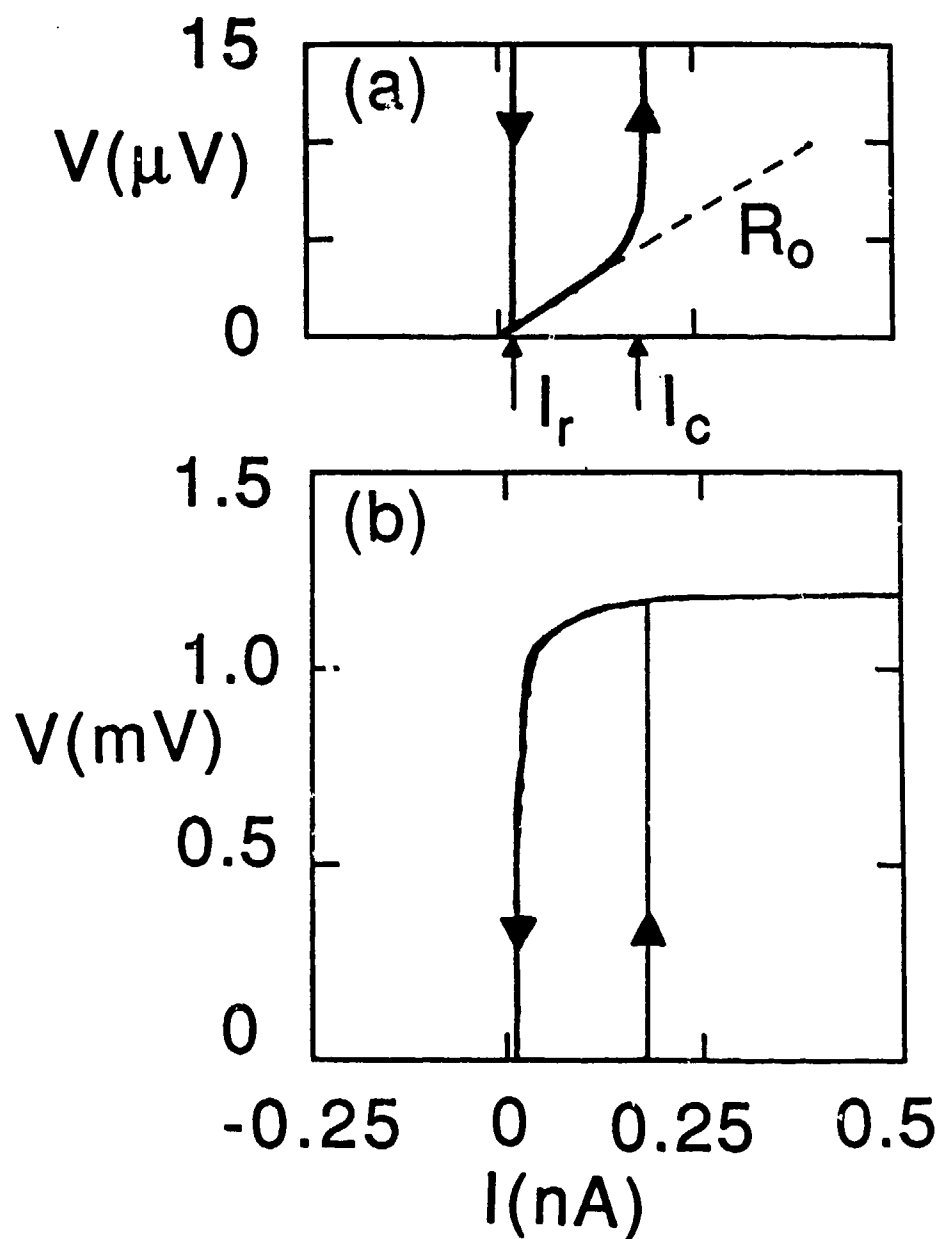


Fig. 1.3: I-V curve of a sample with  $R_n = 70 \text{ k}\Omega$  and estimated capacitance  $C \approx 1 \text{ fF}$ , taken at  $T=0.98\text{K}$  and  $H=0$ , showing definitions of  $I_c$ ,  $I_r$ , and  $R_0$ . Parts (a) and (b) have the same horizontal scale but different vertical scales.

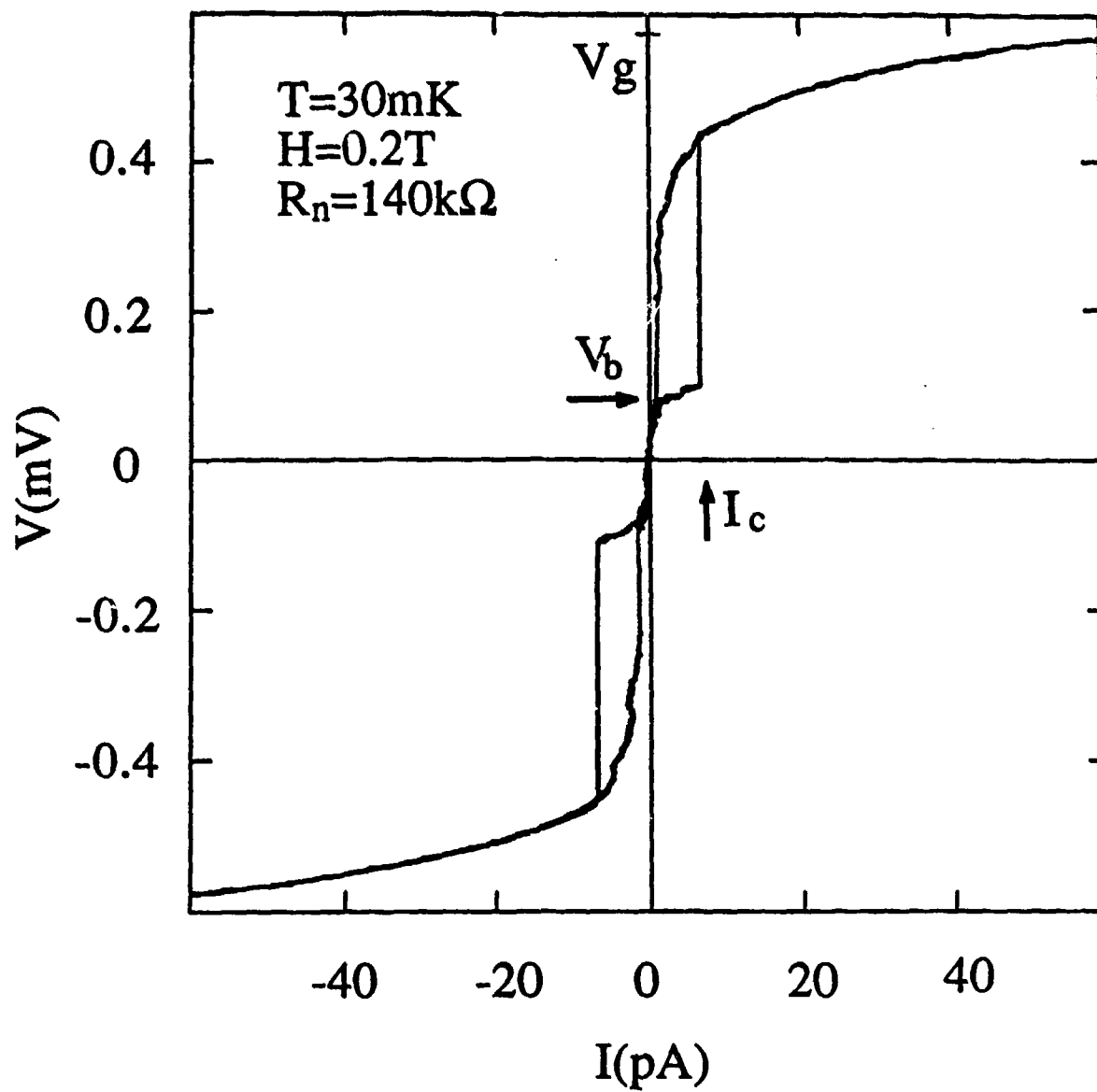


Fig. 1.4: I-V characteristic of a single Josephson junction with  $R_n = 140\text{k}\Omega$  and estimated  $C \approx 1\text{fF}$  taken in a magnetic field of 0.2 tesla at  $T=30\text{mK}$ .

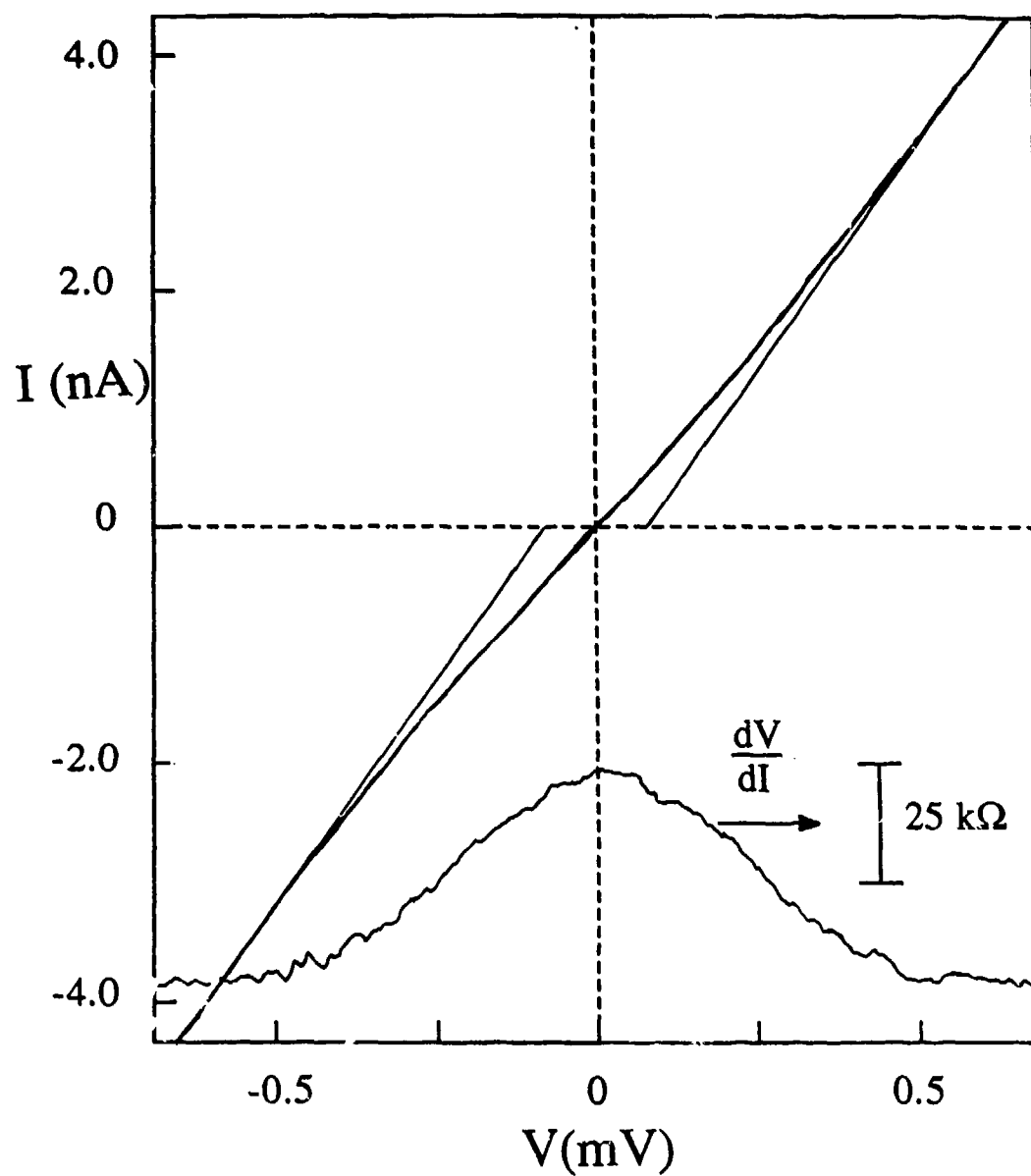


Fig. 1.5: I-V characteristic of a single Josephson junction with  $R_n = 140 \text{ k}\Omega$  and estimated  $C \approx 1 \text{ fF}$  taken in a magnetic field of 1.2 tesla, at  $T = 30 \text{ mK}$ .

In this report, we discuss these observations, and explore their interpretation in some detail. We begin in Chapter 2 by providing some theoretical background necessary to discuss our experimental results. An account of the methods used in the fabrication and measurement of the samples is given in Chapter 3. Next, in Chapter 4, we describe our experimental results. We then discuss a few simple models which we have used in their interpretation: We first examine the semiclassical models used in interpreting earlier work in Chapter 5 to see to what extent they can explain the new data by simply taking account of the new parameter regimes involved. Second, in Chapter 6, we investigate to what extent the introduction of a more fully quantum mechanical picture, including large quantum uncertainties in  $\phi$  space, can account for the remaining features. We conclude in Chapter 7.

## CHAPTER 2

### THEORETICAL OVERVIEW

This chapter develops some theoretical tools that will be used extensively in the discussion sections of this report, in Chapters 5 and 6. We write down and justify a Hamiltonian which includes the different components that are necessary for a description of Josephson junction dynamics: Josephson tunneling, quasiparticle tunneling and the effect of the environment, charging effects, and the effect of an external biasing source. We then examine some simple consequences of the Hamiltonian description in the quantum mechanical and classical limits.

#### 2.1 The Josephson Hamiltonian

The Josephson junction is described by the two quantum mechanical conjugate variables  $\phi$  and  $Q$ .

$$[\phi, Q] = 2ie \quad (2.1)$$

As described in Chapter 1,  $\phi$  is the phase difference between the superconducting wavefunctions on each electrode, and  $Q$  is the charge difference across the junction. In visualizing the problem, it is useful to establish a comparison with mechanics: using an appropriate normalization, we can treat  $\phi$  as the position variable  $X$ , and  $Q$  as the momentum variable  $P$ . The role of the system mass  $M$ , is then played by the capacitance  $C$ .

$$\phi \leftrightarrow X, \quad (h/2e) Q \leftrightarrow P, \quad (h/2e)^2 C \leftrightarrow M, \quad (2.2)$$



The Josephson junction Hamiltonian  $H_0$ , discussed in Chapter 1,

$$H_0(\phi, Q) = E_c \frac{Q^2}{2} - E_J \cos \phi \quad (2.3)$$

can then be simply mapped into the Hamiltonian

$$H(X, P) = \frac{P^2}{2M} + V(X) \quad (2.4)$$

The charging energy term in (2.3) then plays the role of a *kinetic energy* term, while the Josephson term plays the role of the *potential energy*.

To provide a more complete description of the system, it is necessary to incorporate other important factors. First of all,  $\phi$  is a macroscopic variable, since it is given by the difference in phase between the superconducting wavefunctions associated with each macroscopic junction electrode. Therefore,  $\phi$  is coupled to the "environment", made up of a large number of degrees of freedom. In the mechanical analog, the system loses energy by friction. This friction-like term may strongly affect the dynamics of the system, and must therefore be incorporated in the discussion. Following an approach pioneered by Caldeira and Leggett [Caldeira and Leggett 1981, 1983] the effect of the environment can be included in the Hamiltonian by adding an additional term  $H_e$ .

Finally, in order to measure the system, we need to excite it with a measuring current, produced by an external source. The external current source can be added to the system by adding another term to the Hamiltonian which we call  $H_s$ .

The complete Hamiltonian is then given by

$$H(\phi, Q) = H_0 + H_e + H_s \quad (2.5)$$

This chapter is devoted to a more detailed discussion of the origin of the different terms in (2.5), and of their effect on the dynamics of the system.

## 2.2 The Basic Hamiltonian $H_0$

The most basic Josephson junction Hamiltonian  $H_0$ , given above by (2.3), is composed of two terms. The first term, equal to  $Q^2/2C$ , represents the capacitive charging energy associated with a charge difference\*  $Q$  between the electrodes.

If we study a tunnel junction whose electrodes are superconducting, we must add a second term to the Hamiltonian. The right and left electrodes can be described by the complex wavefunctions  $\Psi_R$  and  $\Psi_L$ . If the two wavefunctions overlap there will be an energy term due to their interference, given by

$$\begin{aligned}\Delta E &= -(\text{constant}) (\Psi_R \Psi_L^* + \Psi_L \Psi_R^*) \\ &= -(\text{constant}) |\Psi_R \Psi_L| \cos \phi \\ &= -E_J \cos \phi\end{aligned}$$

The value of the Josephson energy  $E_J$  was calculated by Ambegaokar and Baratoff [1963], and is equal to, for an ideal tunnel junction,

$$E_J = \frac{\hbar \Delta}{8 e^2 R_n} \tanh\left(\frac{\Delta}{2 k_B T}\right) \quad (2.6)$$

---

\* By "charge difference" we mean the difference in charge on one electrode between the present state of the system and the neutral state.

If we incorporate the charging and Josephson terms in the description of the Josephson system we thus arrive to the basic Hamiltonian  $H_0$  given in (2.3).

### 2.2.1 $\phi$ space solutions

To express (2.3) in  $\phi$  space, taking account of the quantum nature of the phase-number relationship described by (2.1), we make the operator replacement  $Q \rightarrow 2ie \partial/\partial\phi$ , and obtain

$$H = -E_J \cos \phi - 4E_C \partial^2/\partial\phi^2 \quad (2.7)$$

where, again,  $E_C = e^2/2C$ . We see that the parameter  $x \equiv E_C/E_J$  provides a measure of the relative importance of the charging energy in forcing a delocalization of the phase, away from the minimum potential energy point at  $\phi = 0$ . Physically, this reflects the uncertainty relation between phase and particle number (or charge):

$$\Delta\phi \Delta N \geq 1 \quad (2.8)$$

where  $N = Q/e$ . For  $x \ll 1$  the ground state is a narrowly peaked wavefunction  $\psi(\phi)$  with width of order  $x^{1/4}$ , and there are many higher states in each minimum, resembling the excited states of a harmonic oscillator. By contrast, when  $x \gg 1$ , the term in  $E_C$  is dominant, and  $\psi$  approaches a constant to minimize it. At this point, one should no longer ignore the periodicity of the potential term  $-E_J \cos \phi$  and the question of whether  $\phi$  should be viewed as an extended variable, or a cyclic one such that  $\phi$  and  $\phi + 2\pi$  (or  $4\pi$ , if we include quasiparticles<sup>§</sup>) are physically indistinguishable. From the former point of view,  $\psi(\phi)$  has the form of a Bloch function  $u(\phi) e^{iq\phi}$ , where  $u(\phi)$  is periodic with period  $2\pi$ ;

---

<sup>§</sup> See, for example, Ambegaokar, Eckern, and Schön [1984].

from the latter point of view,  $\psi(\phi)$  is only defined between  $-\pi$  and  $+\pi$ , and it must satisfy appropriate boundary conditions at those points. So long as we restrict our attention to the ground state, which we expect to correspond to  $q = 0$  in the Bloch picture, and to the boundary conditions  $\psi(\pi) = \psi(-\pi)$  and  $\psi'(\pi) = \psi'(-\pi) = 0$  in the single cell picture, both pictures yield the same eigenvalue problem, and the same energy eigenvalue  $E$ .

Since this problem is one-dimensional, it is easy to solve by numerical means. However, one obtains more insight by a variational approach, using trial functions appropriate to the limiting cases of  $x \ll 1$  and  $x \gg 1$ , respectively. For  $x \ll 1$ , one assumes a Gaussian trial function,

$$\psi(\phi) \sim e^{-\frac{\phi^2}{4\sigma^2}} \quad (2.9)$$

where  $\sigma$ , the rms spread in  $\phi$ , is chosen to minimize the expectation value of (2.9). The resulting minimum energy is

$$E = -E_J e^{-\frac{\sigma^2}{2}} \left(1 - \frac{\sigma^2}{2}\right) \quad (2.10)$$

where  $\sigma$  has the value determined by the solution of the transcendental equation

$$\sigma^4 = e^{-\frac{\sigma^2}{2}} = 2x \quad (2.11)$$

For  $x \ll 1$ , (2.11) leads to the analytic approximation

$$E = -E_J [1 - (2x)^{1/2}] \quad (2.12)$$

In the other limiting case of  $x \gg 1$ , an appropriate trial function which satisfies the boundary conditions at the edge of the cell is

$$\psi(\phi) \sim (1 + a \cos \phi) \quad (2.13)$$

Minimization of the expectation value of the energy with respect to the parameter  $a$  leads to the condition that

$$a = 4x[(1 + 1/8x^2)^{1/2} - 1] \quad (2.14)$$

For this value of  $a$ , the energy is

$$E = -E_J 2x [(1 + 1/8x^2)^{1/2} - 1] \quad (2.15)$$

For  $x \gg 1$ , this has the limiting form

$$E \approx -E_J/8x = -E_J^2/8E_c \quad (2.16)$$

where the second form shows explicitly that in this limit the binding energy is *second order* in  $E_J$ , in contrast to binding energy in the classical limit, which is *first order* in  $E_J$ , since  $E = -E_J$ .

These variational approximations to the ground state energy are plotted in Fig. 2.1(a). The tight-binding approximation (2.9) gives a lower (more accurate) energy for  $x < 1/4$ , and the weak-binding approximation (2.13) gives a better energy for  $x > 1/4$ . Numerical solutions in the cross-over region near  $x = 1/4$  show that the exact binding energy exceeds the better of the two approximations by less than 5%, even in the worst case. The wave functions  $\psi(\phi)$  for values of  $x$  ranging from 0.05 to 1 are shown in Fig.

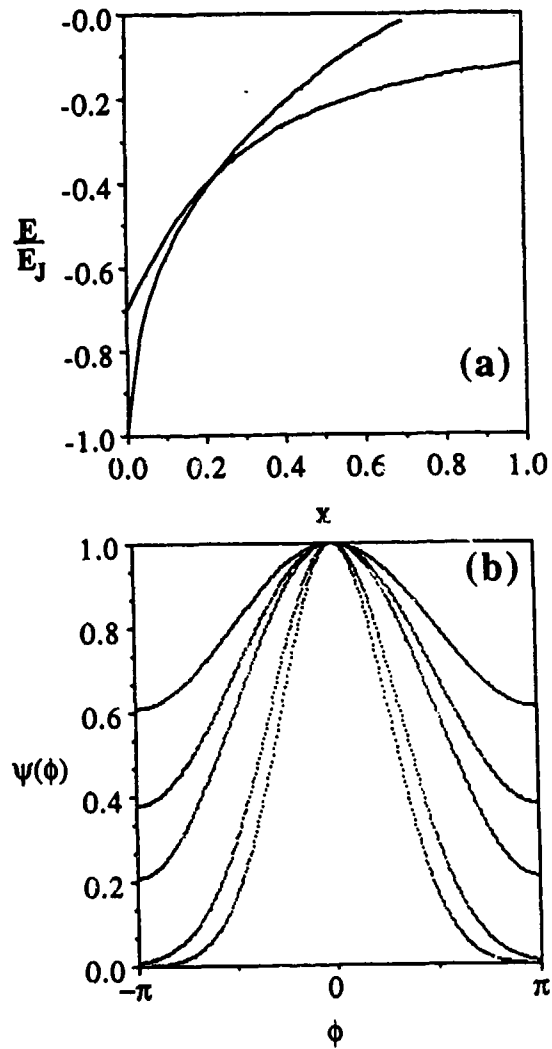


Fig. 2.1: (a) Estimated binding energy  $E$  vs.  $x = E_c/E_J$ . The two curves correspond to two different trial wavefunctions, as outlined in the text. (b) Estimated ground state wavefunction  $\psi(\phi)$  as a function of  $\phi$ , for different values of  $x$ . From top to bottom the curves correspond to  $x = 1, 0.5, 0.3, 0.1, 0.05$ .

2.1(b). In this figure, the loose-binding approximation is shown for  $x > 1/4$  and the tight-binding approximation for  $x < 1/4$ . Qualitatively, it is clear that for  $x > 1/4$ , the probability density for the phase variable  $\phi$  is sufficiently delocalized that it is no longer a good approximation to treat  $\phi$  as a semiclassical variable.

### 2.2.2 Q-space solutions

To investigate the regime in which  $E_c > E_J$ , it is convenient to express the problem as a function of the charge variable  $Q$ . In the  $E_c \gg E_J$  limit, quantum phase fluctuations become very large while  $Q$  can be treated classically. Moreover, by going to Q-space, and assuming Bloch-function solutions to the Hamiltonian (2.3) we automatically take care of the  $2\pi$  phase periodicity of the Josephson potential.

We will first examine the regime in which the charging energy is dominant over  $E_J$ . A plot of the charging term in the Hamiltonian ( $Q^2/2C$ ) as a function of  $Q$  is shown in Fig. 2.2. The voltage across the junction is given by  $V = dE/dQ$ . To model single electron tunneling we can for the moment include in the system a second mechanism which is able to transfer electrons from one side to the other in lumps equal to the electron charge  $e$ . Due to the discreteness of the charge transfer, two types of transitions are possible, indicated in Fig. 2.2 by (1) and (2). If the initial  $Q$  is less than  $e/2$  ( $V < e/2C$ ), as in (1), the transition is energetically unfavorable. If the initial  $Q$  is larger than  $e/2$ , the transition is favorable. If we add charge to this system in a continuous fashion, by attaching highly resistive leads, we have the following situation. For  $V < e/2C$ , electron tunneling is discouraged and the dynamic resistance of the device is high. For  $V > e/2C$ , the tunneling process becomes energetically favorable and the dynamic resistance decreases. The resulting I-V characteristics of the device are then those typical of the Coulomb blockade, shown in Fig. 1.1(a) and 1.4.

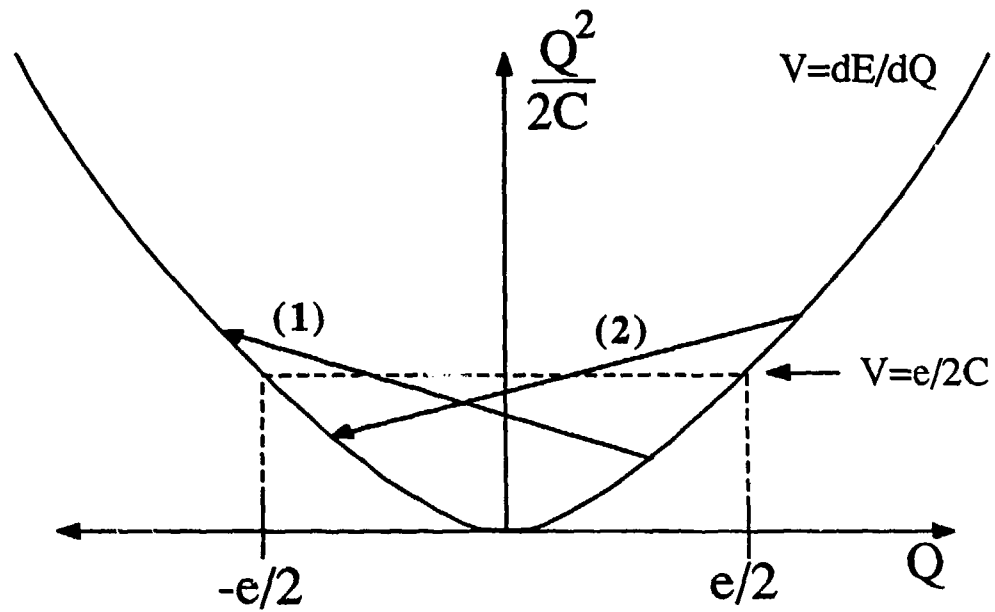


Fig. 2.2: Energy stored on a Normal - Insulator - Normal junction as a function of charge  $Q$ . The two arrows indicate changes in  $Q$  of magnitude  $e$ , corresponding to having one electron tunnel from one electrode to the other. For  $Q < e/2$ , this transition is not energetically favored. For  $Q > e/2$  it is energetically favored. Adapted from Averin and Likharev [1986].



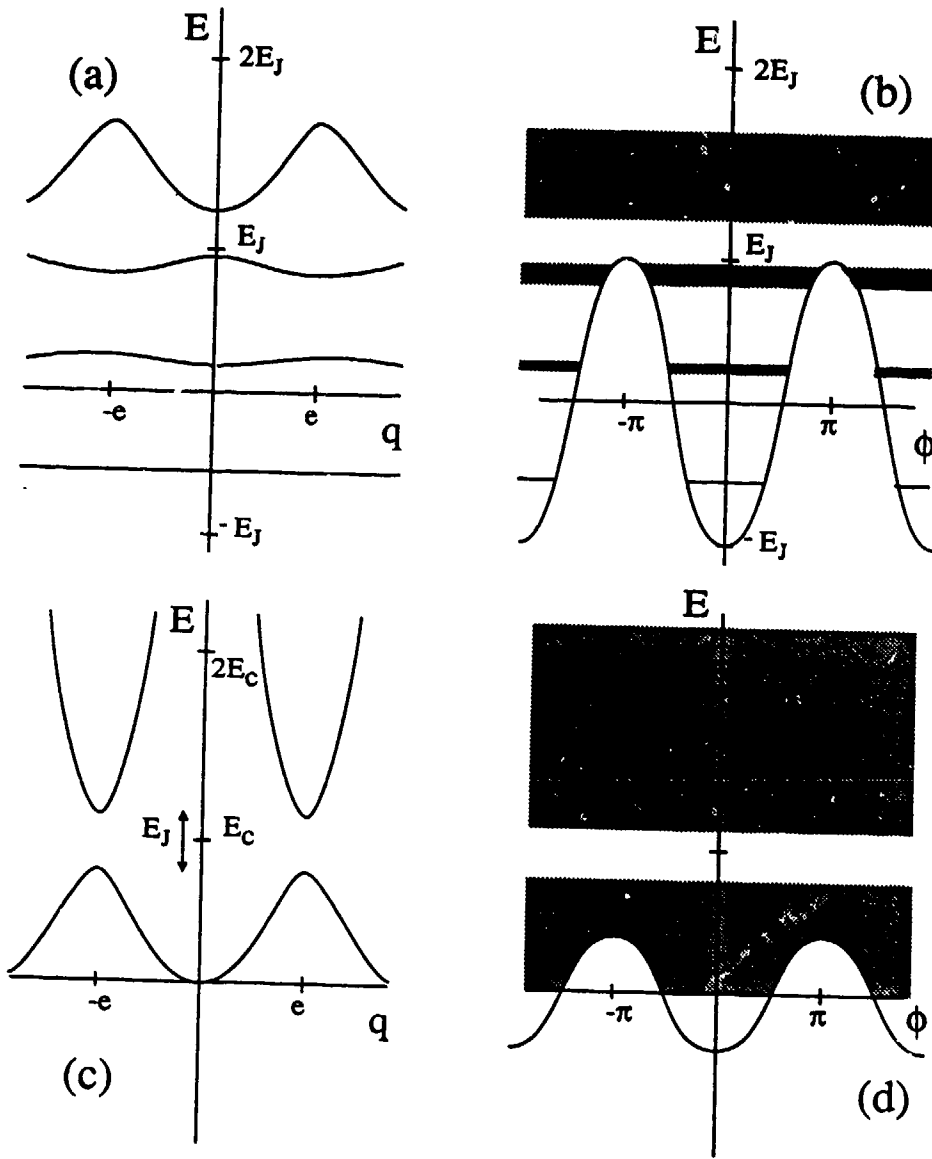


Fig. 2.3: Energy spectrum of a Josephson junction, plotted in  $\phi$ - and  $q$ -space: (a)  $q$ -space,  $x = 0.1$ . (b)  $\phi$ -space,  $x = 0.1$ . (c)  $q$ -space,  $x = 2.5$ . (d)  $\phi$ -space,  $x = 2.5$ .

If we now put the Josephson potential term in the Hamiltonian, postponing the further treatment of single electron effects to Section 2.3, the energy spectrum of the Josephson device then assumes a band-like structure, reminiscent of that of a one dimensional crystal. The wavefunction  $\psi(\phi)$  takes the form of a Bloch function  $u(\phi)e^{iq\phi}$ , where  $u(\phi)$  is periodic with period  $2\pi$ . This approach appears particularly appropriate for the case  $E_c \gg E_J$  (that is,  $x \gg 1$ ) where the band structure approaches that of a free particle, with small energy gaps caused by the periodic Josephson potential. The "quasicharge"  $q$ , playing a role analogous to the crystal- or quasi-momentum in a solid, can then be accurately identified with the charge difference  $Q$ . Fig. 2.3 shows a sketch of the energy spectrum of the Josephson system, drawn both as a function of  $q$  and  $\phi$  for comparison, for  $x = 0.1$  and  $2.5$ . The qualitative behavior of the device is simple: the device can charge up, as a common capacitor, but it can only discharge by having electrons tunnel from one electrode to the other. While the charging-up process may be continuous, the discharge by tunneling is discrete, in units of  $2e$  for Cooper pairs. In this limit,  $E_J$  is the width of the gaps at  $q = \pm e$ , where the "kinetic energy"  $Q^2/2C = e^2/2C = E_c$ . In the opposite limit,  $x \ll 1$ , because of the negligible MQT between adjacent minima, the bands approach zero width, and low-lying ones are separated by the resonance frequency of a Josephson potential well,  $\hbar\omega_p = (8E_cE_J)^{1/2}$ .

### 2.3 The Effect of Dissipation

In their classic 1981 and 1983 papers, Caldeira and Leggett (CL) developed a successful method for incorporating the effect of dissipation in a macroscopic quantum mechanical Hamiltonian. [See Caldeira and Leggett 1981, 1983]. CL suggested modeling the environment as an infinite collection of harmonic oscillators. While the exact nature of the environment Hamiltonian term is usually unknown, this harmonic oscillator model is an extremely good representation of the system, as long as the extent to which any single

degree of freedom is perturbed is small.\* Building on concepts developed by Langer, Coleman, and Callan [Langer, 1967; Coleman, 1977; Callan and Coleman, 1977] CL use an "instanton" technique to calculate the effect of dissipation on the tunneling rate out of a metastable minimum, a calculation which can be easily applied to a Josephson device.

### 2.3.1 The harmonic oscillator Lagrangian

Throughout this section we refer to the "system" as the basic system of interest (i.e. the Josephson junction Hamiltonian  $H_0$ ), and to the "environment" as the collection of infinitely many degrees of freedom surrounding the system. Reverting to the "mechanics analog" notation introduced in Section 2.1, we write the basic system Lagrangian as

$$L_{sys} = \frac{P^2}{2M} - V(X) \quad (2.17)$$

Following CL, we write down the general Lagrangian for an infinite set of harmonic oscillators, modeling the environment

$$L_{osc} = \sum_j \left( \frac{1}{2} m_j \dot{x}_j^2 - \frac{1}{2} m_j \omega_j^2 x_j^2 \right) \quad (2.18)$$

where  $m_j$ ,  $x_j$ , and  $\omega_j$  are, respectively, the mass, position and resonance frequency of each oscillator. The effect of the environment on our system can then be modeled as an interaction term:

---

\* This does *not* imply that the treatment is restricted to low damping cases, since the collective effect of all degrees of freedom can be large.

$$L_{int} = \sum_j (F_j(X) x_j + \Phi(X)) \quad (2.19)$$

the critical assumption is, again, that each single degree of freedom is only weakly perturbed, so that the cross term can be taken to be linear in  $x_j$ . CL argue that the representation in (2.19) is valid without loss of generality. The function  $\Phi(X)$  is related to questions of frequency renormalization and, for many physical systems of interest is given by

$$\Phi(X) = - \sum_j \frac{F_j^2(X)}{2 m_j \omega_j^2} \quad (2.20)$$

This completes the statement of the Lagrangian. In order to examine the effect of dissipation on the dynamics of the Josephson system, further simplifications must be made. In the following section, (3.2.2) we cover the assumption of linear dissipation, often used to treat Josephson junctions in the semiclassical regime. We use it to briefly illustrate some consequences of damping on the phase tunneling rate and energy levels of the Josephson system.

### 2.3.2 The case of strictly linear dissipation

In the limit of "strictly linear dissipation," the cross-term in the system-environment interaction Lagrangian is linearly proportional to the position (or phase) variable  $X$ :

$$F_j = X c_j \quad (2.21)$$

Leggett [1984], shows that an arbitrary *linear* dissipation mechanism will satisfy (2.21). This includes thus not only strictly ohmic dissipation (having a simple resistor in parallel with the Josephson junction) but also any other linear admittance of arbitrary frequency dependence shunting the tunnel junction. The constants  $c_j$  are then related to the complex admittance of the system, as derived by Leggett [1984]. For the special case of ohmic dissipation, this relation is particularly simple: We define a spectral density for the harmonic oscillator bath as:

$$J(\omega) \equiv \frac{\pi}{2} \sum_j \frac{c_j}{m_j \omega_j} \delta(\omega - \omega_j) \quad (2.22)$$

Then,

$$J(\omega) = \eta \omega \quad (2.23)$$

where  $\eta$  is the simple friction coefficient for the system. In the case of Josephson junction shunted by a linear resistance  $R$ ,  $\eta/M$  corresponds to  $1/RC$ .

Once we assume (2.21), we can write down the complete Hamiltonian for the system and environment in a rather transparent way:

$$H = \frac{P^2}{2M} - V(X) + \sum_j \left[ \frac{1}{2} m_j \dot{x}_j^2 + \sum_j \frac{1}{2} m_j \omega_j^2 \left( x_j - \frac{c_j X}{m_j \omega_j^2} \right)^2 \right] \quad (2.24)$$

Equation (2.24) evokes a simple heuristic picture of a system of coupled harmonic oscillators, as sketched in Fig. 2.4.

The model of CL has had its greatest success in the calculation of the effect of dissipation on the tunneling rate out of a metastable well of the Josephson potential. CL

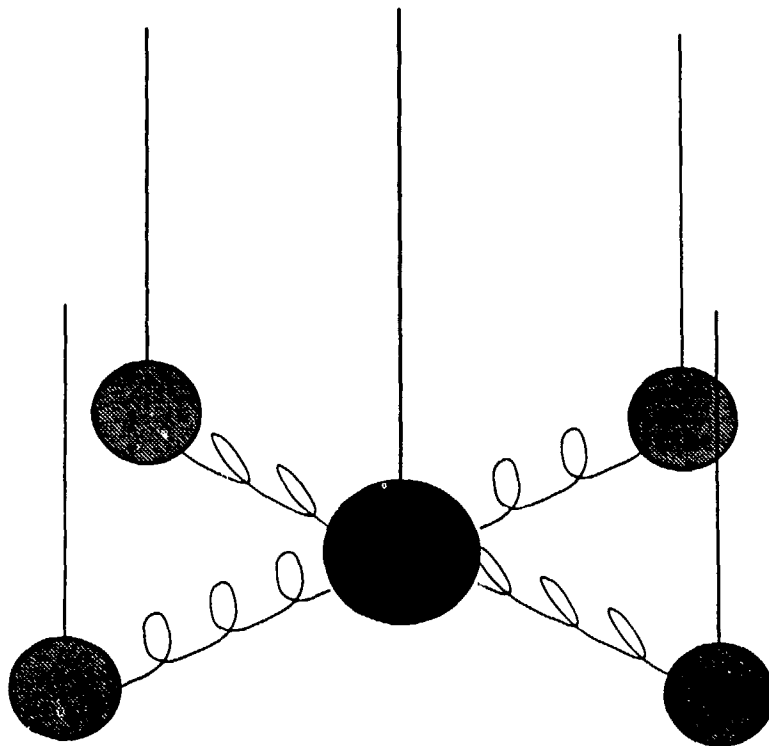


Fig. 2.4: Simple representation of the interaction between the Josephson system and the environment. The large pendulum is a representation of the Josephson tunneling interaction, the smaller pendula represent the oscillator bath.

[1981,1982] calculate the density matrix for the system, in the strictly linear dissipation limit. Since the only interest is in the motion of the coordinates of the system, and not of the environment, they can focus on the reduced density matrix, given by

$$K(X_i, X_f; T) = \int \prod_{\alpha} dx_{\alpha i} \sum_n \psi_n^*(X_i, \{x_{\alpha i}\}) \psi_n(X_f, \{x_{\alpha i}\}) \exp\left(-\frac{E_n}{k_B T}\right) \quad (2.25)$$

where the subscripts  $i$  and  $f$  denote the initial and final values, the product over  $\alpha$  accounts for the contribution of the infinite degrees of freedom of the environment, and the sum over  $n$  covers the states of the system. CL choose to examine the path integral representation of (2.25), which, after considerable simplification, integrating out the oscillator degrees of freedom, is expressed in the following form:

$$K(X_i, X_f; T) = K_o(T) \int_{X(0)=X_i}^{X(T)=X_f} D\{X(\tau)\} \exp\{-S_{eff}[X(\tau)] / \hbar\}$$

$$K_o(T) = \prod_{\alpha} \left[ \frac{1}{2} \cosh\left(\frac{\omega_{\alpha} \hbar \beta}{2}\right) \right] \quad (2.26)$$

where  $D\{X(\tau)\}$  denotes the integration over all possible paths from  $X_i$  to  $X_f$ \*, and  $\cosh$  denotes the hyperbolic cosecant. The "effective action"  $S_{eff}$  is given by

$$S_{eff}[X(\tau)] = \int_0^{\hbar\beta} \left[ \frac{1}{2} M \dot{X}^2 + V(X) \right] d\tau + \frac{1}{2} \int_{-\infty}^{\infty} d\tau \int_0^{\hbar\beta} [\alpha(\tau - \tau') [X(\tau) - X(\tau')] ]^2 d\tau \quad (2.27)$$

with

---

\* For a description of path integration, please see Feynman and Hibbs [1965, chapter 2].

$$\alpha(\tau - \tau') = \frac{1}{2\pi} \int_0^\infty J(\omega) \exp(-\omega|\tau - \tau'|) d\omega = \frac{n}{4\pi} \frac{1}{(\tau - \tau')^2} \quad (2.28)$$

where  $\beta = (k_B T)^{-1}$ , and the last approximate equality is only valid in the ohmic case.

These results can be applied to a variety of problems. The tunneling rate out of a metastable potential well is given by the imaginary part of the ground state energy, which is obtained from the density matrix  $K$  for  $X_i = X_f = 0$ . From this, one key general consequence of the model becomes apparent: Since the damping term [the rightmost term in (2.27)] is positive definite, the effect of damping is to increase the effective action and thus increase the exponent in the integral (2.26). While in the absence of the environment the density matrix need only be defined in  $X$  (or  $\phi$ ) space, when the collection of harmonic oscillators is included, the leading paths in the density matrix path integral are lengthened by a detour in the infinite dimensional space of the harmonic oscillators. *The final effect will always be to suppress the tunneling rate and lower the ground state energy of the system.*

The tunneling rate can be extracted from (2.26) in the semiclassical limit by using the method of steepest descents. The leading contributions to the integral (2.26) will then be from paths around the saddle point of the action  $S_{eff}$ . Callan and Coleman [1977] show that the ground state energy  $E_0$  can then be expressed in the form<sup>§</sup>

$$E_0 = \left( \frac{\hbar\omega_0}{2} - \hbar K e^{-\frac{B}{\hbar}} \right) (1 + O(\hbar)) \quad (2.29)$$

---

<sup>§</sup> The factor  $(1 + O(\hbar))$  implies that the expression is correct within additional dimensionless terms which contain a factor of  $\hbar$ , i.e., the expression is accurate in the semiclassical limit.



where the "bounce"  $B$  is equal to the action evaluated along the saddle-point path, and  $\omega_0$  is the classical resonance frequency of the well. The leading contribution to the bounce simply comes from the classical path in which the potential  $V(X)$  is turned upside down and the particle is allowed to accelerate down the energy well and "bounce" back to the starting point, as shown in Fig 2.5. While the term in the exponential  $B$  is due to the "shortest" path, the prefactor  $K$  is an indication of how many paths are contributing to the integral. The addition of damping thus appears to lower the ground state in the well. In general, the addition of damping to a stable or metastable system tends to squash the energy levels together, and push them towards the bottom of the well. A nice treatment of this is given by Esteve, Devoret, and Martinis [1986], who analyze the effect of an arbitrary linear damping mechanism on the energy levels of a Josephson device using simple second order perturbation theory on the damping Hamiltonian. As the tunneling rate increases, however, the problem becomes less semiclassical as more and more paths begin to contribute, and the approximation breaks down.

The tunneling rate  $\Gamma$  is given by

$$\Gamma = -2 \operatorname{Im} (E_0) / \hbar \quad (2.30)$$

If the potential  $V(X)$  is metastable, the above expression is not equal to zero. For the case of ohmic damping CL [1981,1982] estimate  $\Gamma$  to be equal to, at  $T = 0$

$$\Gamma = \frac{\omega_0}{2\pi} \sqrt{\nu} \chi \exp(-\nu s) \quad (2.31)$$

where  $\omega_0$  is the resonance frequency of the well,  $\nu$  is the barrier height normalized to  $\hbar\omega_0$ , and  $s$  is the bounce action normalized to  $\hbar\nu$ . In the case of weak damping,  $s$  and  $\chi$  are given by

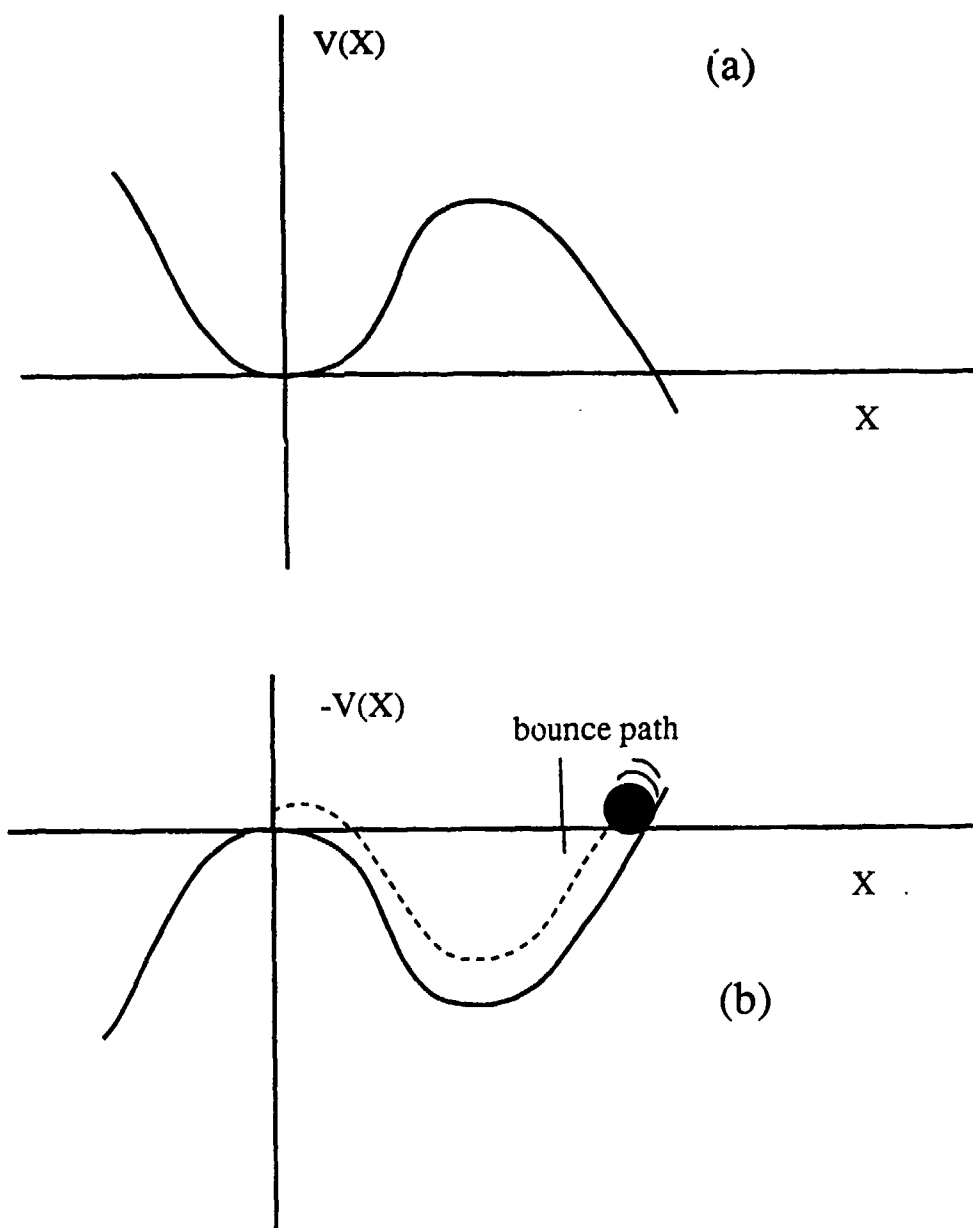


Figure 2.5: (a) A metastable potential. (b) Representation of classical "bounce" trajectory on upside-down potential

$$s = \frac{36}{5} \left[ 1 + \frac{45 \zeta(3)}{\pi^3} \alpha + O(\alpha^2) \right]$$

$$\chi = 12\sqrt{6} \pi [1 + c\alpha + \dots] \quad (2.32)$$

where  $\alpha = \eta/M\omega_b$ ,  $\omega_b$  being the resonance frequency of the inverted potential, and  $c \approx 2.8$ . These values are calculated for a cubic potential of the form  $V(X) = (1/2)\omega_b^2 X^2 - (1/3)\lambda X^3$ , but they apply with reasonable accuracy to the tilted cosinusoidal Josephson potential.

From (2.32) it is clear that the effect of damping becomes significant when the value of  $\alpha$  becomes of order one. If we express this in variables more common to Josephson junctions, we have (for zero current bias)

$$\alpha = \frac{1}{\pi\sqrt{2}} \frac{R_Q}{R} \sqrt{\frac{E_c}{E_J}} \quad (2.33)$$

where  $\omega_b = (8E_c E_J)^{1/2}/\hbar$ , and  $R_Q = h/4e^2$  is the quantum unit of resistance.

It is possible to extend the calculation and derive results as a function of temperature as has been done by several authors [see, for a review, H. Grabert, 1985, and P. Hänggi, 1986]. The tunneling rate increases with temperature. Qualitatively, in the low damping limit, the rate is essentially temperature independent below a crossover temperature  $T_{cross}$ , with

$$T_{cross} = \frac{\hbar\omega_b}{2\pi} (\sqrt{1 + \alpha^2} - \alpha) \quad (2.34)$$

More exactly, [see, for ex., Grabert, *et al.*, 1987] the normalized bounce action  $s$  becomes:

$$s = \frac{36}{5} \left[ 1 + \frac{45 \zeta(3)}{\pi^3} \alpha - \frac{5}{2\pi} \alpha \theta^2 - \frac{\pi}{12} \alpha \theta^4 + O(\alpha^2, \theta^6) \right] \quad (2.35)$$

where  $\theta = T/T_{cross}$ .

The major results of this section can be summarized as follows: CL developed a very nice way to include dissipation in a quantum mechanical Hamiltonian. The effect of dissipation is to *decrease* the quantum tunneling rate. CL estimated the tunneling rate in a semiclassical (low  $\hbar$ ) limit, and its decrease should be significant when the parameter  $\alpha$  (eq. 2.33) is of order 1. The crossover temperature from thermally activated to quantum behavior is given by (2.34) in the low damping limit.

While these results have been proven to be remarkably accurate in predicting the results of tunneling experiments, they break down when the energy level spacing is not much smaller than the barrier height. Therefore, while they present a qualitatively accurate and heuristically valuable method, the results in this section are expected to break down when  $E_C$  is of order  $E_J$ . In the latter case, if damping is sufficiently low, quantum fluctuations in  $\phi$  are expected to become comparable to the periodicity of the Josephson potential ( $2\pi$ ), as illustrated above in Section 2.2.1, and a full quantum treatment is needed.

### 2.3.3 Microscopic model of dissipation in a Josephson junction

In 1982, Ambegaokar, Eckern, and Schön, (AES), developed a microscopic model for dissipation in a Josephson tunnel junction. By using a functional integral approach, AES integrate out the quasiparticle degrees of freedom, responsible for the dissipation, and obtain the following form for the effective action  $S_{eff}$

$$S_{eff}[\phi(\tau)] = \int_0^{\hbar\beta} \left[ \frac{1}{2} M \dot{\phi}^2 + V(\phi) \right] d\tau + \frac{1}{2} \int_{-\infty}^{\infty} d\tau \int_0^{\hbar\beta} \alpha_{qp}(\tau - \tau') \left[ 1 - \cos\left(\frac{\phi(\tau) - \phi(\tau')}{2}\right) \right] \quad (2.36)$$

where we remind the reader that in our notation the "mechanics" variable  $X$  and the Josephson system variable  $\phi$  are interchangeable. The form in (2.36) thus reduces to the CL form in the limit of small  $\phi(t) - \phi(\tau)$ . The Fourier transform of the kernel  $\alpha_{qp}(\tau)$ ,  $\alpha_{qp}(\omega)$ , is proportional to the quasiparticle I-V response  $I_{qp}(V)$ , i.e. the I-V curve one would measure in a perfect superconductor - insulator - superconductor if the Josephson effect were destroyed. Specifically,  $I_{qp}(V) = -2e \alpha_{qp}(eV/\hbar)$ .  $\alpha_{qp}(\omega)$  has the following limiting forms, at  $T=0$  [Eckern, Schön and Ambegaokar, 1984]:

$$\alpha_{qp}(\omega) \approx \begin{cases} -\frac{3\pi}{32} \frac{\hbar}{2e^2 R_n} \frac{\hbar\omega^2}{\Delta}, & |\hbar\omega| < \Delta \\ -\frac{\hbar}{2e^2 R_n} |\omega|, & |\hbar\omega| > \Delta \end{cases} \quad (2.37)$$

with the voltage  $V$  corresponding to  $\hbar\omega/e$ . If only small frequencies and small variations of the phase/position variable are relevant to the problem, we can expand the trigonometric term in (2.36). The result is that the quasiparticle term in the effective action takes the same form of the kinetic energy term [see Eckern, Schön and Ambegaokar, 1984]. It is then possible to identify the effect of quasiparticles in this regime as simply adding mass (or capacitance) to the system. In capacitance units, we have:

$$\delta C = \frac{3\pi\hbar}{32\Delta R_n} \quad (2.38)$$

For parameters typical for our samples, having normal resistances in the kilohm region, this term is usually of order  $10^{-17}F$ , and is much smaller than the geometrical capacitance of the system, of order  $10^{-15}F$ .

The effective action quoted in (2.36) gives the problem an interesting twist in that it is periodic in the phase, but with period  $4\pi$ . The simple reason for this is that we have now allowed in the problem electrons (of charge  $e$ ) as well as Cooper pairs (of charge  $2e$ ). As a result, an acceptable basis for the Hamiltonian are  $4\pi$  periodic plane waves of the form  $\psi(\phi) \sim \exp(in\phi/2)$ , where  $n$  is an integer. These are now eigenstates of the charge operator  $Q=2ie \partial/\partial\phi$ , with eigenvalue  $ne$ , allowing for changes of charge in units of  $e$ . On the other hand,  $2\pi$  periodic wavefunctions would only allow changes in units of  $2e$ . Finally, for the case of ohmic dissipation, there is no phase periodicity in the effective action, given by (2.27), and nonperiodic wavefunctions are allowed. This is consistent with the statement that a classical resistive shunt can pass charge in a continuous fashion.

The ability of the system to change electrode charge in units of  $e$  has profound changes on the energy spectrum of the system, whose unit cell in charge space must now be of width  $e$ . This has been derived by various authors in the regime of large  $E_c/E_J$ <sup>†</sup>. Fig 2.6 shows a sketch after the calculation of Guinea and Schön (GS) [1986,1987]. The spectrum is similar in character to the one shown in Fig. 2.3. The horizontal variable,  $Q_x$ , which corresponds to  $q$  in Fig. 2.3, can again be interpreted as the total charge applied by some external means to the junction. As we apply more charge, the system charges up through the parabolic sections of the bands, and discharges by tunneling electrons across the junction. The main differences reflect the fact that the device can now discharge by tunneling in units of  $e$  as well as  $2e$ .

From (2.37), the dynamic resistance  $dV/dI$  approaches infinity as the voltage approaches zero, at  $T=0$ . This is not usually observed in real Josephson devices (including ours). This is usually blamed on imperfections in the junction barrier or to the existence of

---

<sup>†</sup> See, for example, Averin and Likharev [1986], Mullen, Ben-Jacob, and Schuss [1988], Guinea and Schön [1986,1987].

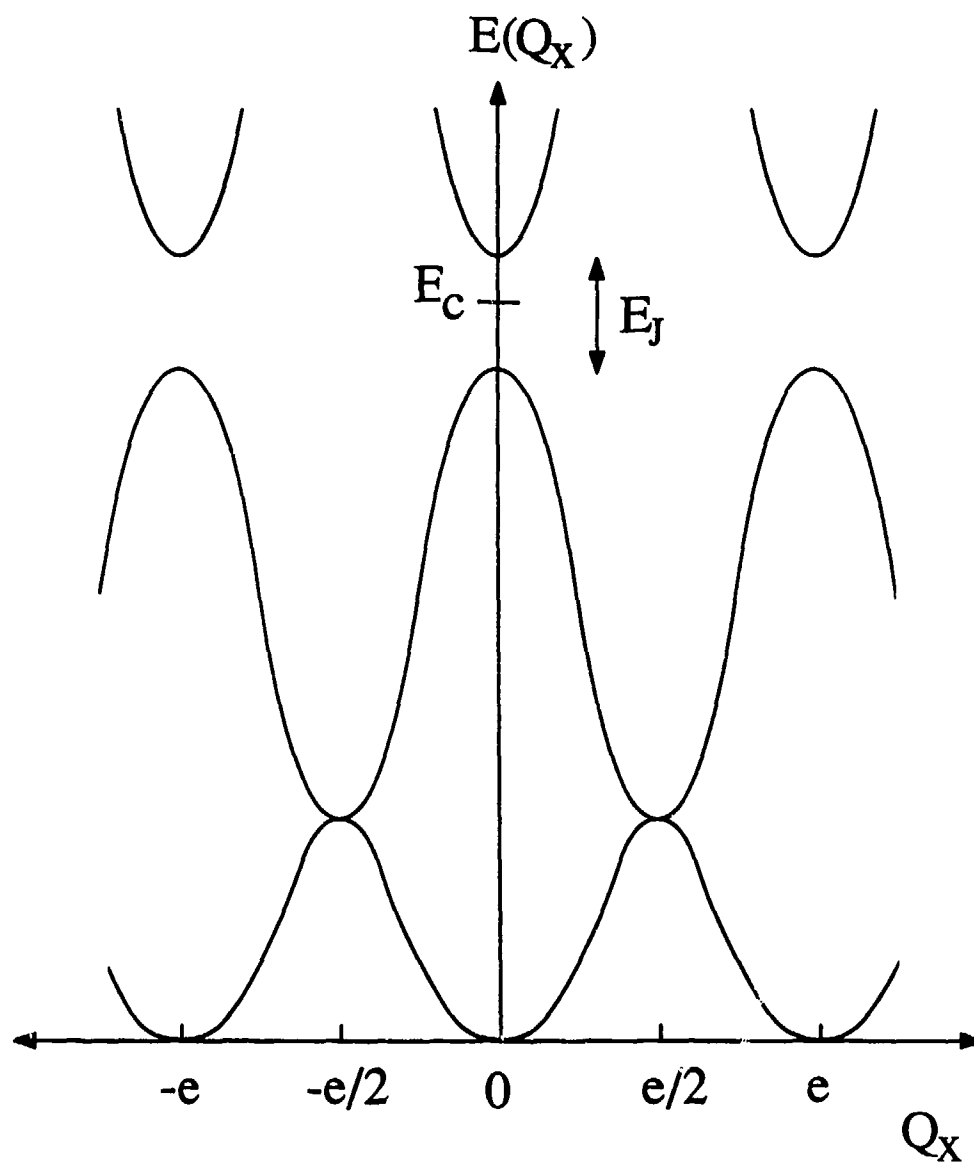


Fig. 2.6: Sketch of the energy spectrum as a function of applied charge derived for a Josephson junction in the large charging energy limit. [After Guinea and Schön, 1987.]

pair-breaking effects, not included in the approach of AES. Useful phenomenological approaches to include such complications are discussed below, in Section 2.5.1.\*

## 2.4 The Effect of the External Source

In order to measure the system properties, we must apply a current  $I$ . There has been a lot of speculation as to the best way to model a typical source of current, as to what its intrinsic impedance at the high frequencies of interest might be, and whether it should be treated classically or quantum mechanically. In this section, we assume when necessary that the system is indeed effectively current biased. In the discussion of our experimental work (see Chapter 6) this assumption is relaxed for the higher resistance samples.

### 2.4.1 $\phi$ -space approach

The energy  $E$  contributed by the external bias to the Josephson system is the integral of the power fed into the junction:

$$E = \int I(t) V(t) dt = \int I(t) \frac{\hbar}{2e} \frac{d\phi}{dt} dt \quad (2.38)$$

where we have used the Josephson relation  $V = (\hbar/2e) d\phi/dt$ . Integrating by parts, we have,

$$E = \frac{\hbar I}{2e} \phi - \int \frac{\hbar}{2e} \phi \frac{dI}{dt} dt \quad (2.39)$$

---

\* Guinea and Schön [1986; 1987] for example, use a phenomenological low voltage resistance  $R_{qp}$ .



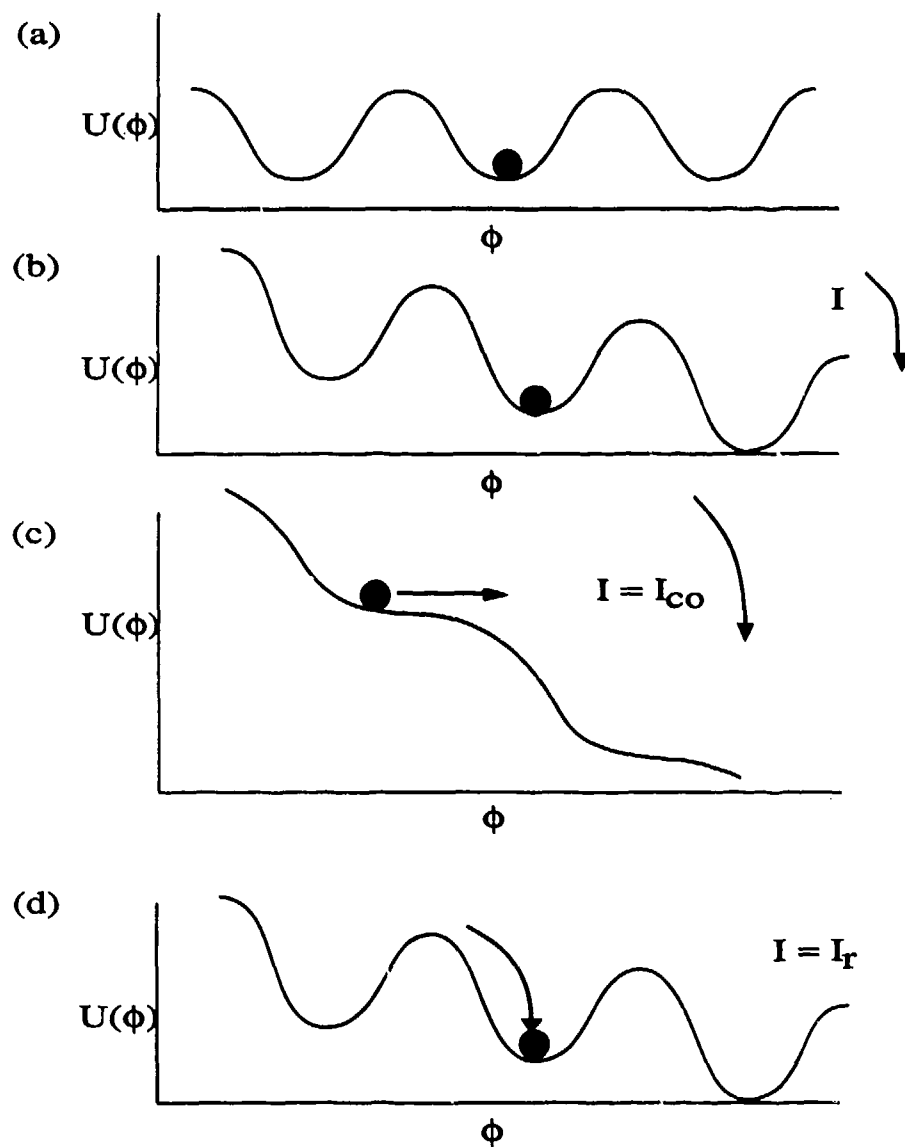


Fig. 2.7: The effect of current on the "washboard" potential. (a) no current is applied. (b)  $I$  is increased to a value less than the critical current. (c)  $I$  equals the critical current. (d)  $I$  is decreased until the particle is retrapped

If the current is constant, the second term in (2.39) is zero, and we can incorporate the effect of current bias by including a term equal to

$$H_s = (hI/2e) \phi \quad (2.40)$$

to the Josephson Hamiltonian. As a result, the effect of dc current bias, figuratively speaking, is to tilt the Josephson "washboard" potential, as shown in Fig. 2.7. The effect of a tilt is to lower the effective energy barrier between wells, and to decrease the resonance frequency of the individual well.

#### 2.4.2 $Q$ - space approach

The charge variable  $Q_x$  can be interpreted as charge applied to the junction by some external means. As a result we can make the following identification:

$$I = \frac{dQ_x}{dt} \quad (2.41)$$

Following Widom *et al.* [1982], Guinea and Schön [1986, 1987] do not use the approach outlined in 2.4.1 to include the bias into the Hamiltonian. Instead, they simply include  $Q_x$  in the charging part of the Hamiltonian,

$$H_o + H_s = \frac{(\hat{Q} + Q_x)^2}{2C} - E_J \cos(\phi) \quad (2.42)$$

The two charge variables can be interpreted in the following way:  $Q$  is an operator and is the fraction of total charge which does not commute with  $\phi$ ; it fluctuates due to tunneling through the junction barrier.  $Q_x$  is fixed by external constraints, which are assumed strong

enough to justify ignoring fluctuations in  $Q_x$ , and treating it as a classical variable. While  $Q_x$  can be varied continuously, the expectation value of  $Q$  can only change in discrete lumps of size  $e$ .

GS begin with the Hamiltonian description of (2.42), include damping, as discussed in Section 2.3.3, and arrive at the energy band spectrum shown in Fig. 2.6. In the presence of an imposed current  $I$  feeding charge onto the electrodes, the external charge variable  $Q_x$  advances at a rate  $dQ_x/dt = I$ . The instantaneous voltage is given by  $V = dE/dQ_x$ . While the energy spectrum may appear straightforward, the motion of the system along the energy band may be quite complex, even if we assume a perfect current source (an assumption which we later relax). If we begin at  $Q_x=0$ , the system can at first only charge up capacitively. Once  $Q_x$  is increased to a value greater than  $e/2$ , however, the system can follow the lower band or it can proceed upward, continuing to accumulate charge on one electrode, eventually relaxing to the lower band by having a single electron tunnel from one electrode to the other. Moreover, if the current is large enough, the system can Zener tunnel to the higher bands (which corresponds to charging up faster than electrons can tunnel to equalize the built up charge). Depending on the values of these various relaxation times, the size of the bandgaps, and the actual nature of the current source, one can obtain very different dynamics, corresponding to a large variety of possible I-V curves.

As the current  $I=dQ/dt$  increases, there is an increasing probability that the system will jump across the bandgap at  $E = E_c$  at the zone boundary ( $Q_x=e$ ), rather than continuing to cycle up and down in the lower bands. By simply transcribing the usual calculation of this Zener tunneling probability to the present context, we have previously shown [Iansiti *et al.*, 1987a] that the probability of a jump on each cycle is

$$P_{\text{Zener}} = \exp\left[-\frac{\pi^2 E_J^2}{8 E_c \left(\frac{\hbar I}{2e}\right)}\right] = \exp\left[-\frac{I_Z}{I}\right] \quad (2.43)$$

where we define the "Zener" current  $I_Z$  by

$$I_Z = \pi e E_J^2 / 8 \hbar E_c \quad (2.44)$$

It will be shown in Chapter 6 that these arguments will lead to an estimate for a reduced critical current, given by  $I_Z$ .

## 2.5 The Classical Limit

We have discussed the different terms which comprise the Hamiltonian of a Josephson junction. We have also discussed some of the quantum mechanical approaches which have been applied to the system. For conventional junctions (with  $E_J \gg E_c$ ), quantum fluctuations in  $\phi$  are very small, and the Hamiltonian can be treated classically. This section gives a basic treatment of Josephson junctions in the classical limit, which will be used extensively in the remainder of this report. We rewrite the complete Hamiltonian:

$$H = \frac{Q^2}{2C} + \frac{\hbar}{2e}(-I_{co} \cos \phi - I\phi) + H_e(\phi, \dot{\phi}, \{x\}) \quad (2.45)$$

where  $H_e$  represents is the environment term, which may be a function of both the phase and the environmental coordinates  $\{x\}$ . The "unfluctuated" critical current is  $I_{co} = (2e/\hbar) E_J$ . We can then obtain the classical Hamilton equations of motion, in the conjugate variables  $Q$  and  $\phi$ .

$$\dot{Q} = I - I_{co} \sin \phi + I_e(\phi, \dot{\phi}, \{x\}) \quad (2.46)$$

$$\dot{\phi} = \frac{2e}{\hbar} \frac{Q}{C} \quad (2.47)$$

Since the voltage  $V = Q/C$ , (2.47) is a statement of the ac Josephson effect. (2.46) can be interpreted as a current conservation equation; it provides the basis for the resistively and capacitively shunted junction (RCSJ) model [Stewart 1966, Mc Cumber, 1968].

### 2.5.1 The RCSJ model

The combination of the capacitive, Josephson, and resistive channels as parallel circuit elements is the essence of the RCSJ model. Equation (2.46) implies that the charge fed onto the junction electrodes by the source at a rate  $I$  can be carried off by either the Josephson or the quasiparticle "channels", or it can be stored on the capacitor  $C$ . This implies the simple picture of three parallel circuit elements shown in Fig. 2.8. The capacitor is the simplest part of the circuit, the only one that is intrinsically linear. The supercurrent-carrying Josephson channel is more complicated

$$I_s \equiv I_{co} \sin \phi = I_{co} \sin\left(\frac{2e}{\hbar} \int V dt\right) \quad (2.48)$$

where  $I_s$  is the supercurrent. (2.48) shows that the Josephson channel is inductive in nature. By differentiating (2.48) with respect to time, one can obtain the characteristic Josephson inductance,

$$L_J = \frac{\hbar}{2eI_{co} \cos \phi} \quad (2.49)$$

The last channel, the quasiparticle contribution, is the most difficult one to characterize. The effect of the quasiparticle environment may be divided into two parts.

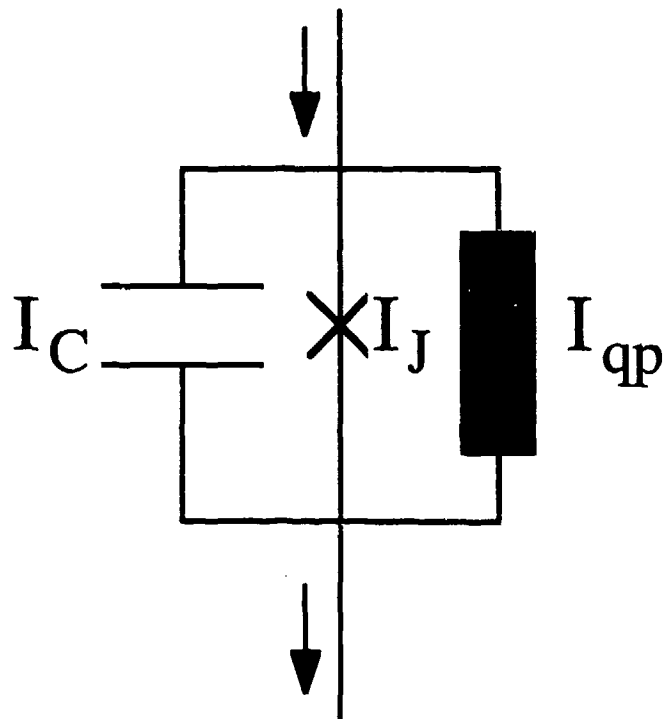


Fig. 2.8: Schematic of the equivalent junction circuit used in the RCSJ model. The Josephson, quasiparticle and capacitive contributions are viewed as three different channels

On one hand, there is the frequency dependent response to an excitation current or voltage. On the other hand, at finite voltages and temperatures, fluctuations in the dissipative quasiparticle "bath" have a significant thermal noise or shot noise contribution to the dynamics of the device.

The characteristic quasiparticle response was derived by Bardeen [1961] and Cohen, Falicov, and Phillips [1962]. In the latter's approach, the current through the quasiparticle channel is expressed as an integral over the product of densities of states on each side of the tunneling barrier. Their approach, originally developed for superconductor - insulator - normal metal (SIN) tunneling, can be applied to the SIS case, with

$$\begin{aligned}
 I_{qp} &= A \int_{-\infty}^{\infty} |T|^2 N_1(E) N_2(E + eV) [f(E) - f(E + eV)] dE \\
 &= \frac{1}{eR_n} \int_{-\infty}^{\infty} \frac{|E|}{\sqrt{E^2 - \Delta^2}} \frac{|E + eV|}{\sqrt{(E + eV)^2 - \Delta^2}} [f(E) - f(E + eV)] dE
 \end{aligned}
 \tag{2.50}$$

where  $A$  is a proportionality constant,  $|T|^2$  is the square of the tunneling matrix element (assumed energy independent)  $\Delta$  is the superconducting energy gap,  $V$  is the bias voltage, and  $f$  is the Fermi function. The simple interpretation of this result, known as the "semiconductor model" [see Tinkham, 1975] is that the quasiparticle current is proportional to the sum over all states of the product of the probability of having an excitation on one side of the barrier, times the probability of finding an empty "slot" on the other side. Few quasiparticles are available at low temperatures so that, for  $V < 2\Delta$ ,  $I_{qp}$  is very small, and the dynamic resistance is very high. This response is sketched in Fig 2.9. At  $T=0$ , the dynamic resistance  $dV/dI$  approaches infinity at low voltages. In a more complete treatment, as outlined briefly above in Section 2.3.3, the ideal low-voltage response is shown to be capacitive (also at  $T=0$ ), with a small characteristic capacitance given in (2.38).

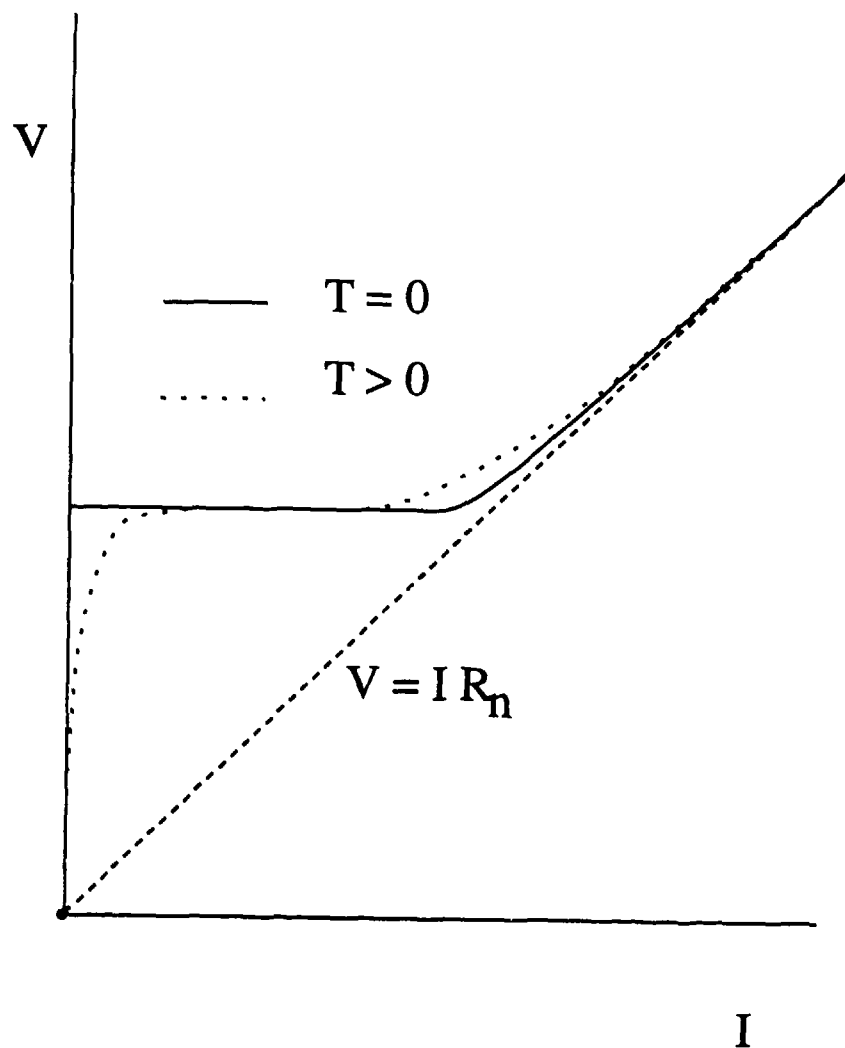


Fig. 2.9: Sketch of the quasiparticle I-V response.



The ideal situation outlined in the preceding paragraph is not usually encountered experimentally. In practice, junctions are imperfect, and some other mechanism is present which at low temperature gives a current larger than the ideal quasiparticle response, introducing additional dissipation. The nature of possible additional mechanisms is in some dispute, and may be different depending on the experimental situation: microshorts in the barrier, pair-breaking effects in the superconducting electrodes, and the effect of Andreev reflections have all been suggested. A good phenomenological approach, which has succeeded even in cases where high accuracy was needed [see, for example, Iansiti *et al.*, 1985], is to simply approximate the quasiparticle response by a piecewise linear resistor, so that

$$I_e = \frac{V}{R(V)} \quad (2.51)$$

with all of the environmental degrees of freedom absorbed in  $R(V)$ .  $R(V)$  is taken to be

$$R(V) = \begin{cases} R_n, & V > \frac{\Delta_1 + \Delta_2}{e} \\ R_L, & V \leq \frac{\Delta_1 + \Delta_2}{e} \end{cases} \quad (2.52)$$

where  $R_n$  is the normal resistance, and  $R_L$  is a phenomenological leakage resistance. The temperature dependence of the leakage term is found (at least for our samples)\* to be well approximated by the form

$$R_L^{-1}(T) \approx R_L^{-1}(0) + R_n^{-1} e^{-\Delta/kT} \quad (2.53)$$

---

\* See the experimental discussion in chapter 4.

where the second term's temperature dependence reflects intrinsic quasiparticle thermal excitation.

Finally, we must take into account the contribution of the noise fluctuations in the resistive channel. The autocorrelation function for a tunnel junction was derived by Dahm, *et al.* [1969] to be given by, at low frequencies  $\omega \ll eV/\hbar$ ,

$$\langle \hat{I}_N(t) \hat{I}_N(t + t') \rangle = e I_{qp}(V) \coth\left(\frac{eV}{2 k_B T}\right) \delta(t') \xrightarrow{V \rightarrow 0} \frac{2 k_B T}{R(V)} \delta(t') \quad (2.54)$$

where  $R(V)$  is defined here as  $V/I_{qp}(V)$ . Excellent agreement with experiment has been obtained by using the simplified expression for  $R(V)$  given above in (2.52) [Danchi, *et al.*, 1984; Iansiti, *et al.*, 1985]. As shown in (2.54), the autocorrelation function reduces to that of the Johnson noise formula at low voltages.

## 2.6 Junction Dynamics

We can now use the tools developed in the previous sections to discuss the most basic dynamics of a Josephson junction. We limit the present topics to relatively well known techniques, which have succeeded in modeling the behavior of conventional low resistance, high capacitance junctions. We will thus form a base for the discussion of our experimental results, given in Chapters 5 and 6, after the presentation of our observations in Chapter 4.

We begin our present discussion in the zero temperature classical limit in Section 2.6.1. In Sections 2.6.2 and 2.6.3 we discuss some simple consequences of significant (but still small) contribution of thermal and charging energies, respectively.

### 2.6.1 The classical regime

In this classical description, the system can be effectively visualized (see Fig. 2.10) as a particle lying at the bottom of a well of the "washboard" Josephson potential  $-E_J \cos \phi$  [Fig. 2.10 (a)]. The effect of the current bias is to tilt the potential, by adding a term  $-(\hbar/2e) I \phi$  [Fig. 2.10 (b)]. At low currents the particle is trapped in the well, and the average of the voltage  $V = (\hbar/2e) d\phi/dt$  is zero. At  $I = I_c$  [Fig. 2.10 (c)] the tilt is enough to allow the particle to escape. After having escaped, the particle will continue to run down the washboard, dissipating energy at a rate  $\langle V^2/R(V) \rangle$ . The average voltage in this regime (corresponding to the terminal velocity in our mechanics analog) is such that the loss in potential energy equals the loss due to dissipation (friction). If we now decrease the current, the particle will not immediately retrap in a Josephson well, since it has inertia. The retrapping current  $I_r$  is less than  $I_{co}$ , and is approximately (if the damping is low) given by the current at which the kinetic energy is equal to the energy barrier to be surmounted [Fig. 2.10(b)]. Stewart [1966] and Mc Cumber [1966] obtain:

$$I_r = \frac{4}{\pi} \frac{I_{co}}{\sqrt{\beta_c}}, \quad \beta_c = \frac{2e}{\hbar} I_{co} R^2 C \quad (2.55)$$

We believe it is reasonable to substitute  $R_L$  for  $R$  in  $\beta_c$  in this case. To justify this, it is necessary to further examine the physics behind this formula for  $I_r$ . In the presence of damping, the system loses energy at a rate  $dE/dt = -V^2/R$ .  $V = (\hbar/2e)d\phi/dt$ , and the total energy  $E$  stored in the capacitance, is  $1/2 CV^2$ . By combining these relations, one can write

$$\frac{dE}{d\phi} = -\frac{\hbar}{2eR} \sqrt{\frac{2(E + E_J \cos \phi)}{C}} \quad (2.56)$$

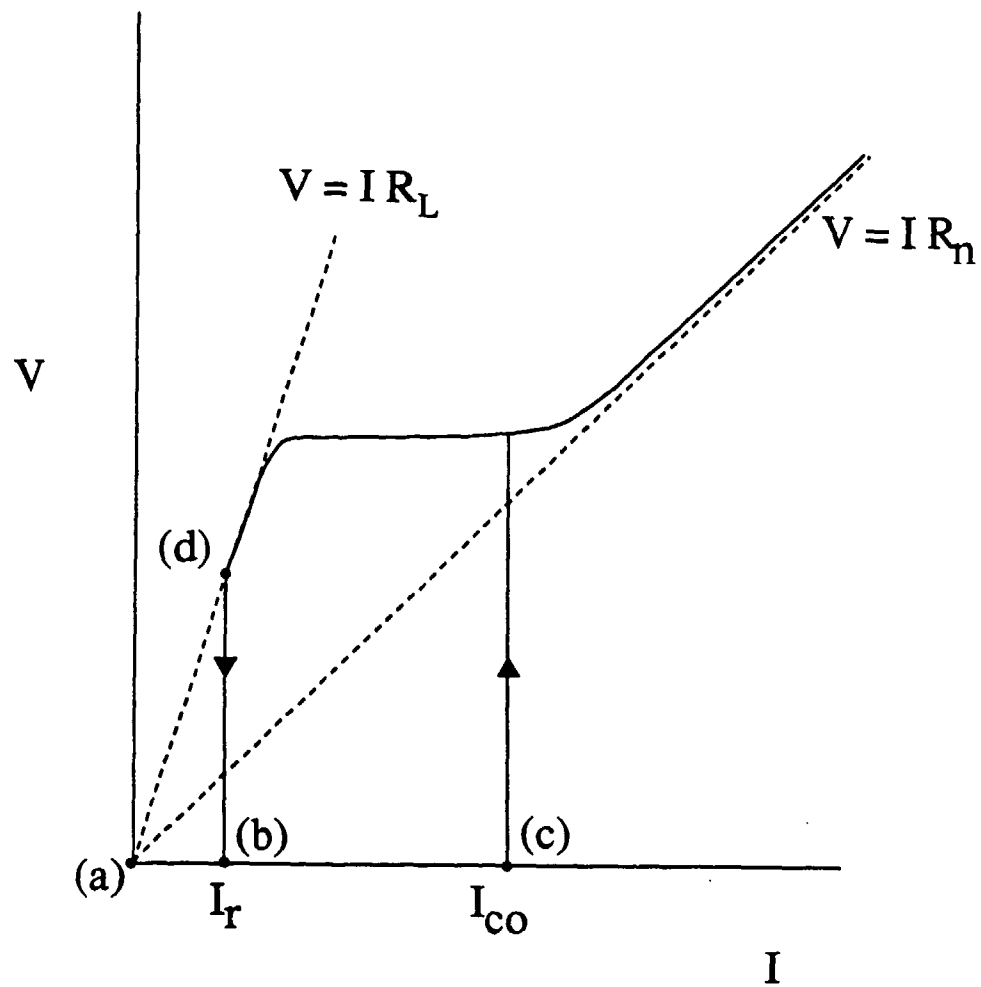


Fig. 2.10: Typical underdamped RCSJ I-V characteristic. The points labeled (a) through (d) correspond to the regimes sketched in Fig. 2.7 (a) through (d).

in which  $R$  is to be understood as being a function of the instantaneous voltage, which is determined by integrating this equation forward in  $\phi$ . The condition for  $I_r$  is that, if the particle starts at the top of one maximum of the tilted washboard, where it has zero velocity, it should just exactly reach the next maximum, again with zero velocity. If the tilt (i.e., current  $I$ ) is any greater, the representative point will run away at a rate limited by the damping; if it is any less, it will be trapped in the next minimum. For this critical trajectory, the voltage oscillates between zero (at the maxima) and a maximum value such that  $I/2 CV^2 \equiv 2E_J$ , corresponding essentially to the plasma frequency. The *average* voltage, as read off the I-V curve, is evidently less than  $2\Delta/e$ . Theoretically, one expects the quasiparticle conductance to be only weakly dependent on voltage for  $eV < 2\Delta$ . Accordingly, it is plausible that the *average*  $R$  determining  $I_r$  should be quite similar to the *measured*  $R_L$  at the *average* voltage.

### 2.6.2 Effect of small thermal fluctuations

The effect of thermal fluctuations on the dynamics of a Josephson device has received extensive experimental<sup>†</sup> and theoretical\* attention, in the regime of  $E_J \gg E_C$ ,  $k_B T$ . We limit our discussion to the underdamped case, relevant for our samples.

Since we are still in the classical regime, we will still use the particle-in-the-washboard analogy of Section 2.5. The basic idea is that now the particle can be thermally activated out of the Josephson potential well, at a current below  $I_{c0}$  [see Fig. 2.11 (a)]. The escape rate is usually given by an expression of the form

---

<sup>†</sup> See, for example, Fulton and Dunkelberger [1974], Naor, Tesche, and Ketchen [1982], Danchi *et al.* [1984], Silvestrini *et al.*, [1988], and Silvestrini, Liengme, and Gray [1988].

\* See Kramers [1940], Ambegaokar and Halperin [1969], P.A. Lee [1971], J. Kurkijärvi [1972], Büttiker, Harris and Landauer [1983], and Barone, Cristiano, and Silvestrini [1985].

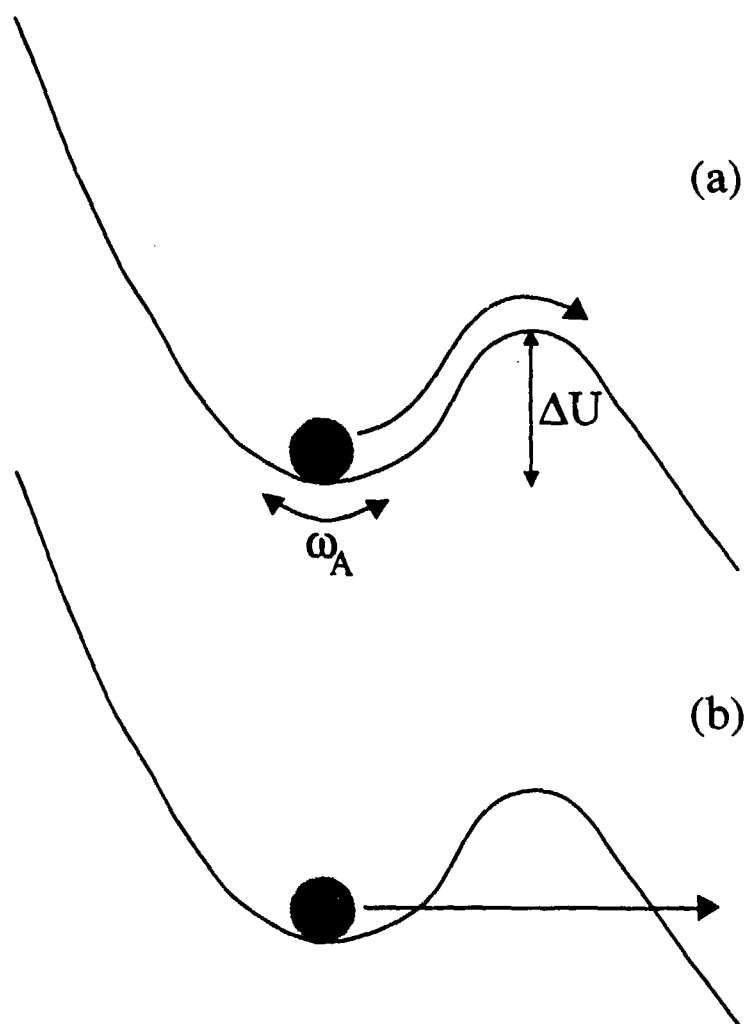


Fig. 2.11: Sketch of the two possible mechanism of escape from a well of the Josephson potential: (a) thermal activation. (b) quantum tunneling

$$\tau^{-1} = \frac{\omega_A}{2\pi} F(E_J, R, C, T) e^{-\frac{\Delta U}{k_B T}} \quad (2.57)$$

where  $\omega_A$  is the resonant frequency of the well,  $\Delta U$  is the barrier height, and  $F$  accounts for the effect of damping. For  $I < I_{co}$ ,  $\Delta U = 2E_J$ , and  $\omega_A = \omega_p = (1/\hbar)(8E_J E_c)^{1/2}$ . After the particle is activated out of the potential well, it will keep running downhill, since the system is underdamped, and the voltage will approach the energy gap value. The measured critical current  $I_c$  will thus be less than  $I_{co}$ , and will have a probabilistic distribution of values, dependent on the sweep rate. If we assume that  $F$  will have a value of order unity, one expects switching to occur when [Iansiti, *et al.*, 1988b]

$$I_c = I_{co} \left[ 1 - \frac{k_B T}{2E_J} \ln \left( \frac{\omega_p \delta I_c}{dI/dt} \right) \right]^{2/3} \quad (2.58)$$

where  $\delta I_c / (dI/dt)$  is the time spent sweeping through the switching distribution. A more careful analysis by Danchi [1984] gives the same result, apart from small numerical refinements. Thus  $I_c$  depends logarithmically on the current sweep rate.

Because this escape is a probabilistic event, the  $I_c$  measured in an actual experiment is different on each current sweep. The distribution of measured  $I_c$  values has a characteristic width  $\delta I_c$ , mentioned above, which is proportional to the extent of the depression of  $I_c$ . For the dependences cited above, one finds

$$\delta I_c = \frac{\frac{2}{3}(I_{co} - I_c)}{\ln \left( \frac{\omega_p \delta I_c}{dI/dt} \right)} \quad (2.59)$$

### 2.6.3 Effect of small quantum fluctuations

As discussed in Section 2.1, if the charging energy becomes significant, we expect to see quantum fluctuations in  $\phi$ . The first clear manifestation of this was the measurement<sup>#</sup> of the macroscopic quantum tunneling (MQT) of the phase through the potential barrier of the tilted washboard potential, shown schematically in Fig. 2.11 (b). This has been studied theoretically by various authors,<sup>†</sup> and we have already discussed the tunneling calculation in Section 2.3.2. A formula for the tunneling rate is given by (2.31). The effect of tunneling on the I-V response of the junction is similar to the effect of thermal activation:  $I_c$  acquires a distribution of values and is less than  $I_{c0}$ .

## 2.7 Summary

In this chapter we have discussed some powerful theoretical concepts which form the basis for a description of the Josephson junction. We have developed a model Hamiltonian for the system, and analyzed its implications in a few well-known situations. We have thus developed a theoretical basis for the analysis of our observations. After presenting our experimental techniques and results, we will resume the theoretical discussion in Chapters 5 and 6. This current chapter will then serve as a springboard for the discussion of the experimentally relevant parameter regime, in which the charging energy is comparable to or greater than the Josephson energy.

---

<sup>#</sup> See den Boer and de Bruyn Ouboter [1980], Prance *et al.* [1981], Voss and Webb [1981], Jackel *et al.* [1981], Washburn *et al.* [1985], Schwartz *et al.* [1985], Martinis, Devoret, and Clarke [1985], Devoret, Martinis, and Clarke [1985].

<sup>†</sup> See, for example, Caldeira and Leggett [1981; 1983], Chang and Chakravarty [1984], Grabert [1985], and Hänggi [1986], and references therein.



### CHAPTER 3

#### EXPERIMENTAL TECHNIQUES

This chapter describes the most important experimental techniques used in the fabrication and measurement of the properties of the samples. It is divided into two sections. We begin in Section 3.1, by describing the lithography and deposition methods involved in the fabrication of the junctions. We continue in Section 3.2 with a description of the measurement electronics, and a brief account of the low temperature techniques used in the measurements.

#### 3.1 Fabrication Techniques

The aim of the work reported here was the study of devices whose ratio of charging to Josephson energy is of order one. This goal created challenging requirements for the patterning techniques used in the fabrication of the junctions. The Josephson energy  $E_J$  is given at low temperatures in an ideal junction by the expression  $E_J = (h/8e^2)(\Delta/R_n)$ . The charging energy  $E_C$  is given by  $e^2/2C$ . We assume that

$$C = \epsilon_o \epsilon_r \frac{A}{d} \quad \text{and} \quad R_n = (\text{const}) \frac{e^{\frac{d}{d_o}}}{A} \quad (3.1)$$

where  $A$  is the area of the device,  $d$  is the insulating barrier thickness, and  $d_o$  is a constant of order  $1\text{\AA}$ . We can then express the charging energy as a function of the junction area and thickness. Assuming a relative dielectric constant  $\epsilon_r \approx 6$ ,\* we reach the following estimate:

---

\* See Wang and Gailey [1978], and Danchi [1983]

$$\frac{E_c}{k_B} = \frac{e^2}{2 k_B \epsilon_o \epsilon_r} \frac{d}{A} \approx \frac{0.035 K}{A [(\mu m)^2]} \quad (3.2)$$

where we have assumed a reasonable barrier thickness  $d \approx 20 \text{ \AA}$ . In order to be able to measure charging energy effects, we need  $E_c/k_B$  at least of order the accessible temperatures. In order to obtain  $E_c/k_B > 1K$  we need  $A < 0.04 (\mu m)^2$ . To obtain a junction of such small area, the fabrication of electrodes of width less than one micron is necessary. Since  $E_J \propto 1/R_n$  depends exponentially on the barrier thickness  $d$ , where  $E_c$  depends only linearly, we can obtain  $E_c \sim E_J$  by adjusting the barrier oxidation time.

This is the first thesis written in this research group which reports studies of thin film devices of submicron dimensions. The fabrication of submicron size junctions required the adaptation of a new set of patterning techniques. These were mainly based on electron-beam lithography, which allows the exposure of very fine lines in organic polymer resists without incurring the minimum size limitations of photolithography, set by the wavelength of light.

The first step in the sample fabrication is the patterning and evaporation of pads, to connect the fine junction features with the large scale leads necessary for the measurements. Next, the junction fabrication method is similar to the "overlap" junction methods developed at Bell laboratories<sup>§</sup>. The method begins with the preparation of a submicron suspended bridge of resist material. The first junction electrode of Sn is then evaporated at an oblique angle. After the first electrode is oxidized, the second electrode is evaporated at a different angle, completing the junction under the bridge of resist. An outline of the fabrication process is sketched in Fig. 3.1. The details of the fabrication are given below, in Sections 3.1.1, 3.1.2, 3.1.3, and 3.1.4.

---

<sup>§</sup> See, for example, Dolan [1977], Dolan *et al.* [1981], Hu, Jackel, and Howard [1981].

resist bridge

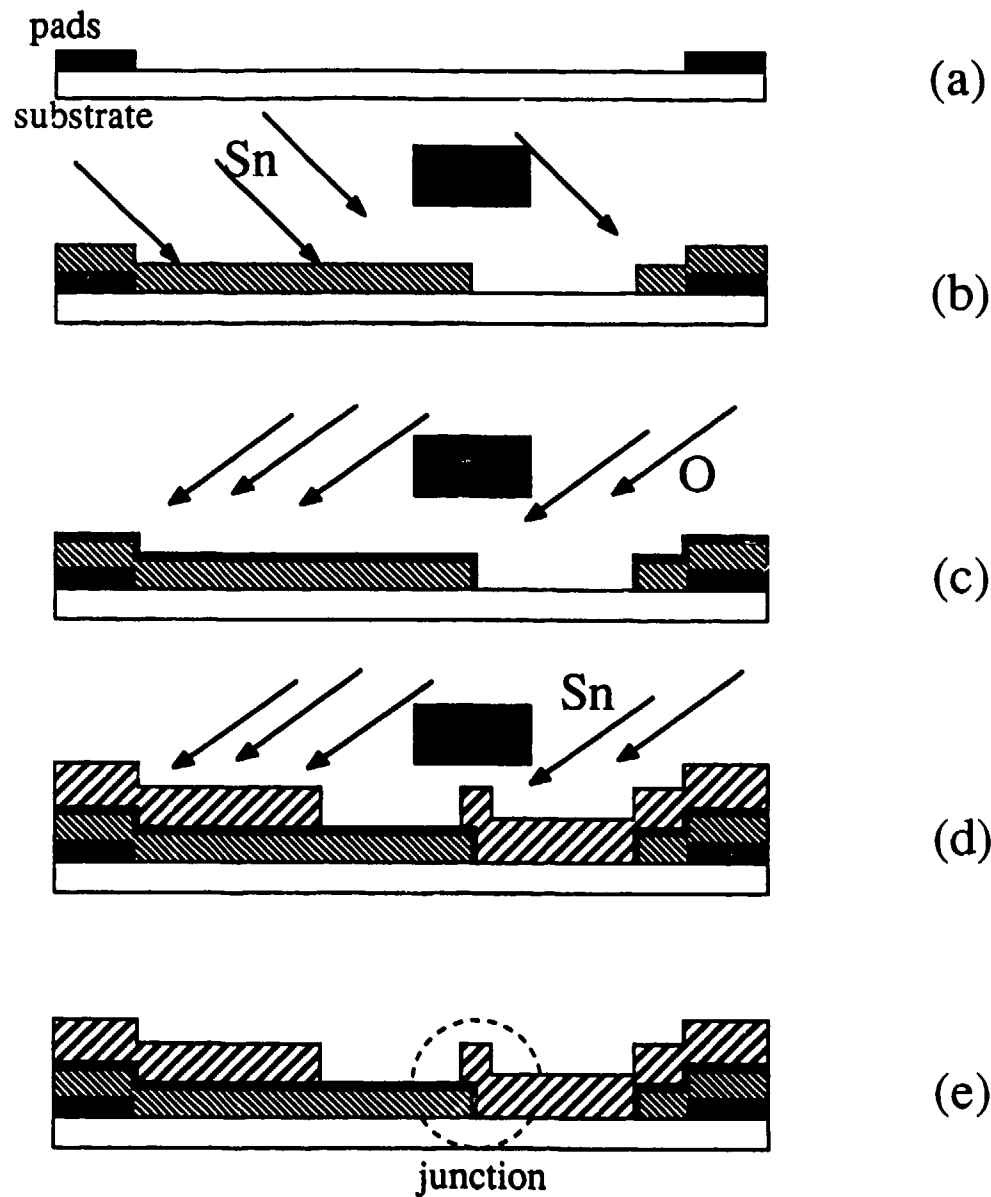


Fig. 3.1: Outline of the fabrication process. (a) After having evaporated contact pads, a suspended bridge of resist is patterned. (b) The bottom electrode of tin is evaporated at a 45° angle. (c) The oxide barrier is grown by a dc glow discharge. (d) The tin counter-electrode is evaporated. (e) The completed sample is shown.

### 3.1.1 Fabrication of contact pads

The small features necessary for the construction of submicron junctions are patterned with electron beam lithography, which has a characteristically small field of view ( $< 100 \mu\text{m} \times 100 \mu\text{m}$ ). Therefore, larger contact pads are necessary to connect the junction area to the leads on the dilution refrigerator sample loading slug. The contact pads were patterned by conventional optical lithography, using a liftoff technique. The essence of the liftoff technique is sketched in Fig. 3.2. The substrate is first coated with a photosensitive material known as photoresist (PR) and exposed through a mask made of chrome evaporated on glass. The photoresist is then developed (the exposed PR is dissolved). Finally metal is evaporated and the remaining photoresist is removed, defining the desired pattern.

Since the yield of the whole fabrication process is usually low, the best approach is the parallel patterning and deposition of as many sets of contact pads as possible, to make sure that a working sample is obtained by the end. After having decided that a two inch wafer size was convenient given the constraints of the available equipment, we designed a mask that would fit sixteen sets of pads in a 1" x 1" square in the center of the wafer. Each set of pads was 1/4" x 1/4", to conveniently fit on the sample loading slug of the dilution refrigerator. A sketch of the pad pattern is shown in Fig. 3.3. The mask was made by Advance Reproductions, Inc., located in Willows Industrial Park, 100 Flagship Drive, North Andover, MA 01845.

Because the minimum linewidth on the pad mask was as large as  $20 \mu\text{m}$ , this part of the process is not particularly difficult. Two specific techniques have been used with success: a fast but sometimes unreliable one-layer technique involving a chlorobenzene soak, and the more time consuming but reliable three layer photoresist - aluminum - photoresist (PR-Al-PR) technique. Since the latter is described in detail in Danchi's thesis [Danchi, 1983], we will not dwell on it here. For the chlorobenzene technique, oxidized Si

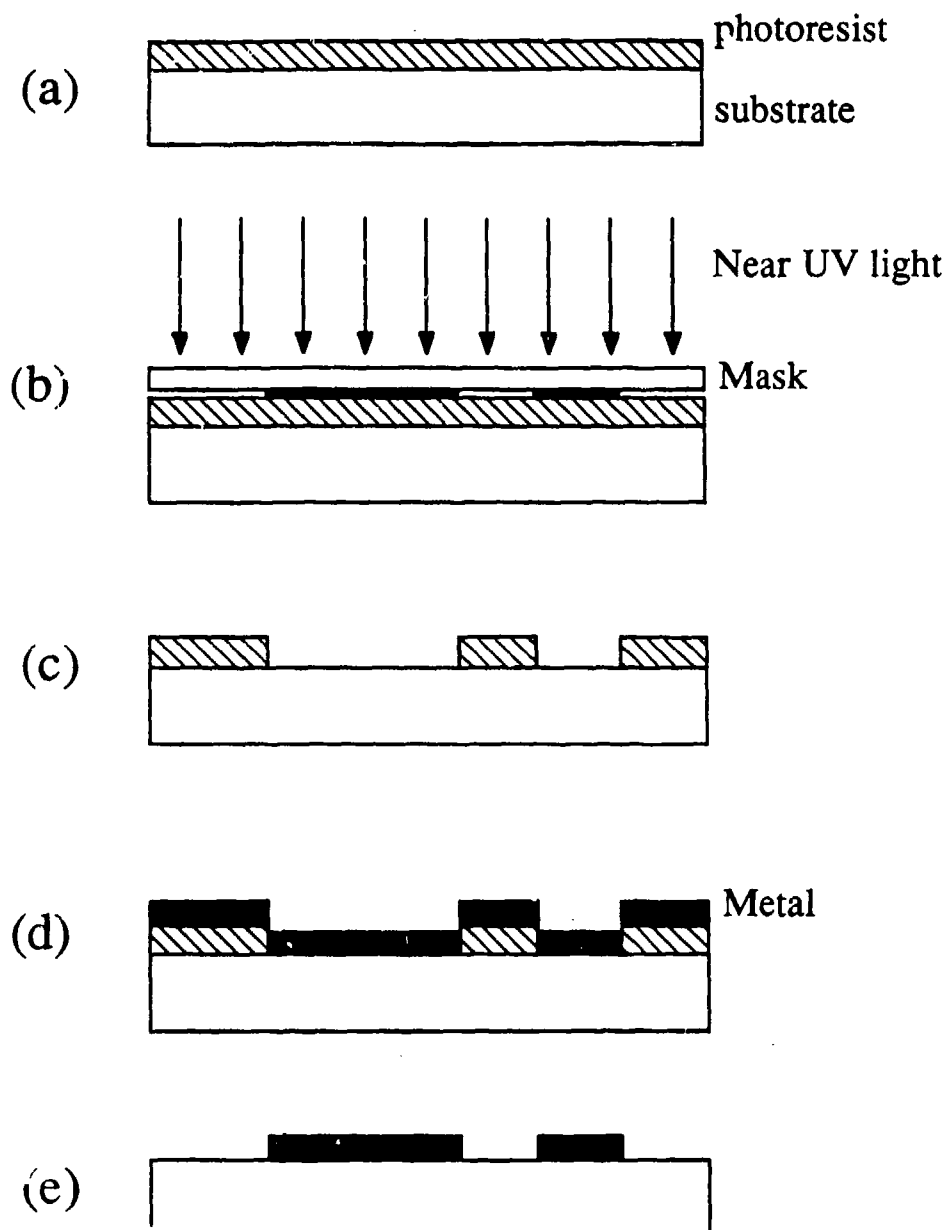


Fig. 3.2: Outline of the liftoff process. (a) The photoresist is spun on the substrate. (b) The coated substrate is exposed with near UV light through a chrome-on-glass mask. (c) The photoresist is developed. (d) Metal is evaporated. (e) The photoresist is dissolved

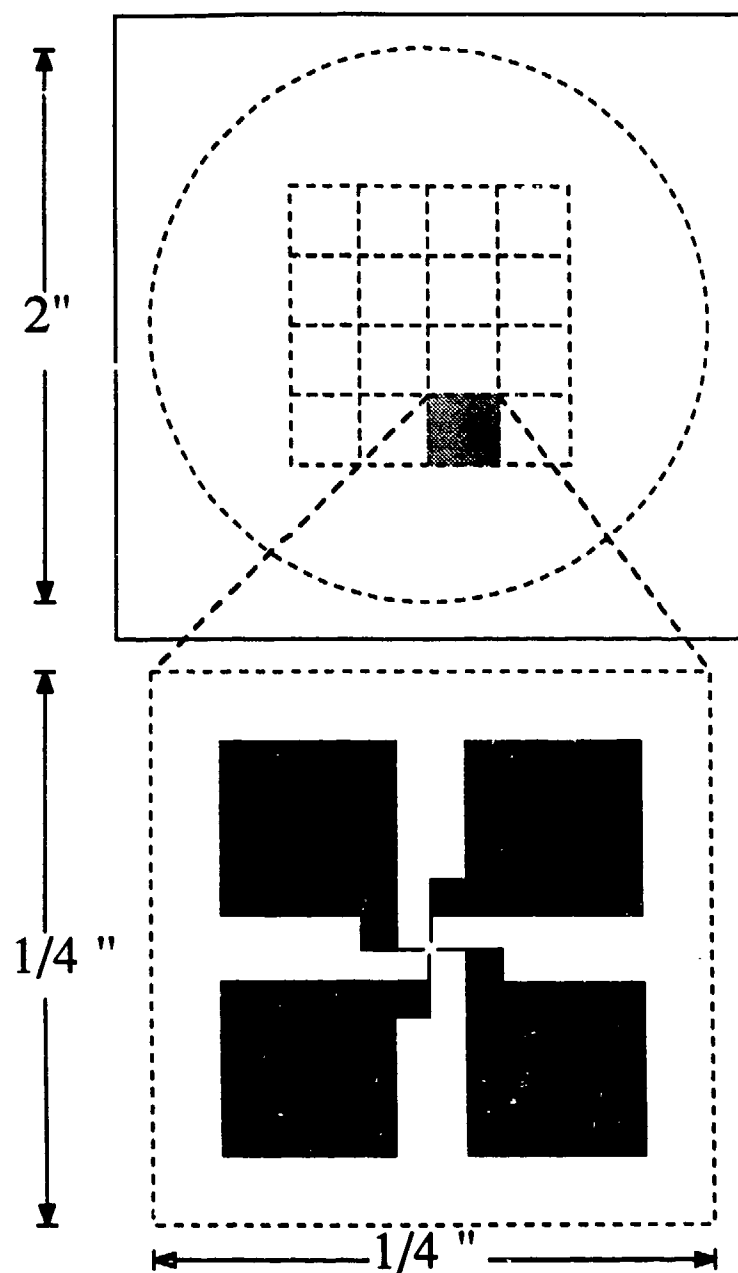


Fig. 3.3: Sketch of the mask used in the fabrication of the contact pads. The blowup shows a single set of pads.

wafers are first cleaned\* and coated with about 1  $\mu\text{m}$  of Shipley photoresist (AZ 1400-27, spun at  $\sim 4000$  rpm), and baked at  $70^\circ$  for 20 minutes. After cooling off for at least ten minutes, the wafers are exposed with the Karl Suss mask aligner in the soft contact mode. Next, the wafers are soaked in new chlorobenzene for 10 minutes. The wafers are then developed in a 1:5 solution of AZ 351 developer and water, for 5 to 10 minutes. The wafers are mounted in an evaporator, and coated with 50  $\text{\AA}$  of Cr followed by 400  $\text{\AA}$  of Au.<sup>†</sup> Finally, the liftoff is completed by soaking the samples in acetone. The pads are now ready to be cleaned and coated with the resist for the next step of the fabrication process.

### 3.1.2 Electron-beam lithography: general concepts

Electron-beam lithography is the exposure of patterns in an organic resist material by means of a narrowly focused beam of electrons. By using different accelerating voltages, resist materials and substrates, different characteristic linewidths and resist profiles are achievable.<sup>‡</sup>

Polymethylmethacrylate (PMMA) is the most commonly used resist in electron-beam lithography. PMMA, like most radiation-sensitive resists, is a polymer consisting of a long linear chain, the "backbone", attached to a number of sidegroups. PMMA is dissolved in a suitable solvent (such as chlorobenzene,) spun on the substrate, and baked. The solvent evaporates, and the PMMA goes from being a solution of neatly separated

---

\* The cleaning process was as follows: Heat for 5 minutes on hot plate in a 1:2 solution of photoresist stripper and water. Transfer mixture to ultrasonic cleaner for 10 minutes. Rinse in running 18 M $\Omega$  water for 15 minutes. Immerse for 10 minutes, respectively, in trichloroethylene, acetone, and methanol, and agitate with the ultrasonic cleaner.

† It is essential to fill the liquid nitrogen cold trap of a diffusion-pumped evaporator, even for this simple process, to avoid contaminating the wafers with pump oil.

‡ For a complete reference, please see Wittels [1980.]

molecules, to a tangled web of polymers forming a mat which uniformly covers the substrate. The resist is then exposed with an electron-beam, which attacks the sidegroups, and severs them from the backbone.\* These sidegroups are easily removed, leaving behind a highly porous mass which the developer can infiltrate to dissolve the main body of the resist. The unexposed PMMA lacks the porosity, and the action of the developer is much slower. Developers usually consist of two ingredients. The first is the solvent, and the faster it can infiltrate the PMMA mass, the faster it will dissolve it; as a good rule of thumb, the higher the molecular weight of the solvent, the slower the diffusion, and the longer the development process. The second ingredient is a nonsolvent which affects the rate at which the PMMA goes from a gel to a liquid, by adjusting the enthalpy of the solution.

The interaction of these various processes gives rise to a value of "critical dose"  $D_c$ . If the dose received by the resist is greater than  $D_c$ , the resist will be dissolved by the developer. In electron-beam lithography, dosage is usually given in units of charge/area; in our system, a typical dose (with a 10kV electron-beam) is in the neighborhood of 10 pC/( $\mu\text{m}$ )<sup>2</sup>. It is possible to increase the sensitivity (or decrease  $D_c$ ) of PMMA, by changing its molecular weight and by copolymerization with methacrylic acid [Wittels, 1980]

A sketch of the exposure process is shown in Fig. 3.4. The ultimate resolution of PMMA is the size of the basic molecule, being of order a 50 Å (depending on the molecular weight.) Apart from the size of the resist molecule (very small by our standards) other factors can strongly influence the width of the exposed pattern: the width of the focused beam of electrons, and the forward and back scattering of electrons. As the electrons travel through the resist, they scatter against the resist molecules, broadening the size of the beam. Moreover, once the electrons reach the substrate, they scatter back into the resist, interacting with the resist molecules, and broadening the exposed area. These two phenomena are

---

\* If the PMMA is overexposed, on the other hand, the polymer units crosslink in an essentially insoluble mat.



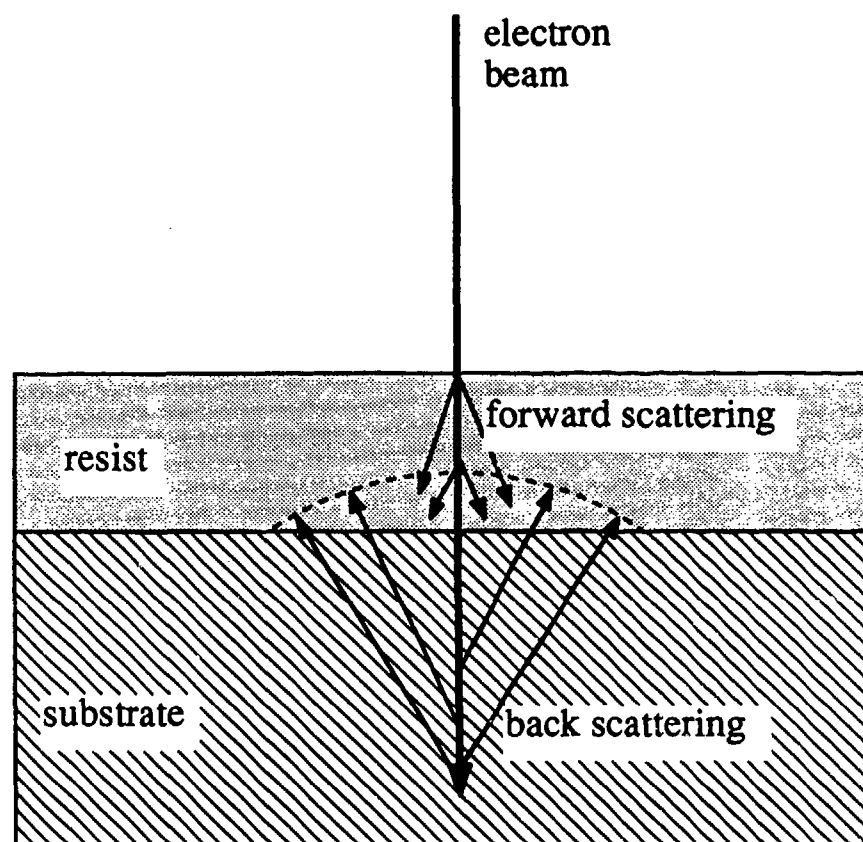


Fig 3.4: Sketch of the electron beam exposure process, including forward and backscattering effects. A realistic simulation of the phenomenon is shown in Wittels [Fig. 1.15,1980].

known as "forward scattering" and "backscattering", respectively. The two broadening processes are sometimes modeled as giving rise to two concentric Gaussian distributions of beam current intensity [Wittels, 1980]

$$J(r) = \frac{I}{\pi} (\alpha^2 e^{-\alpha^2 r^2} + b\beta^2 e^{-\beta^2 r^2}) \quad (3.3)$$

where  $1/\alpha$  and  $1/\beta$  are the characteristic widths of the forward and back scattered electron beam components. The dose at any point is then given by multiplying (3.3) by the exposure time. The upshot is that the dose received by the resist molecules will vary with depth and with the voltage of the electron-beam: If the voltage is high, there will be less forward scattering, and the electrons will penetrate further into the substrate before backscattering. Therefore, the backscattered electrons will be spread out over a wide area, and might not contribute much to the dosage received by the resist molecules. A high beam voltage will tend to minimize the exposed width, and give rise to a relatively vertical resist profile. If the voltage is low, on the other hand, forward scattering will broaden out the beam, and backscattered electrons will be restricted to a smaller radius, and thus effectively contribute to the dose received by the resist. Therefore the linewidth will broaden, but the resist profile will have a much more pronounced "undercut", i.e. the exposed line will be broader at the bottom than at the top.

### 3.1.3 Electron-beam lithography: junction patterning procedures

The fabrication of an overlap junction requires the patterning of an overhanging bridge of resist (as shown above in Fig 3.1.): A line is exposed in the resist, leaving a small gap in the middle. If the undercut is large enough, and the gap small enough, the resist will be exposed through the gap region in the lower resist layers, but not in the top layers. This will leave a bridge of resist after development (see Fig 3.5). The successful fabrication of

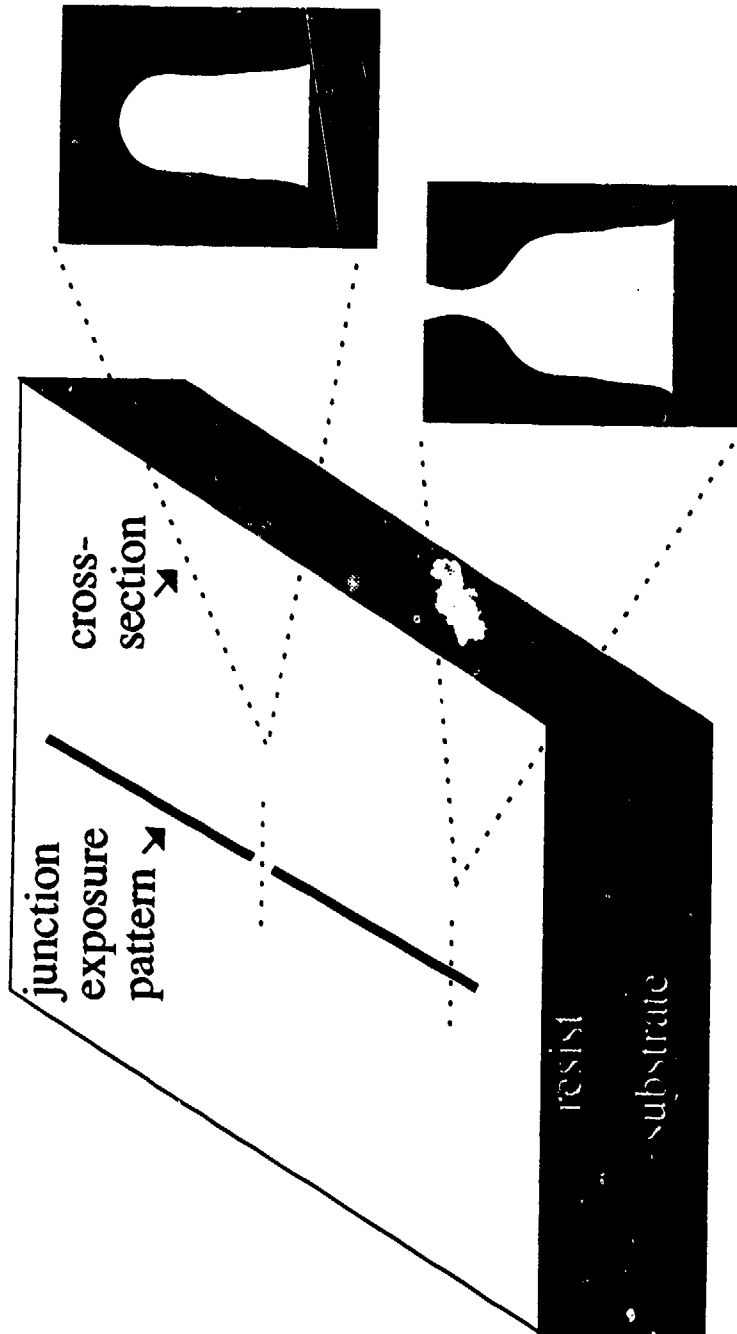


Fig. 3.5: Sketch of pattern exposed to produce the resist bridge necessary for the fabrication of an overlap junction. Also shown are crosssections of the developed resist.

submicron overlap junctions thus requires the capability to pattern lines of submicron width while at the same time obtaining the large undercut necessary for the resist bridge. We chose to solve this problem by using a low beam voltage (10 kV) to maximize the effect of backscattering to create an undercut. We also used a two layer resist scheme, with a thin layer of PMMA on top and a thick bottom layer of the more sensitive PMMA/MAA (polymethylmethacrylate/methacrylic acid), to further enhance the undercut profile. The idea is that a gaussian beam of electrons will expose a narrower hole in the less sensitive top layer than in the more sensitive bottom layer, creating the desired strongly undercut profile. Furthermore, we used very low exposure currents, to minimize the number of resist molecules at the top of the resist structure to receive the critical dose, and to lengthen the development time. The long development time, (~ 10 minutes,) allowed the close monitoring of the sample under an optical microscope; the development was stopped as soon as the sample appeared completely developed, and before the exposed lines could be broadened by overdevelopment.

The process begins by cleaning the newly prepared contact pads (patterned in a 16 x 16 array on a 2" wafer) by immersing them 10 minutes each in TCE, acetone, and methanol, in the ultrasonic cleaner. Next, the bottom resist layer is spun. This layer is chosen to enhance the undercut, and ease the liftoff process. Therefore, it must be composed of a very sensitive resist, and it must be thick enough, for the deposited metal to lift off without tearing at the edges<sup>†</sup>. The bottom layer is thus composed of PMMA/MAA, (available in beads from Esschem, dissolved 0.12 g/ml in glacial acetic acid) and is spun at a very slow speed, 2000 or 3000 rpm, giving rise to a resist thickness of about 0.4 - 0.6  $\mu\text{m}$ . The wafers are then baked at 180° C for one hour. After letting the wafers cool for at least ten minutes, the second resist layer is spun.

---

<sup>†</sup> As a rule of thumb, to avoid tearing, the resist thickness should be at least three times the thickness of the film.

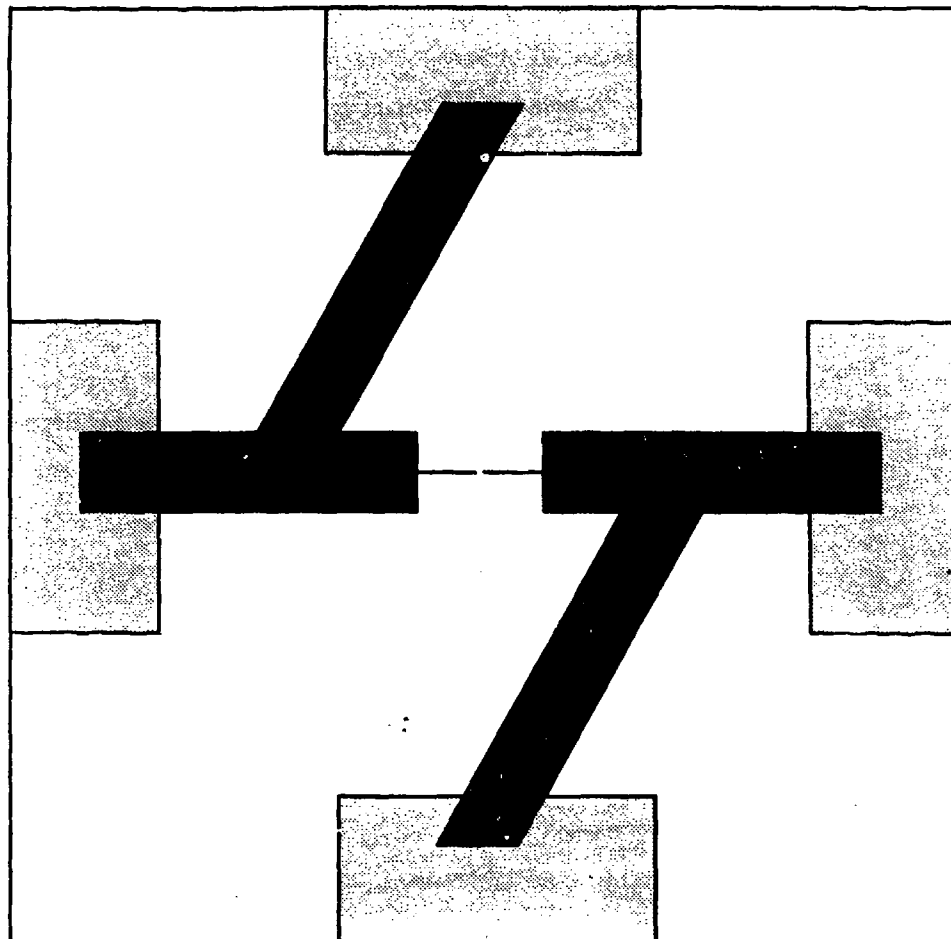
The purpose of the top resist layer is to maximize resolution, to obtain the minimum linewidth. A less sensitive resist is therefore used, (PMMA of 950 K molecular weight, dissolved at 6% in a chlorobenzene solution, available from KTI, Inc., 1170 Sonora Ct., Sunnyvale CA 94086), and spun on in a thin layer of about  $0.2\mu\text{m}$ , at 8000 rpm. The wafers are again baked at  $180^\circ\text{C}$  for one hour. The wafers are then diced in  $1/2" \times 1/2"$  pieces each containing four sets of pads, to fit in the scanning electron microscope (SEM) field of view at the lowest magnification, and taken to the SEM for exposure.

The heart of our electron-beam exposure system is a JEOL 35 U scanning electron microscope. To control the beam, and scan over the desired patterns, we interfaced an IBM Instruments 9000 microcomputer to two high-quality sixteen-bit Analogic digital-to-analog converters, which in turn were attached to the external XY input of the SEM. A set of machine language routines, written by Dr. H. Rogalla for the 68000 processor of the IBM Instruments 9000 were used to generate the coordinates for the XY control of the SEM beam. These were transmitted to the external D/A converters, which in turn transmitted an analog control signal to the SEM. A sketch of the electronics controlling the scanning electron microscope used to expose the resist is given in Appendix 1.

The two layer resist stencils were mounted on the SEM stage with silverpaint. With a beam voltage fixed at  $10\text{ kV}^*$ , and a beam current of about  $5\text{ pA}$ , the focus, astigmatism, and aperture alignment SEM settings were first optimized while looking at silver-painted areas. This was necessary since the only large distinguishable features on the wafers were the Cr-Au pads, which were covered by two layers of resist, and were therefore difficult to see sharply with the low  $10\text{ kV}$  beam voltage. The beam focus was then re-optimized while looking at dust or a scratch in the resist near the center of the pads. Next, the field of view

---

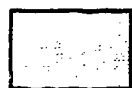
\* Depending on the age and alignment of the SEM filament, occasionally it was not possible to obtain enough beam current at  $10\text{ kV}$  to see the contact pads. In this case, the beam voltage was stepped up to  $11$  or  $12\text{ kV}$ .



Key:



Exposed pattern



Tips of contact pads

Fig. 3.6: Sketch of SEM field of view at a magnification of 1000 x, showing the contact pads and the exposed pattern.

was aligned with the center of the pads<sup>#</sup>, as the magnification was increased to 1000 x. The SEM beam was then blanked off, and control was given over to the IBM 9000 to execute the exposure of the sample. A typical setting for the exposure time per pixel was about 200  $\mu$ s. Fig. 3.6 shows a sketch of the field of view at 1000 x, and of the pattern exposed by the beam. The width of the gap in the center of the pattern, which defines the location of the resist bridge was typically 125 pixels.

The samples were developed in a 1:5 mixture of methylisobutylketone (MIBK) and isopropanol. Typical developing times ranged from five to fifteen minutes. The sample was closely monitored during this long process, and the development was stopped as soon as the resist bridge structure appeared developed under the optical microscope. The resist stencils were then ready to be mounted in the evaporator.

#### 3.1.4 Evaporation procedures

While the resist stencils can be safely stored for weeks, the completed samples must be cooled and stored at liquid helium temperatures within six to twelve hours of the evaporation, to avoid the likely growth of metallic whiskers shorting the oxide barrier. As a result, the evaporation process must be timed carefully with the planned availability of the dilution refrigerator, needed to perform the measurements.

The resist stencils were mounted on the tiltable stage of a cryopumped evaporator, the tilt being adjustable by a control outside the vacuum chamber. The chamber was pumped down to a pressure below  $4 \times 10^{-7}$  torr. Next, the sample stage was cooled by flowing liquid nitrogen for at least one hour, which would further cryopump the chamber, and cause the pressure to drop below  $2 \times 10^{-7}$  torr. The stage was then tilted by an angle of  $45^\circ$  from normal incidence, and the first electrode was evaporated. In carrying this out, the evaporator

---

<sup>#</sup> Usually the slow or even very slow SEM scan settings were necessary to see the pads well enough to align them.

boat, containing 99.999% pure Sn was heated slowly at a low setting for about five minutes. Then, the power fed to the boat was gradually increased, until a very high and stable evaporation rate of about 300 Å/sec was achieved. The shutter was then opened, to deposit about 700 - 800 Å of Sn to make up the bottom electrode of the junction.

After completing the first evaporation, the chamber was twice flushed with 20 - 40 mtorr of oxygen, 99.99% pure. The oxidation of the bottom electrode was then completed in a dc oxygen plasma, driven by a source voltage of 1.1 kV. The oxygen pressure was 40 mtorr. The oxidation time varied from 30 seconds to five minutes, depending on the desired thickness of the barrier. The chamber was again pumped down to below  $4 \times 10^{-7}$  torr. After changing the stage tilt to about  $-45^\circ$ , the top electrode of Sn was evaporated, using warmup times and deposition rates comparable to those of the bottom electrode. The top electrode was between 1000 and 1200 Å thick. If the top electrode was not made thicker than the bottom electrode, the top electrode would often break near the junction area, on the edge of the bottom electrode.

After the evaporation was completed, the sample was warmed up slowly. Typically, it was left to warm up in the chamber for about four hours. After this, approximately 1 torr of nitrogen exchange gas was bled into the chamber, to accelerate the final warming stages. After waiting two more hours, the chamber was vented to atmosphere, and the sample was unloaded. The sample was completed by lifting off the unwanted tin, by squirting the wafer with acetone. A quick methanol rinse, to wash off the acetone residue, would complete the sample preparation.

Fig. 3.7 is a scanning electron microscope photograph of a typical sample. The active junction area is the overlapping region between the two thin fingers of tin, at the center of the photograph. The bottom electrode appears fuzzier than the top electrode, since it is not as thick. Figs. 3.8 and 3.9 are photographs of an array of eleven small tunnel junctions, fabricated by patterning five overhanging resist bridges in a row. Fig. 3.9 is taken at a low enough magnification to also show the tips of the contact pads.



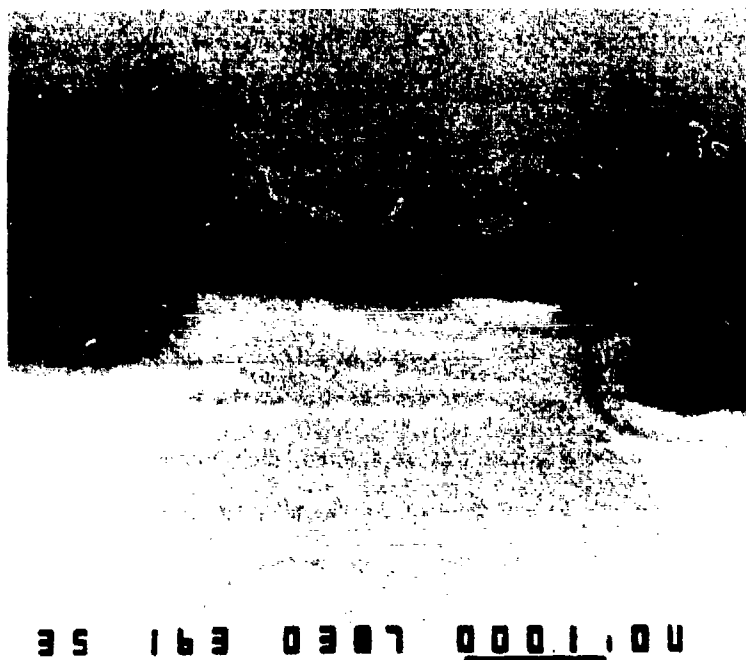


Fig. 3.7: SEM photograph of a previously measured sample with area  $\sim 0.1(\mu\text{m})^2$ , normal resistance  $R_n = 34\text{ k}\Omega$ , and capacitance  $C \approx 2\text{ fF}$ . The junction is the small overlapping region between the two "fingers" of tin, in the center of the picture. The photograph was taken at an angle of  $45^\circ$ . The horizontal bar is one  $\mu\text{m}$  long.



Fig. 3.8: SEM photograph of the eleven-junction array. The horizontal bar is 10  $\mu\text{m}$  long.

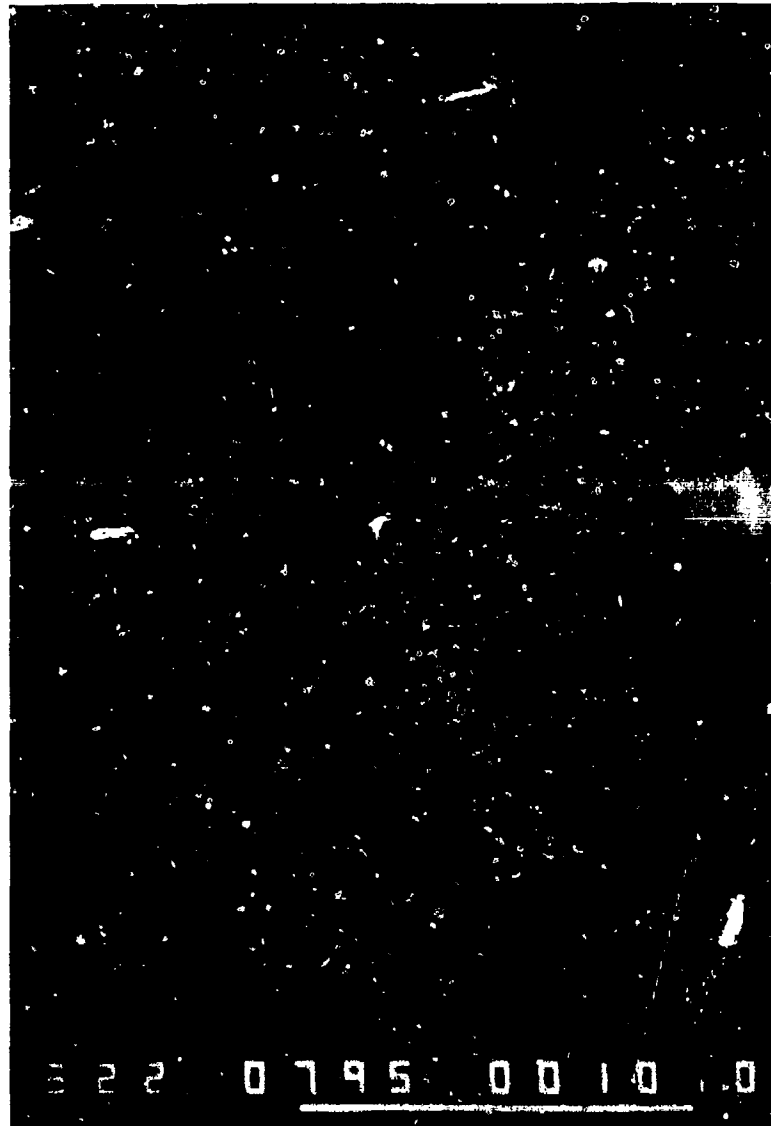


Fig. 3.9: Close-up of the eleven-junction array. The horizontal bar is 10  $\mu\text{m}$  long.

### 3.2 Measurement Techniques

#### 3.2.1 Mounting procedures

The junctions were measured in an Oxford Instruments model 200 dilution refrigerator. One of the main advantages of this refrigerator is that it has a top-loading facility. A sketch of the top-loading "slug" is shown in Fig. 3.10. The sample was mounted on the slug, and the leads were attached to the pads by pressed indium dots. The slug is attached to the refrigerator by screwing it into the bottom part of a copper tail that is thermally anchored to the mixing chamber. Electrical contact to the sample is made by means of the eight slip-rings. To load the slug, some liquid helium is first syphoned from the main bath of the dilution refrigerator to precool it. The slug is then quickly loaded in place, and can be cooled down to millikelvin temperatures in a few hours.

#### 3.2.2 Measurement set-up

A sketch of the measurement set-up is shown in Figs. 3.11 and 3.12. The samples were isolated from the environment by RLC filtering composed of 5 k $\Omega$  cold resistors, mounted on the top loading slug and the extensive distributed inductance and capacitance of the leads. The leads were composed of 40 gauge insulated Cu wire arranged in ribbons. The lead capacitance was measured to be about 1 nF. In several locations, the leads were tightly wrapped on solenoidal heat-sinking posts, which are believed to add significantly to their inductance. The measured cutoff frequency of the leads was below 1 kHz. The addition of Murata-ERIE rf low pass filters was found to add unwanted resonances in the leads, and better performance was obtained by the distributed RLC filtering. By using an audio-frequency spectrum analyzer, the measurement set-up was extensively tested for low frequency noise, and great effort was spent to minimize its contribution. The dilution refrigerator and measurement apparatus were enclosed in an

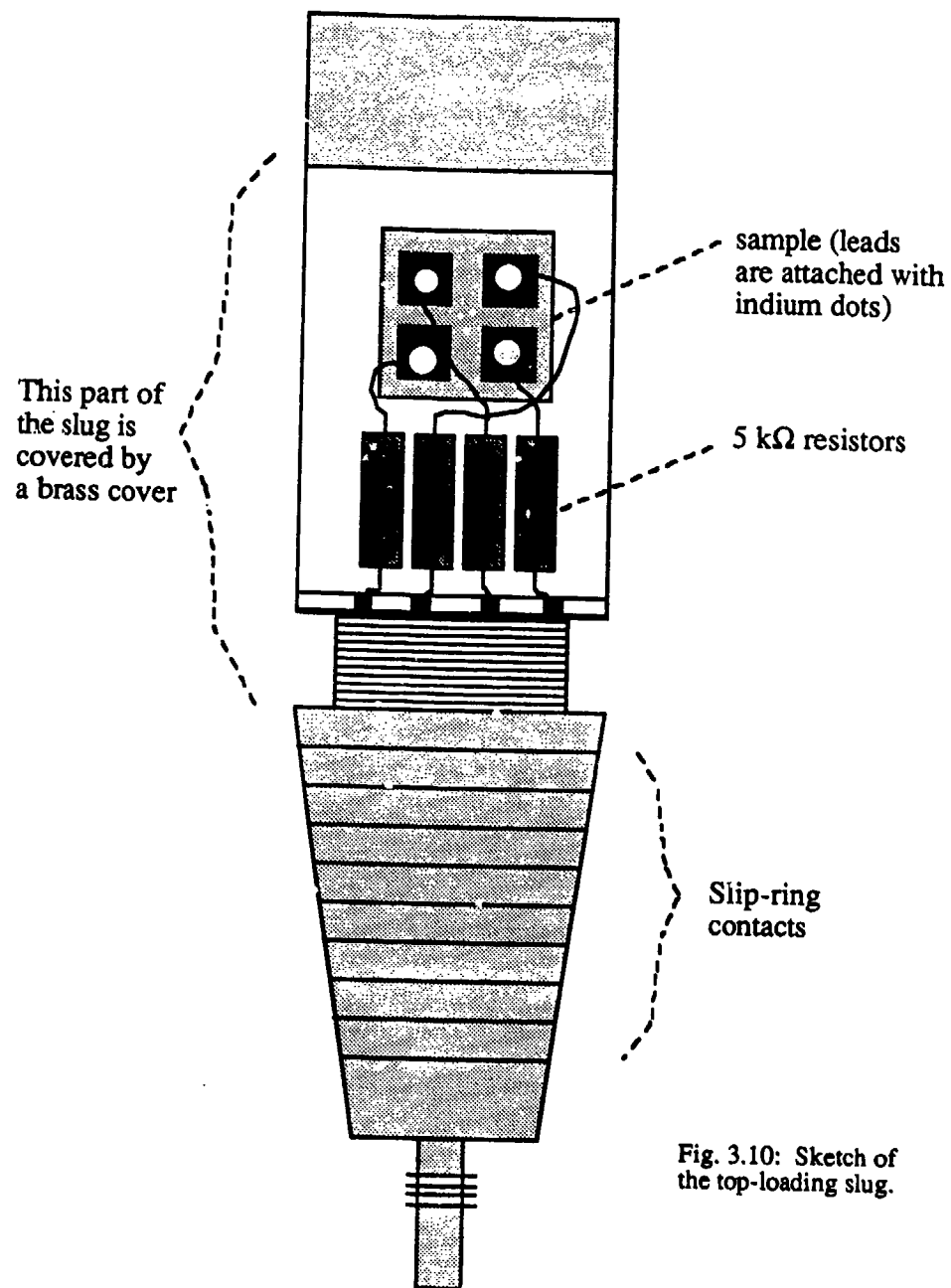


Fig. 3.10: Sketch of the top-loading slug.

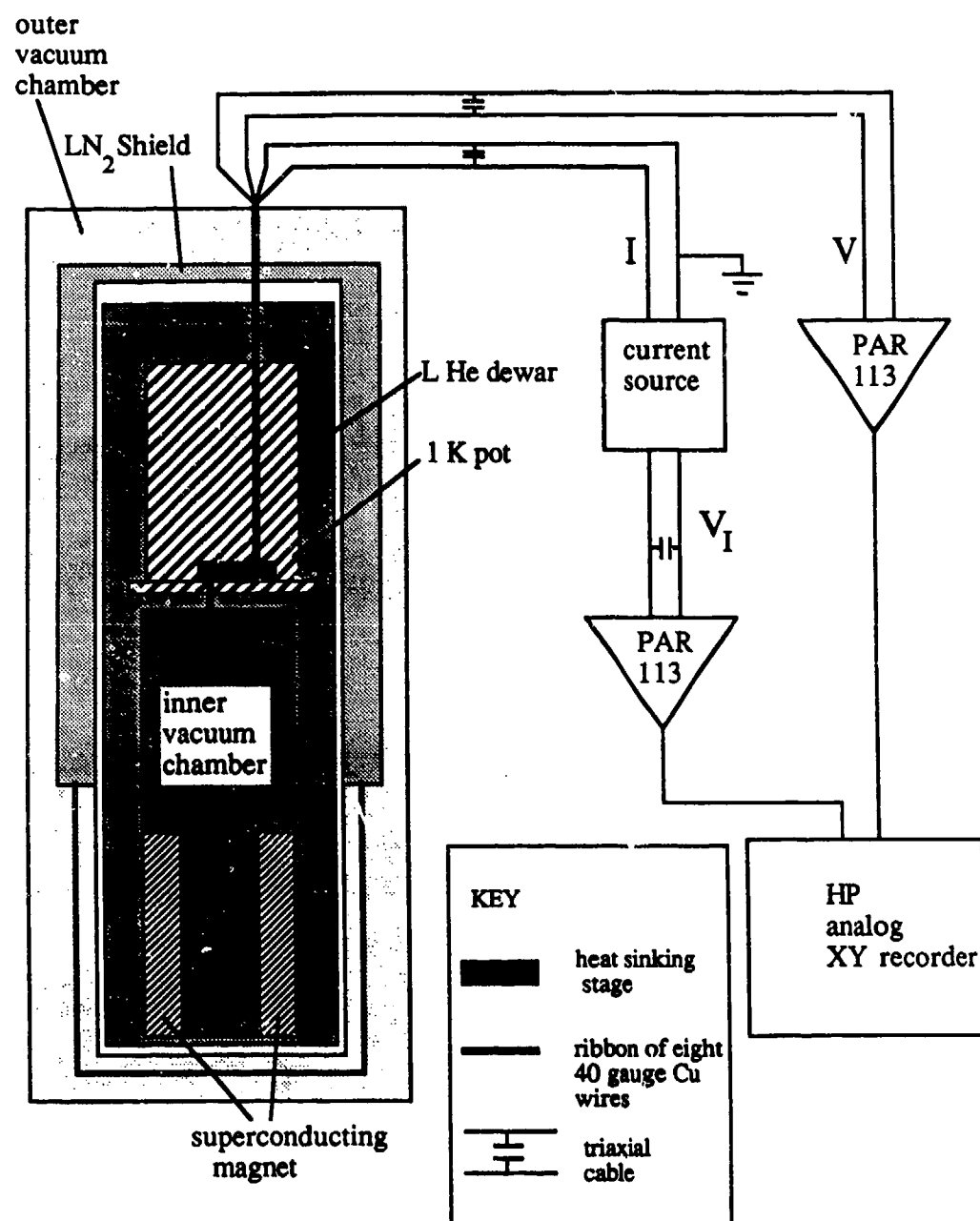


Fig. 3.11: Sketch of the measurement apparatus.  $V_I$  is the voltage measured across a calibrated resistor used to measure the current.

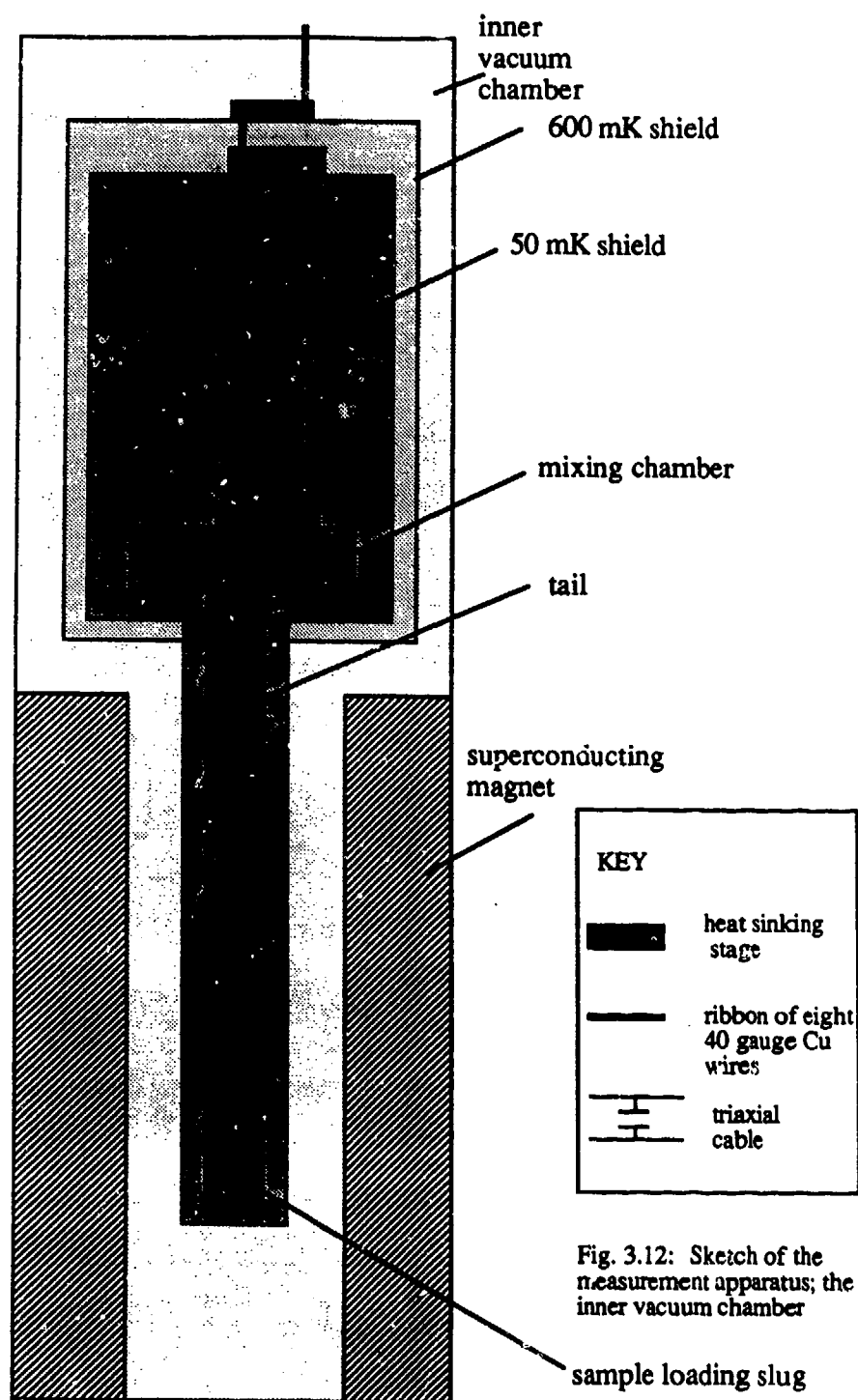


Fig. 3.12: Sketch of the measurement apparatus; the inner vacuum chamber

electrically screened room, to minimize rf pick-up. Several more layers of shielding were provided by the various copper heat shields of the dilution refrigerator set-up (see Figs. 3.11 and 3.12).

To minimize the extrinsic noise fed into the sample by the measurement set-up, the latter was kept very simple. For the I-V curve measurements, we relied on a simple current source, composed of a dry battery whose voltage was adjusted by a variable voltage divider, and a 500 M $\Omega$  current-limiting resistor. The voltage signal was amplified with a Princeton Applied Research PAR 113 preamplifier and fed into the Y input of an analog Hewlett Packard XY recorder. The current fed into the sample was measured by taking the voltage across a precision series resistor and, after it was amplified with another PAR 113, the signal was fed into the X input of the XY recorder. One of the two sample current leads was grounded at the current source. Care was taken to avoid ground loops in the measurement setup, and shielded twisted pair (Belden triax) cable was used in all connections to the sample. Using a 500 M $\Omega$  limiting resistor and a 1 M $\Omega$  measuring resistor, we were able to produce and measure currents of a few pico amperes.

A more complex computer-controlled set-up was also built, and used successfully for preliminary measurements in a conventional liquid helium pumped rig. A schematic of the computer-controlled current source, which has also been used by others, is given in Appendix 2. Its low frequency noise performance, however, was inferior to that of the simple setup described above, and it was not used for the most delicate low temperature measurements described in this report.

The  $dV/dI$  measurements were made using a PAR 124 lock-in amplifier, and a home-built voltage-current converter and level-shifter. The good noise performance of this set-up allowed the measurement of  $dV/dI$  vs  $I$  curves with excitation currents as small as 5 pA, using averaging time constants below 1 sec.



### 3.2.3 Low temperature considerations

The temperature of the mixing chamber was measured by means of calibrated resistors. Between 4 K and 250 mK we used a factory-calibrated germanium resistance thermometer (GRT) obtained from Lake Shore Cryotronics. Below 250 mK we used Speer carbon resistors, which were milled on one side to provide a flat surface, and pressed against the mixing chamber surface, using cigarette paper to provide a layer of electrical insulation. The carbon resistors were calibrated *in situ* in each cool-down using a National Bureau of Standards fixed point thermometer, consisting of five different superconductors of known transition temperatures between 250 mK and 20 mK.

To ensure that the temperature of the mixing chamber is indeed a reasonable guess for the sample temperature, we must examine some heat sinking considerations.\* There are two primary contributions to the heat-sinking of the junction: heat-sinking through the leads and through the substrate. In considering the first term, the bottleneck in the heat transfer process is given by the thin and narrow superconducting leads in the immediate proximity of the junction. For the sake of an order of magnitude estimate, we assume that this bottleneck is a tin wire of diameter 0.2  $\mu\text{m}$ , and length 10  $\mu\text{m}$ . At temperatures below 0.5 K, the thermal conductivity of tin is primarily due to phonon contributions, and is proportional to  $T^3$ . A reasonable value [Lounasmaa, 1974] at 0.3 K is 10 W/Kcm. If we multiply this value by the cross-section of the wire, and divide by the length, we obtain the maximum power allowed through the sample, to maintain a given temperature error to be of order  $4 \times 10^{-10}$  W for an error of 1 K. Since the conductivity is proportional to  $T^3$ , at 30 mK this value is reduced to  $4 \times 10^{-13}$  W/K. Therefore, if we can tolerate a maximum temperature error of 2 mK, we can feed a maximum of about one fW to the junction. To measure a critical current of order 200 pA, given that the sample has a low current resistance  $R_0 \sim 10$  k $\Omega$ , the power fed to the sample is of order 0.5 fW. The heat sinking of

---

\* Good references are Lounasmaa [1974] and Richardson and Smith [1988].

the junction through the leads should thus be effective, and the temperature of the sample should be within a few mK of the temperature of the mixing chamber.

A good approximation [Richardson and Smith, 1988] for the thermal boundary resistance from a metallic to an insulating medium is  $30 \text{ K}^4\text{cm}^2/\text{W}$ . At 0.3 K, for a  $0.2 \text{ } \mu\text{m} \times 0.2 \text{ } \mu\text{m}$  interface cross-section, the approximate area of the junction, the maximum power allowed for a given temperature error is thus of order  $4 \times 10^{-11} \text{ W/K}$ , which is about a factor of ten worse than the estimate due to the lead contribution. It thus appears that the leads are a better heat-sinking mechanism than the substrate. Naturally, however, the two mechanisms interact with each other, and the heat can be carried off part way through the leads and part way through the substrate. The conclusion is this: if we only feed a power of order 1 femtowatt to the junction in order to measure its properties, we should be relatively safe in trusting the readings of the thermometers on the mixing chamber. This is confirmed by the sharp temperature dependence of our measurements, reported in Chapter 4, all the way down to below 20 mK. The only exception are the measurements on the eleven junction linear array, in which the five highly resistive junctions (with thick oxide barriers) on each side of the measured device are likely to render the heat sinking much less effective.

## CHAPTER 4

### EXPERIMENTAL RESULTS

This chapter describes our experimental results. We performed measurements on a total of eleven samples: five single-junction samples, five two-junction linear arrays, and one eleven-junction linear array. Sample parameters are given in Table 4.1. We have divided the presentation of the results into four sections. We first describe, in Section 4.1, the most basic results from I-V curve measurements performed on the junctions at zero magnetic field; here we present a number of striking observations, such as a reentrant critical current temperature dependence, and a significant resistive region (with  $R = R_0$ ) at  $I < I_c$ . In Section 4.2 we discuss the effect of applying a magnetic field to the junctions: the field dependence of  $I_c$  and  $R_0$ , the appearance of a novel regime in which features of the Coulomb blockade and Josephson tunneling coexist, and the high field region in which superconductivity is destroyed. Section 4.3 completes the presentation of results with a discussion of the measurements performed on the eleven-junction array. Section 4.4 ends the chapter by summarizing the experimental results, setting the stage for the discussion to be given in Chapters 5 and 6.

#### 4.1 Basic Junction Characterization

This section is the core of this report. Here we discuss the most basic properties of our small devices, and begin to differentiate them from conventional low capacitance Josephson junctions.

##### 4.1.1 Current-voltage characteristics

We begin the presentation of our experimental results with a typical plot, shown in Fig. 4.1, of the low temperature I-V characteristics for a junction with  $R_n \approx 140 \text{ k}\Omega$ . The

Table 4.1: Sample parameters.  $R_n$  is the normal resistance of the junction.  $R_{LO}$  is the low temperature leakage resistance.  $T_{min}$  is the lowest temperature at which measurements were carried out. Area is the area of the sample, from SEM photographs.  $C$  is the capacitance of the sample;  $C$  was estimated by Coulomb blockade measurements in samples 4, 5, 8, and 11; for the other samples, the estimate  $C$  was given by the geometrical capacitance.  $E_j$  is the  $T=0$  Josephson energy and  $E_c$  is the single electron charging energy, defined in the text.  $N_{JJ}$  is the total number of junctions present in a sample; the junctions were patterned in a linear array and the quoted measurements correspond to the lowest  $I_c$  (highest resistance) junction in the array.

Sample	$R_n$ (k $\Omega$ )	$R_{LO}$ (k $\Omega$ )	$T_{min}$ (K)	Area [ $(\mu m)^2$ ]	$C$ (fF)	$E_j$ (K)	$E_c$ (K)	$N_{JJ}$
1	0.52	10	1.4	0.1	2	40	0.45	2
2	3.4	105	1.8	0.15	3	6.2	0.3	1
3	6.5	3000	0.85	0.4	7	3.2	0.15	2
4	8.5	4000	0.02	0.15	3.5	2.7	0.3	1
5	14.8	2860	0.02	0.1	2.5	1.4	0.35	1
6	30	2500	1.3	0.025	<1	0.7	>0.9	2
7	~30	-	0.02	0.1	2	0.7	0.45	11
8	34	2400	0.02	0.1	2	0.6	0.45	1
9	70	40000	0.02	0.04	1	0.3	0.9	2
10	110	-	0.02	0.05	1	0.19	0.9	2
11	140	300000	0.02	0.05	1	0.15	0.9	1

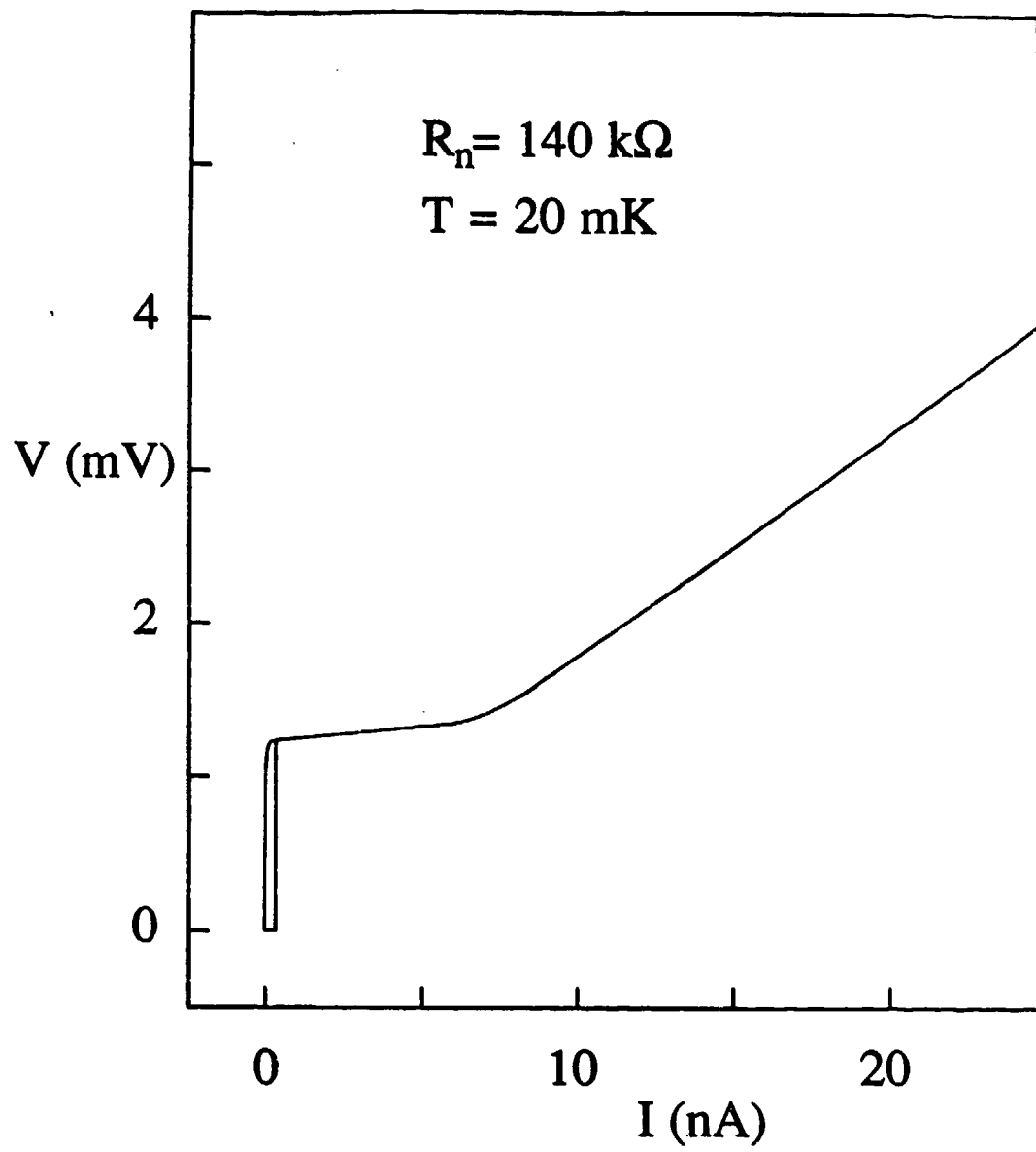


Fig. 4.1: Low temperature I-V characteristics of the sample with  $R_n = 140 \text{ k}\Omega$ .

characteristics are those of a high quality junction, with very sharp gap structure, and very low leakage current. Values for the low temperature subgap leakage resistance  $R_L$  are given in Table 4.1.

While the sharp characteristics might remind us of a good conventional tunnel junction, such as we described in Chapter 2, a closer look at the I-V curve already reveals some unusual phenomena. First of all, the value of the energy gap  $V_g$  measured from the I-V curve [ $V_g \approx 1.3 \text{ mV}$ ] appears too high for a junction with tin electrodes. Since the measured  $T_c$  of this device was about  $3.75 \text{ K}$ , a good value for Sn, we would expect from Bardeen-Cooper-Schrieffer theory to have a gap value  $2\Delta/e \approx 1.764 kT_c/e \approx 1.16 \text{ mV}$ . At the same time, the linear high voltage part of the I-V curve does not extrapolate back to the origin. The vertical offset is about  $100 \mu\text{V}$ , as can be determined with good accuracy by looking at the I-V curve on different scales. This vertical offset of the extrapolated line at the origin matches approximately with the gap estimate discrepancy. It is also in good agreement ( $\pm 20\%$ ) with the value of  $e/2C$  for this device.<sup>§</sup> Our interpretation is that we are witnessing the effect of the Coulomb blockade, indicated schematically in Fig. 1.2 (c), described in Chapters 1 and 2. The theme of this work is already apparent. While our devices share many characteristics with conventional Josephson junctions, a number of striking novel phenomena can be observed, which we attribute to the effect of a large charging energy  $E_C$ .

Fig. 4.2 is another plot of the I-V characteristics of the junction with  $R_n = 140 \text{ k}\Omega$ , also taken at  $T = 20 \text{ mK}$ . The scale is more sensitive, and the critical currents and low current resistance  $R_0$  (notice the top plot on the expanded voltage scale) can be accurately read off. This plot is similar to Fig. 1.3, an I-V curve of a junction with  $R_n = 70 \text{ k}\Omega$ , already described in Chapter 1. The estimated value of  $x = E_C/E_J$  for this sample is about 6. The features of this curve, such as a large hysteresis and a significant  $R_0$ , are typical for the

---

<sup>§</sup> The value of  $C$  is given by the intrinsic capacitance  $C_i$ , estimated as described below, in Section 4.1.4.

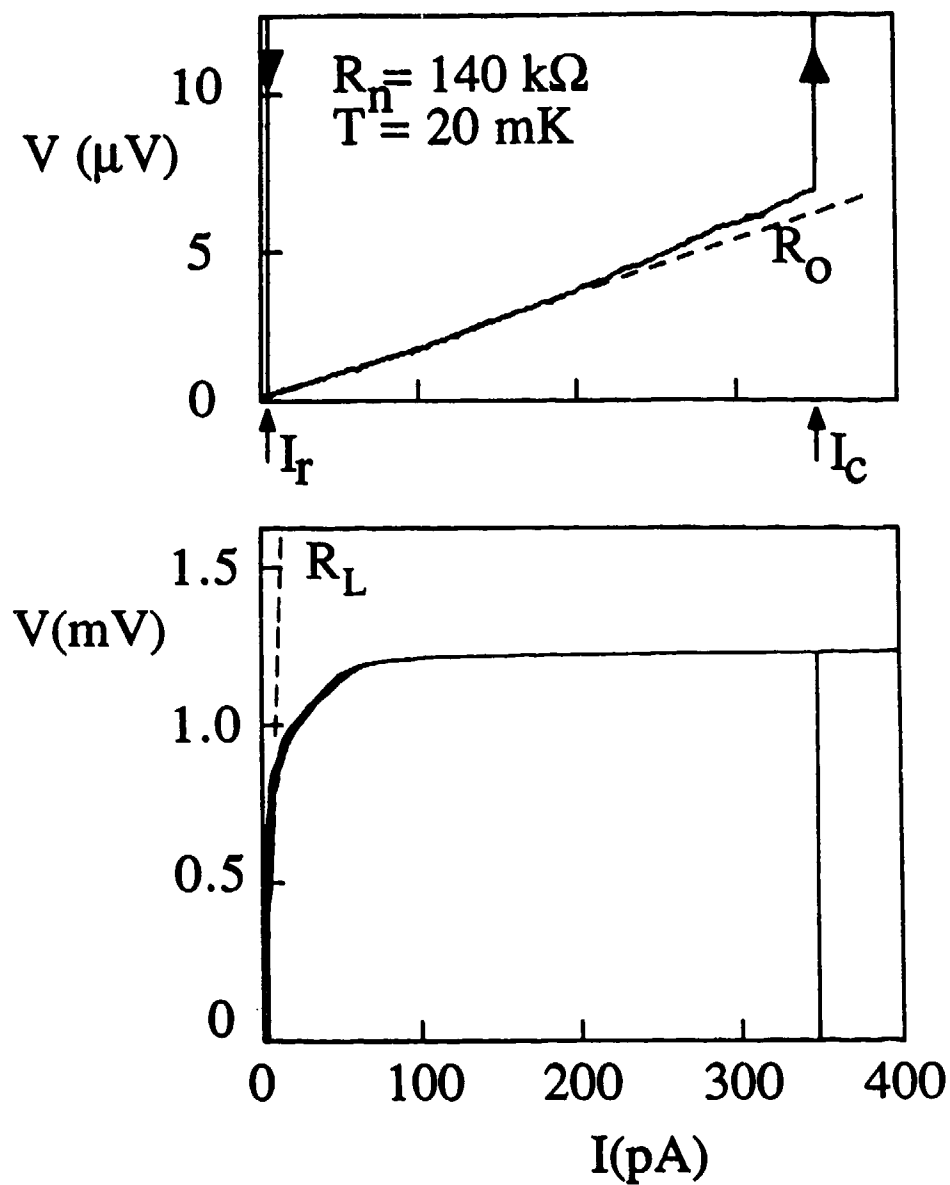


Fig. 4.2: I-V curve of a sample with  $R_n = 140 \text{ k}\Omega$  and estimated capacitance  $C = 1 \text{ fF}$ , taken at  $T = 20 \text{ mK}$  and  $H = 0$ , showing definitions of  $I_c$ ,  $I_r$ ,  $R_O$ , and  $R_L$ . The two plots have the same horizontal scale but different vertical scales.

low temperature behavior of the high resistance, low capacitance junctions reported in this work. Similar I-V curves were also observed by Ono, *et al.* [1987].

#### 4.1.2 The junction critical currents

The I-V curve in Fig. 4.2 displays *two* different measurable critical currents,  $I_c$  and  $I_r$ .  $I_c$  is the maximum current that can be carried before the jump into the high voltage regime.  $I_r$ , the recapture critical current, is the current at which the system returns to the low voltage state. The familiar "zero voltage state" is *not* found in this type of junction. The behavior of the system is always observably dissipative, and can be characterized by the resistances described below. Our definitions of critical currents are thus modified from the standard ones and are motivated by the need to describe our observations. Our interpretation of these critical currents is developed in the remainder of this report. At higher temperatures, the measured I-V curves were not found to be hysteretic. In this case  $I_c = I_r$ , and we *define* the measured critical current to be the  $V=0$  extrapolation of the increasing current branch of the I-V curve below the gap voltage.

In an ideal device, neglecting fluctuations,  $I_c$  is given by the value  $I_{co}$  related to  $E_J$  by  $E_J = \pi I_{co} / 2e$ , where  $I_{co}$  monotonically increases with decreasing temperature, as described in Chapter 2. In Fig. 4.3, we display the temperature dependence of  $I_c$  and  $I_r$  for the junction with 140 k $\Omega$  normal resistance. Note the remarkable temperature dependence of  $I_c$ , first rising, then dropping by a factor of ten, then rising again by a similar factor as  $T$  is reduced. This is very different from the monotonic rise of  $I_{co}(T)$ . Moreover, the measured value ( $I_c \approx 0.36$  nA) at low temperatures is much less than the theoretical  $I_{co}(T=0) \approx 7$  nA. The inset in Fig. 4.3 is an enlargement of the low temperature region: the temperature dependence of  $I_c$  is very sharp down to the low millikelvin region, where it appears to flatten off a bit. Another important observation is that the plotted  $I_c$  values are averages over a very *narrow* distribution of switching currents measured on repeated



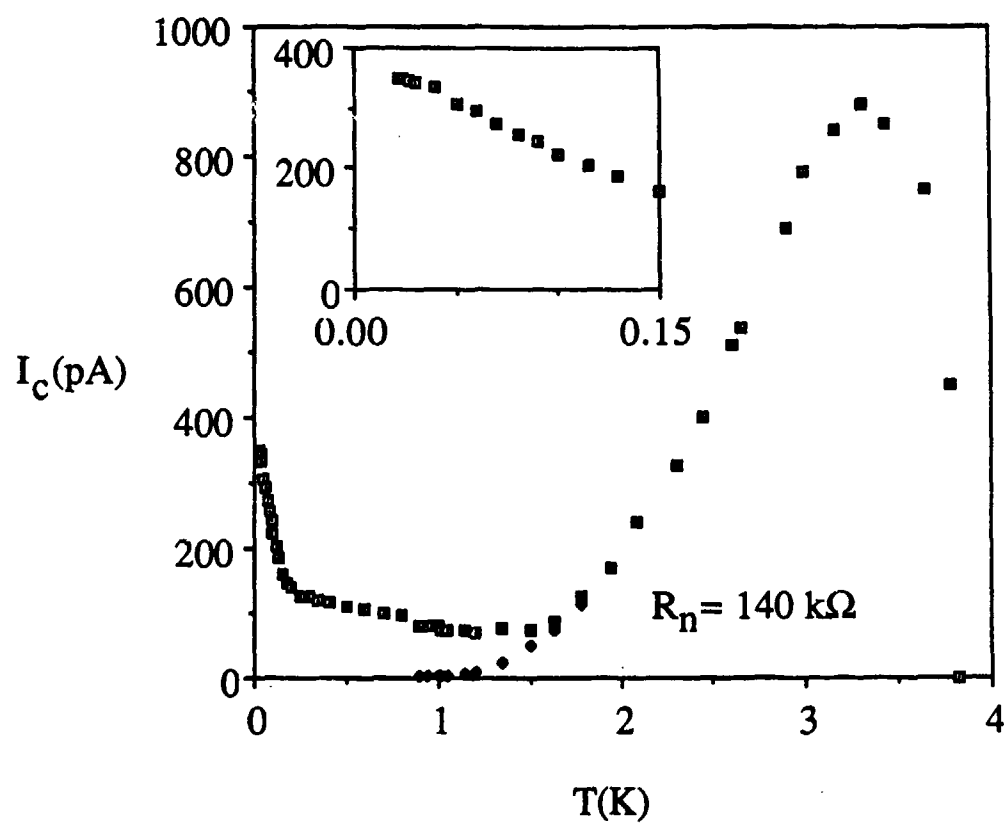


Fig. 4.3:  $I_c$  vs.  $T$  for the sample with  $R_n = 140 \text{ k}\Omega$ . The inset focuses on the low temperature measurements.

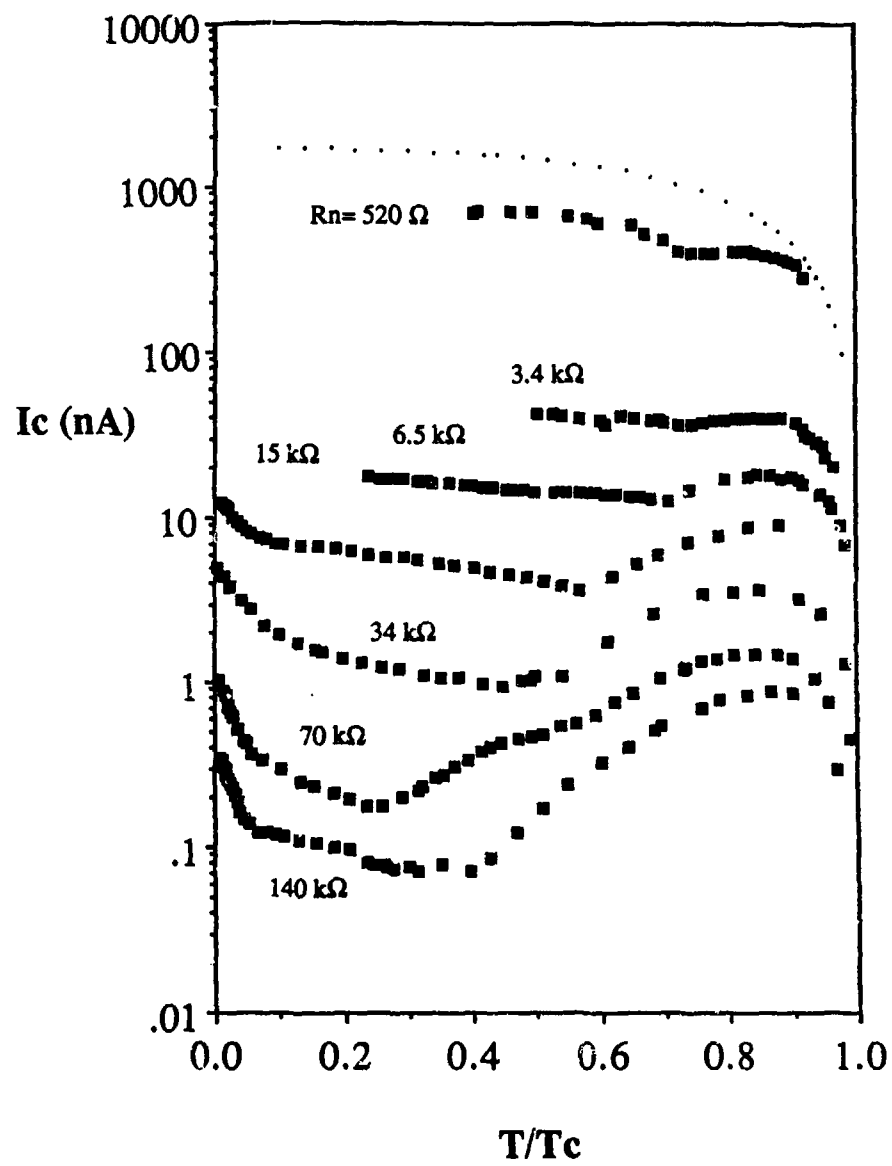


Fig. 4.4:  $I_c$  vs.  $T$  for seven different samples. The normal resistance of each sample is shown. The dotted line is  $I_{c0}(T)$  for the sample with  $R_n = 550 \Omega$ .

sweeps, with width  $\Delta I_c$  of only  $\sim 0.05 I_c \approx 0.003 I_{c0}$ . Note that  $I_c = I_r$  for  $T/T_c > 0.5$ , where the I-V curve is not hysteretic.

In Fig. 4.4, we display the temperature dependence of  $I_c$  for a number of different samples. The striking nonmonotonic behavior sets in as the sample resistance becomes of the order of  $10\text{ k}\Omega$ . Our lowest resistance junctions exhibit a monotonic temperature dependence. Moreover, the measured critical current depression is not as marked as in the high resistance samples, and can be accounted for quite well by conventional premature switching arguments. It appears clear from Fig. 4.4 that the trend of the results presented here is not dependent on the sample configuration. Some of the  $I_c(T)$  curves plotted in Fig. 4.4 are from single junction samples, while others are the lowest  $I_c$  measured in a two junction sample: the general results from these two families of samples seem quite mutually consistent.

#### 4.1.3 The junction resistances

The behavior of our smallest devices always appears dissipative; to describe it, we discuss *three* directly measurable resistance values. Using the sample in Fig. 4.2 as an example, we have the normal state resistance  $R_n \approx 140\text{ k}\Omega$ , the low voltage resistance  $R_o$  (which ranges from  $140\text{ k}\Omega$  near the transition temperature  $T_c$  down to  $\sim 6\text{ k}\Omega$  as  $T \rightarrow 0$ ), and the subgap leakage resistance  $R_L$  (ranging from  $140\text{ k}\Omega$  at  $T_c$  up to  $40\text{ M}\Omega$  as  $T \rightarrow 0$ ). The latter is defined by the slope of the quasilinear part of the decrease in  $V$  from the gap voltage, measured on an expanded current scale.

In Fig. 4.5, we display the temperature dependence of  $R_o(T)$ , for this sample with  $R_n = 140\text{ k}\Omega$ .  $R_o$  is large at all temperatures: as  $T$  is reduced below  $T_c$ , where  $R_o = R_n$ ,  $R_o$  drops, slowly at first, and then more sharply below  $0.5\text{ K}$ , apparently flattening out at the lowest temperatures. The inset shows the low temperature region. Fig. 4.6 is a plot of  $R_o$  vs.  $T$  for a number of different samples. While for low resistance samples  $R_o$  soon becomes immeasurably small below  $T_c$ , resembling the behavior of conventional devices,

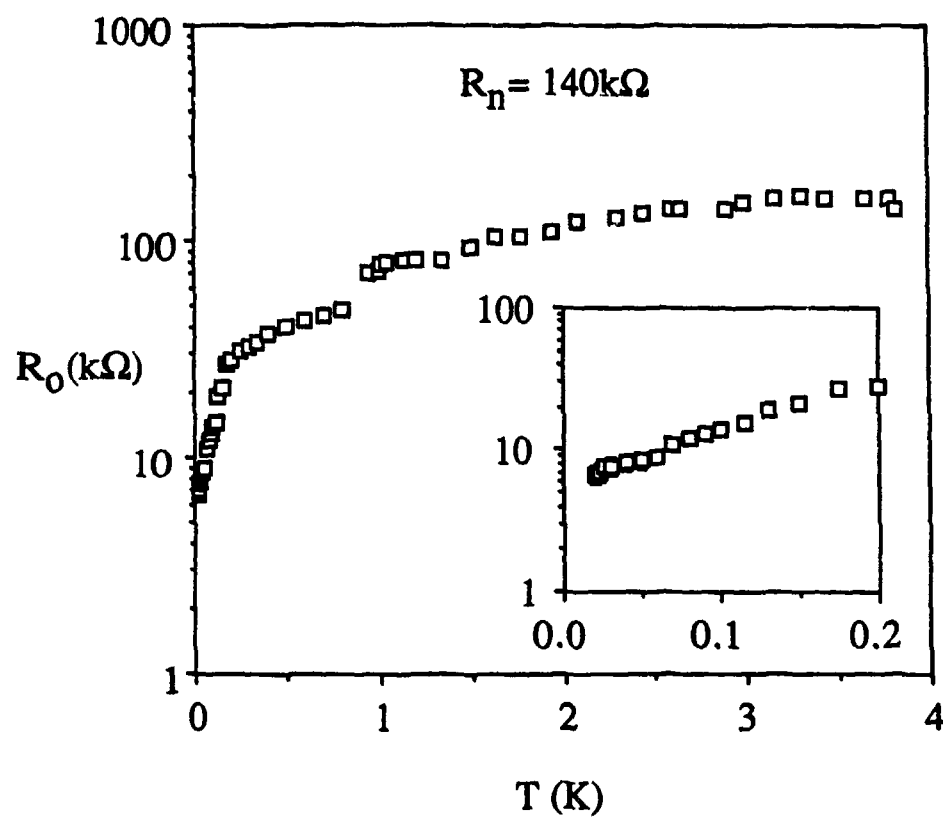


Fig. 4.5:  $R_O$  vs.  $T$  for the sample with  $R_n = 140 \text{ k}\Omega$ . The inset is a blow-up of the low temperature region.

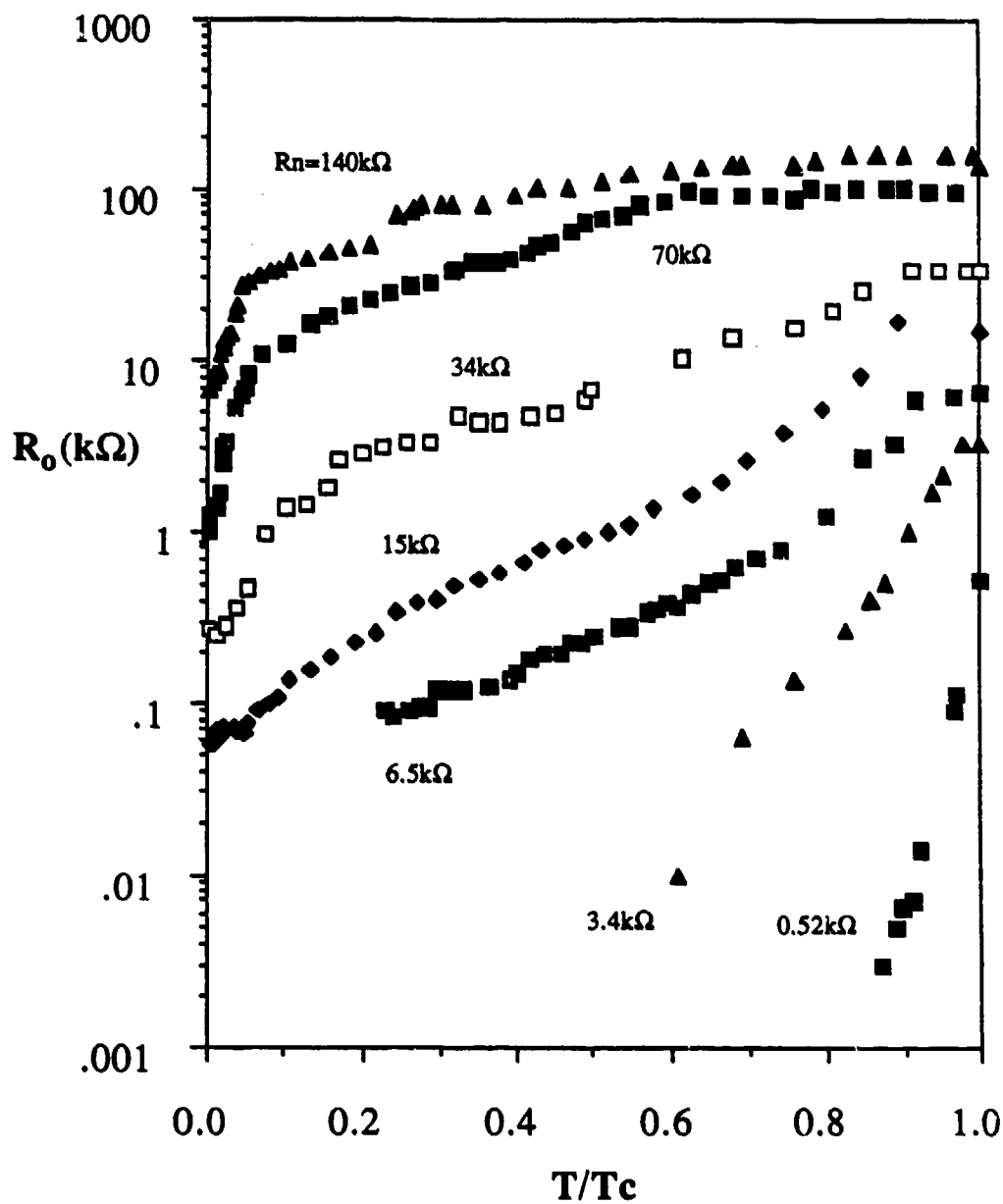


Fig. 4.6:  $R_o$  vs.  $T$  for seven samples. For  $T$  below  $\sim 0.85 T_c$  for the sample with  $R_n = 520 \Omega$ , and below  $0.60 T_c$  for the sample with  $R_n = 3.4 k\Omega$ ,  $R_o$  was below our experimental resolution.

as  $R_n$  becomes of the order of  $10\text{ k}\Omega$ , the behavior changes, and  $R_o$  is significant over the whole temperature range.

Fig. 4.7 shows a plot of the measured  $R_L$  vs  $T$  for a typical sample. For our samples, the leakage resistance is found to be well approximated by a shunt combination of a thermally excited quasiparticle term  $\sim R_n e^{\Delta/KT}$  and a residual conductance at  $T=0$ .

$$R_L^{-1}(T) \approx R_L^{-1}(0) + R_n^{-1} e^{-\Delta/KT} \quad (4.1)$$

In all measured samples, the oxide barriers were found to be of very high quality, with  $R_L(0) \sim 100 - 10,000 R_n$ . The measured low temperature leakage resistance  $R_L(0)$  is plotted in Fig. 4.8 as a function of  $R_n$ . The trend is for  $R_L(0)$  to be roughly proportional to  $R_n^2$ , as discussed further in Chapter 5.

#### 4.1.4 Junction "intrinsic" capacitance

An important part of our analysis is the estimation of the *intrinsic* capacitance of the junction. The intrinsic capacitance  $C_i$  cannot be directly extracted from I-V curve measurements. It is defined in this context as the capacitance due *only* to the parallel plate geometry of the superconducting electrodes separated by the oxide barrier through which the tunneling occurs, and is thus given by  $C_i = \epsilon_o \epsilon_r A/d$ .  $A$  is the junction area, obtained from scanning electron microscope photographs. To complete the estimate, we use a dielectric constant  $\epsilon_r \approx 6$  typical<sup>§</sup> of SnOx barriers grown by glow discharge, and a barrier thickness  $d \approx 25 \pm 5 \text{ \AA}$ , which is quite reasonable for our junctions, given their very low current density (and thick barriers). Table 4.1 contains a list of sample capacitance estimates. In general, the intrinsic capacitance is not necessarily an accurate estimate of the capacitance of a device, since parasitic contributions may be important. In our case, it appears that  $C_i$  agrees rather

---

<sup>§</sup> See Wang and Gailey [1978], and Danchi [1982].

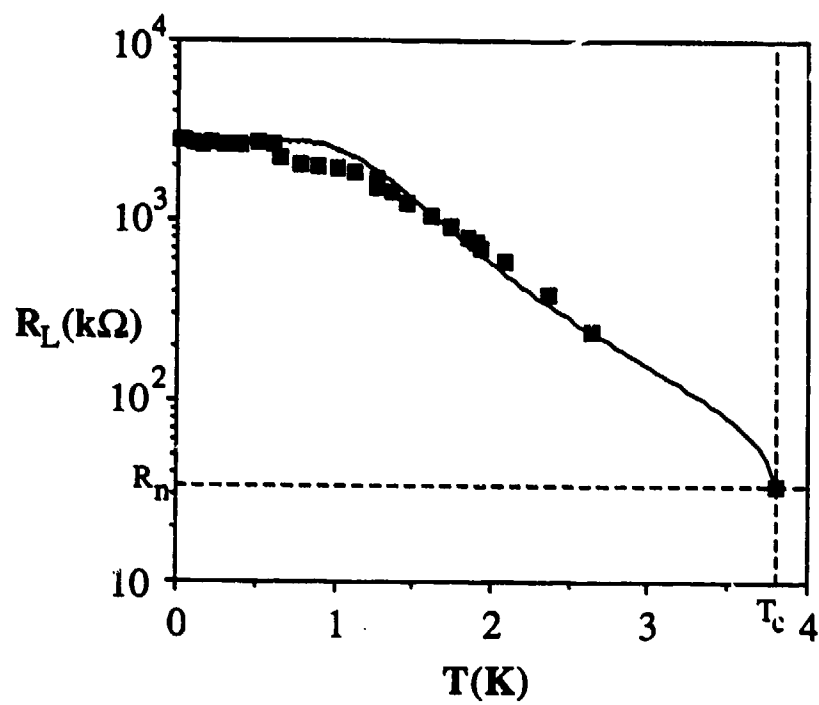


Fig. 4.7:  $R_L$  vs.  $T$  for the sample with  $R_n = 34 \text{ k}\Omega$ . The solid line is the fit using Eq. (4.1).

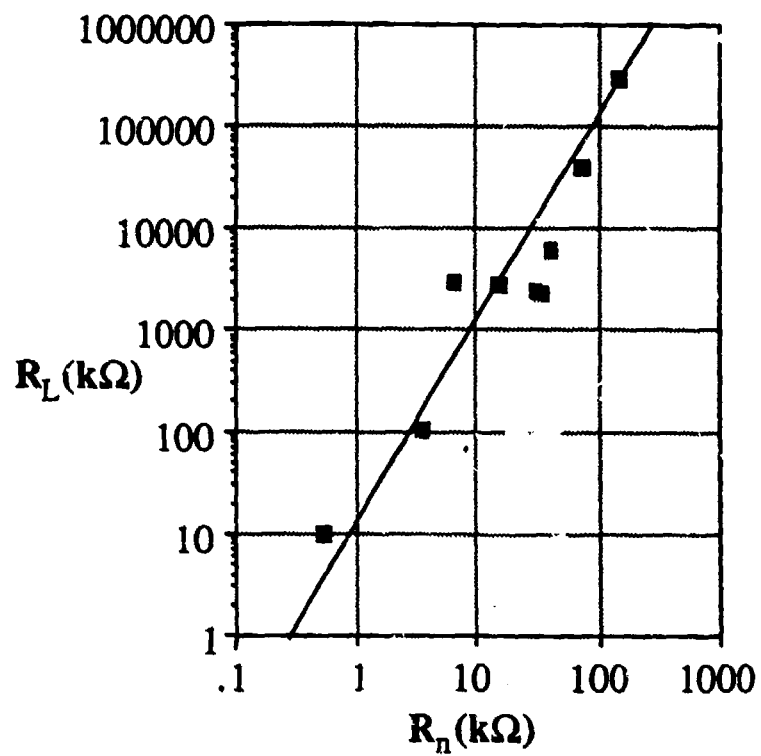


Fig. 4.8: Low temperature leakage resistance vs. the normal resistance for all measured junctions. The solid line has slope 2 and indicates the trend of proportionality between  $R_L$  and  $R_n^2$ .



well† with capacitance estimates extracted from fits with our theoretical models. An example is given above in Section 4.1.1; many more examples will follow. In the following chapters, unless we specify otherwise, we use  $C_i$  as the estimate for the total capacitance of the device.

## 4.2 Measurements in a Magnetic Field

Applying a magnetic field  $H$  to the sample reduces the Josephson coupling between the electrodes by phase modulation and by reducing the energy gap, both leading to a smaller effective  $E_J$ . By increasing  $H$  we can thus conveniently change the ratio  $x = E_C/E_J$  *in situ*, which profoundly affects the behavior of the Josephson system, as described in Chapter 2. The effects of this field modulation at low and moderate fields are described in Sections 4.2.1 and 4.2.2. In Section 4.2.3, we describe a more extreme field regime, in which  $H$  is apparently large enough to destroy the superconductivity in the tin junction electrodes.

### 4.2.1 Field dependence of $I_c$ and $R_0$

A typical low temperature  $I_c$  vs  $H$  curve is shown in Fig. 4.9. In almost all our junctions, the magnetic field monotonically reduced  $I_c$ . We ascribe this absence of the ideal  $\sin x/x$  dependence to the non-uniformity of the device. Since part of the junction area is on the edge of the electrode and part on top, the field orientation is different in different parts of the device. Moreover, in a junction of this sort, fabricated using very long oxidation times, we expect the distribution of the current through the barrier to be nonuniform.

---

† the agreement is usually within 20 or 30 %, which roughly corresponds to the error in estimating  $C_i$ .

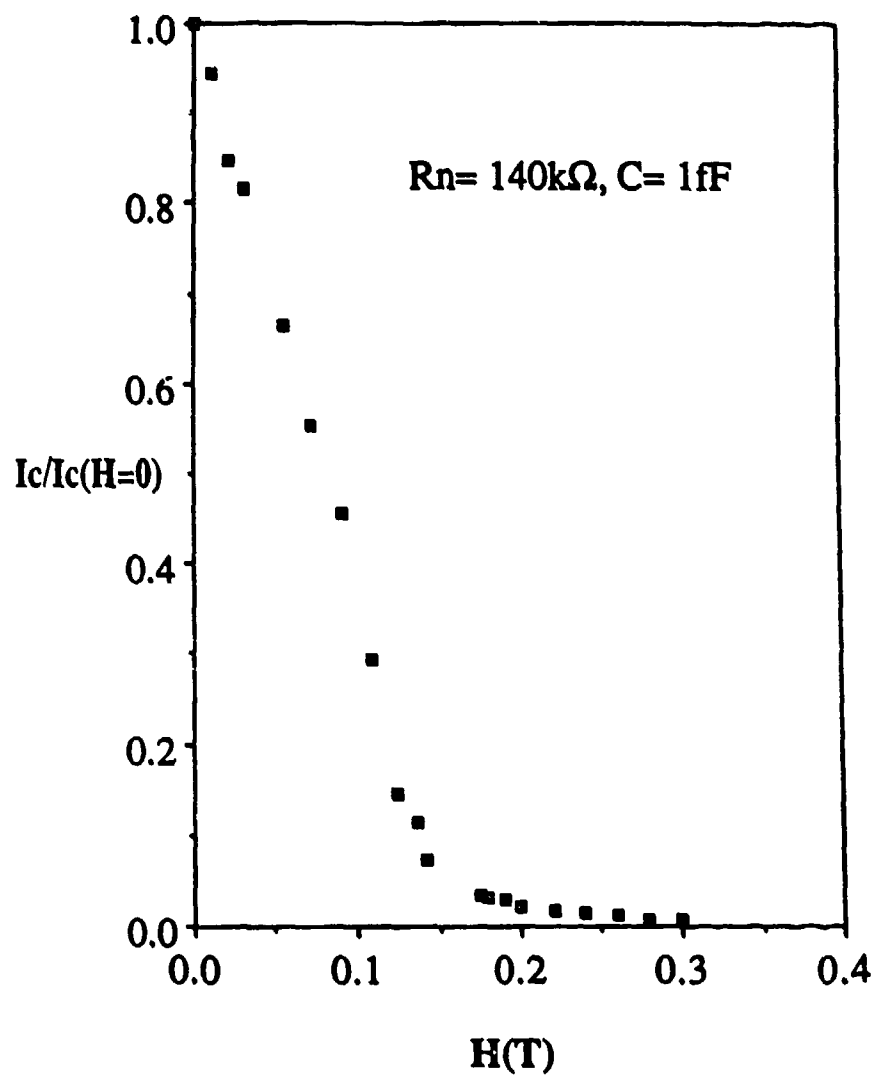


Fig. 4.9:  $I_c$  vs.  $H$  for the sample with  $R_n = 140 k\Omega$ . The critical currents are normalized to the value in zero magnetic field.

As we show in Chapters 5 and 6, the relationship between  $I_c$  and  $E_J$  in the large  $x$  regime is *not* the simple  $I_c = (2e/\hbar) E_J$ , valid in the classical approximation at zero temperature. A new expression is derived there which establishes the proportionality of  $I_c(T=0)$  to  $E_J^2$ , for  $x \gg 1$ . A brief discussion is also given there of the likely dependence of  $I_c$  on temperature. In all cases  $I_c$  appears dependent on the extent to which the phase wavefunction is "bound" to the Josephson potential, and decreases as the height of the potential barrier decreases. We thus assume that a *monotonic* relation exists between  $I_c$  and  $E_J$  in all regimes of a Josephson junction, including the large  $x$  regime. Therefore, an applied  $H$  can be used as a very powerful tool to change the barrier height of the Josephson potential.\*

The inset of Fig. 4.3 is an enlargement of the low temperature section of  $I_c(T)$ , which appears to flatten out below  $T \sim 50$  mK. A similar behavior is observed in the low- $T$  measurements of  $R_0$ , shown in the inset of Fig. 4.5. Three possible reasons for this behavior come to mind: A significant extrinsic noise contribution could be adding a fixed additional noise temperature. The sample heat sinking could be imperfect, causing a fictitious sample temperature above the mixing chamber temperature measured by the thermometers. Finally, quantum fluctuations could be dominating the response of the sample at low temperatures.

Fig. 4.10 shows the low temperature critical current plotted as a function of  $T$ , for three moderate magnetic field values. Fig. 4.11 shows  $R_0$  at low temperatures, for different values of  $H$ . Apparently, the shape of the curves is field dependent, and the low temperature flat section seems to disappear as the field is increased. This would exclude the first explanation (at least in its simplest form), since a sharp temperature response can be obtained down to 20 mK, in the  $H = 1.3$  kG plot. The second explanation also seems to

---

\* A magnetic field has been used in a similar fashion by a number of groups including Devoret, Martinis, and Clarke [1985], for MQT experiments, and Hu, Lobb, and Tinkham [1987], for chaos measurements.

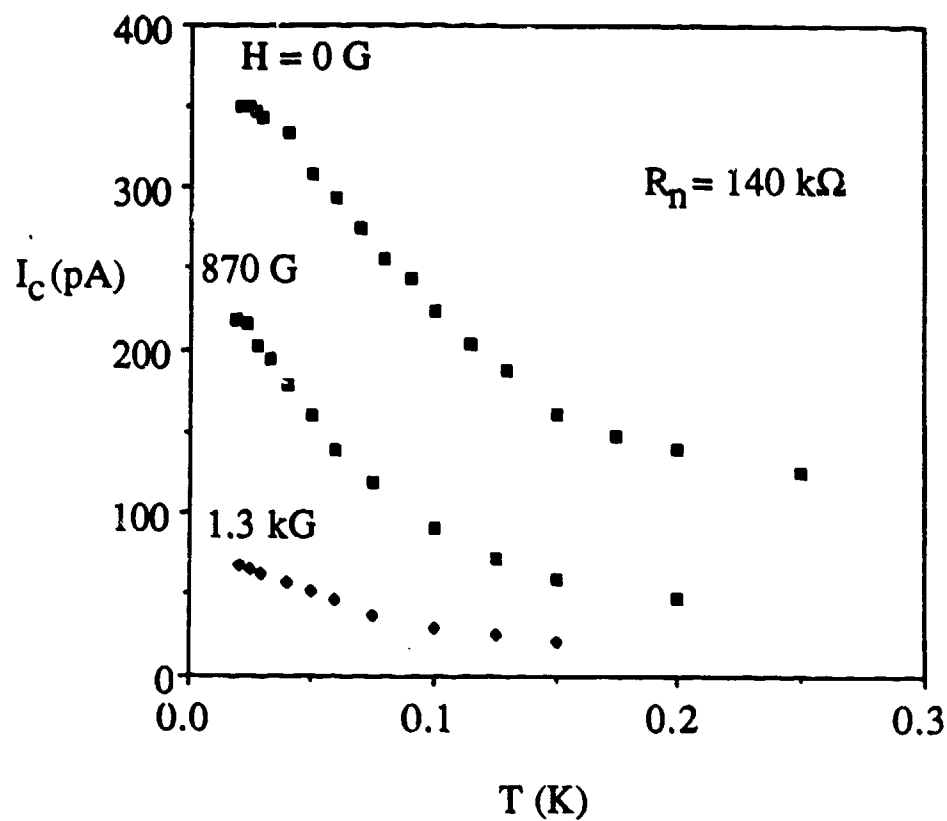


Fig. 4.10: Low temperature  $I_c$  vs.  $T$ , for different values of  $H$ , for the sample with  $R_n = 140$  k $\Omega$ .

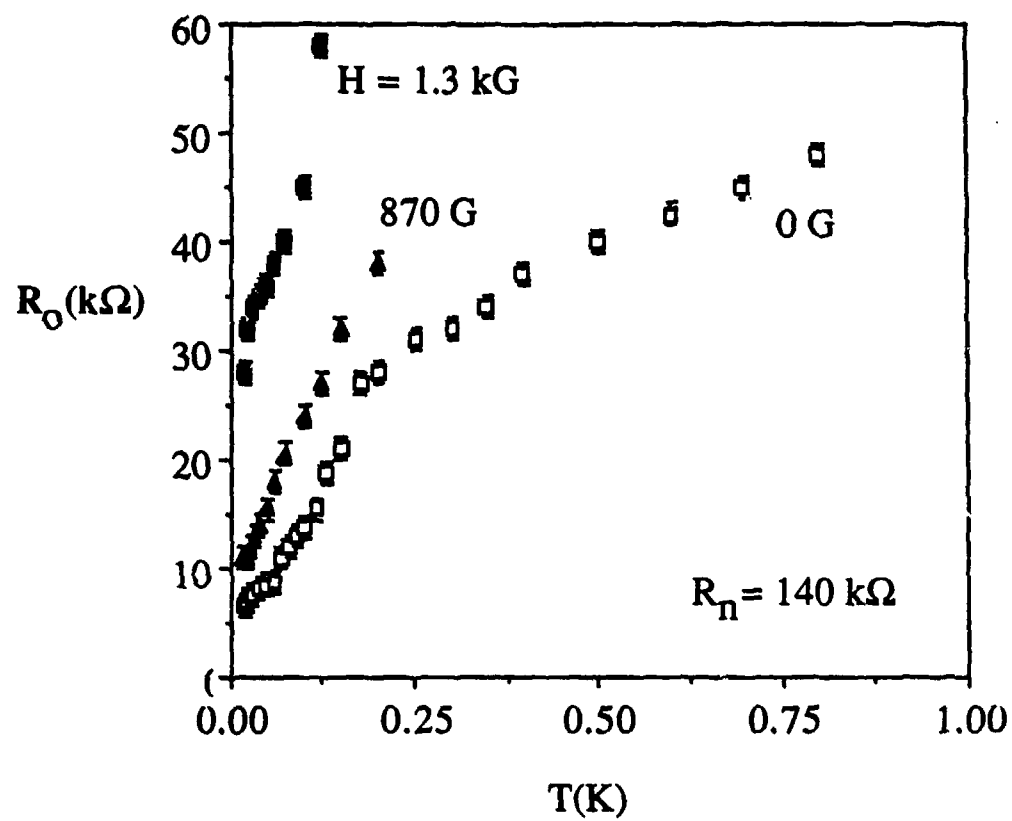


Fig. 4.11: Low temperature  $R_0$  vs.  $T$ , for different values of  $H$ , for the sample with  $R_n = 140 \text{ k}\Omega$ .

be inappropriate, for the following reasons: The power fed into the sample to measure  $R_0$  or  $I_c$  is essentially constant.\* As a result, imperfect sample heat sinking would also apparently add an additional temperature to the sample, independent of  $H$ . This is incompatible to the measurements performed at 1.3 kG.

The remaining explanation attributes the low temperature flattening of  $R_0$  and  $I_c$  to quantum fluctuations. The semiclassical underdamped limit result is, roughly speaking, for quantum fluctuations to contribute an effective temperature of  $T_{\text{cross}} = \hbar\omega_p/(2\pi k_B)$ , which for this sample (see Table 4.1) would be about 150 mK, at  $H=0$ . Moreover, since  $\omega_p$  is proportional to  $E_J^{1/2}$ ,  $T_{\text{cross}}$  would decrease as the field is increased. Given that a semiclassical result should not be trusted in the high  $x$  regime appropriate for this sample ( $x \sim 6$ ), a quantitative comparison is inappropriate. However, the qualitative agreement between semiclassical estimates and our observations seem to support the theory that the relatively flat low  $T$  dependence of  $I_c$  and  $R_0$  is due to quantum fluctuations. Even better agreement is given by our very rough theory for  $I_c$  (appropriate for large  $x$ ) based on a charge space model, given at the end of Chapter 6. In this theory,  $T \sim E_J/k_B \sim 150$  mK (at  $H=0$ ) sets the scale for the temperature by which  $I_c$  is to be *substantially* reduced.

#### 4.2.2 Coexistence of Josephson tunneling and Coulomb blockade

If we increase the magnetic field applied to the sample, we observe a very striking new regime. Fig. 4.12 shows a sequence of I-V curves taken on the sample with 140 k $\Omega$  normal resistance, at different values of  $H$ . While at low fields the observed I-V curves are only moderately resistive at  $I < I_c$ , as described in Section 4.1, beyond a critical field  $H_t$  (~

---

\* For the case of  $I_c$ , it has been empirically established by us that as the critical current decreases,  $R_0$  increases roughly proportionally to the square root of the current, keeping the power fed to the sample at  $I = I_c$  approximately constant. At low currents, the I-V curve is linear, so that the measurement of  $R_0$  is independent of the power fed into the sample.

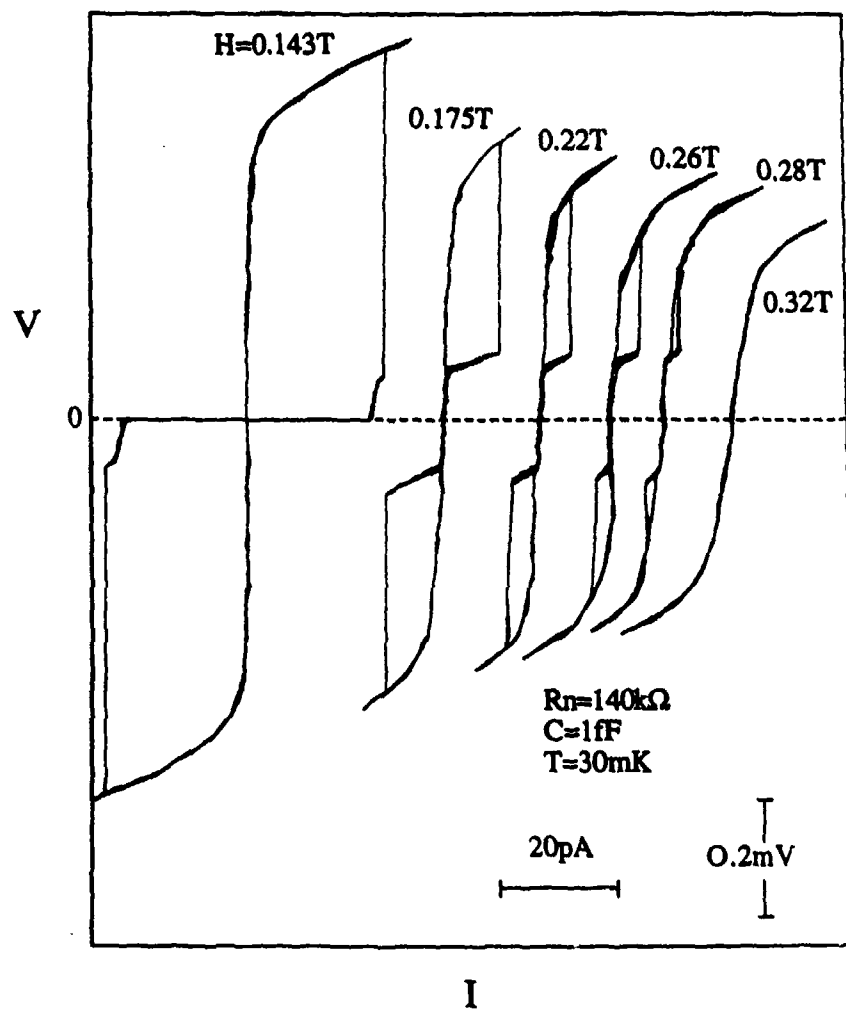


Fig. 4.12: Series of I-V curves taken as a function of magnetic field at fixed temperature, for the sample with  $R_n = 140\text{k}\Omega$ .

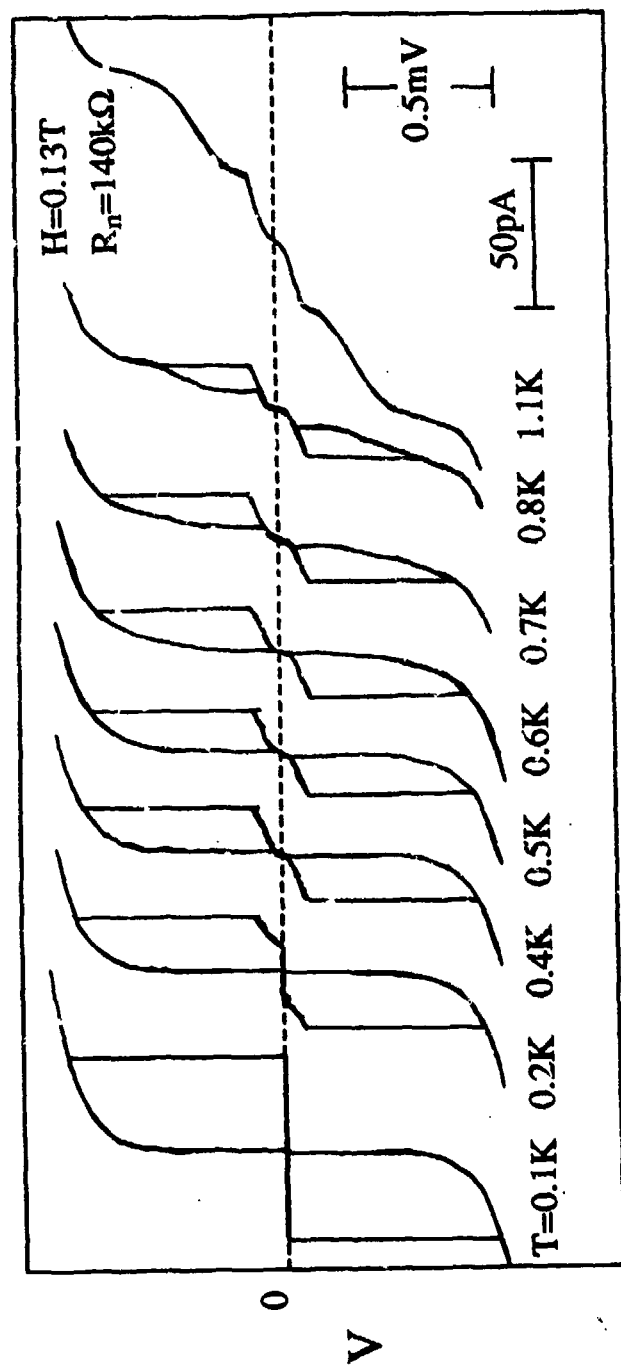


Fig. 4.13: Series of I-V curves taken as a function of temperature at fixed magnetic field, for the sample with  $R_n = 140k\Omega$



0.16 T, in Fig. 4.12) the whole character of the I-V curve changes. The response now becomes *highly* resistive at low currents (with dynamic resistance of order  $R_L$ ), rising to a plateau at  $V \approx V_b$ . Thereafter, the voltage rises on a ramp with slope  $R \sim 10^6 \Omega$ , from which it sharply jumps to the gap voltage  $V_g$  at a current we identify as  $I_c$ . This characteristic behavior is observed until  $H$  is equal to a second threshold field  $H_{t2}$  (about 0.32 T for the sample in Fig. 4.12) beyond which the critical current is reduced to zero, and the "bump" on the I-V curve is no longer visible. Once the novel behavior sets in, between  $H_t$  and  $H_{t2}$ , the value of  $V_b$  is found to be insensitive to magnetic field and temperature. This is shown, for example, in Fig. 4.13: the I-V curves, taken at the intermediate field of 0.13 tesla as a function of temperature, undergo a transition similar to that shown in Fig. 4.11 as a function of field. Apart from rounding, the value of  $V_b$  is the same in all cases.

By reducing the Josephson coupling energy with magnetic field or temperature, we can thus induce a striking transition in the shape of the I-V curve. The new curves are highly resistive at low currents, qualitatively reminiscent of the Coulomb blockade effect mentioned in the introduction. Moreover, as shown in Fig. 4.14, to the precision with which  $C_i$  is known, the measured  $V_b$  corresponds to  $e/2C_i$  in all measured samples, where  $C_i$  is the *intrinsic* capacitance. In this novel regime, features typical of the Coulomb blockade, such as the knee at  $V \approx e/2C$ , coexist with a sharp voltage jump at a current reminiscent of the Josephson critical current  $I_c$ .

Fig. 4.15 shows a plot of the threshold fields  $H_t$  and  $H_{t2}$  vs temperature for a different sample, with  $R_N = 14.8 \text{ k}\Omega$ . As the temperature is increased,  $E_J$  decreases\*, and the value of applied field required to reduce the Josephson energy to the threshold level ( $H_t$ ), also decreases.

---

\* At these fields, the transition temperature of the sample is as low as 1.4 K, so that between 50 mK and 1K the value of  $E_J$  changes considerably.

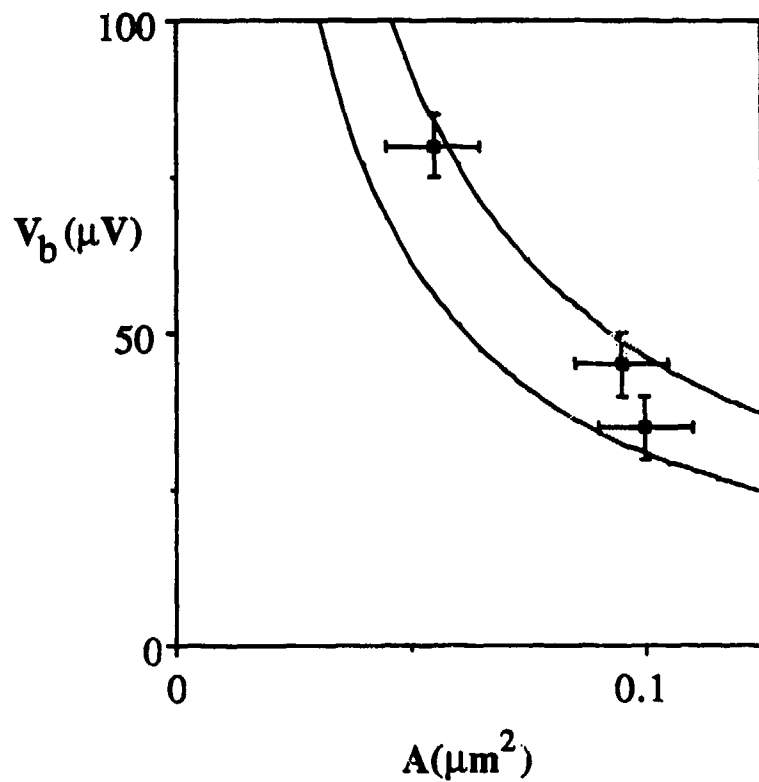


Fig. 4.14: Measured blockade voltage  $V_b$  as a function of junction area. The three measured samples (from left to right) had  $R_1 = 140$ , 35, and 14.8  $\text{k}\Omega$ . The curves correspond to  $e/2C$ , calculated using an oxide barrier thickness of 30 Å (top curve) and 20 Å (bottom curve).

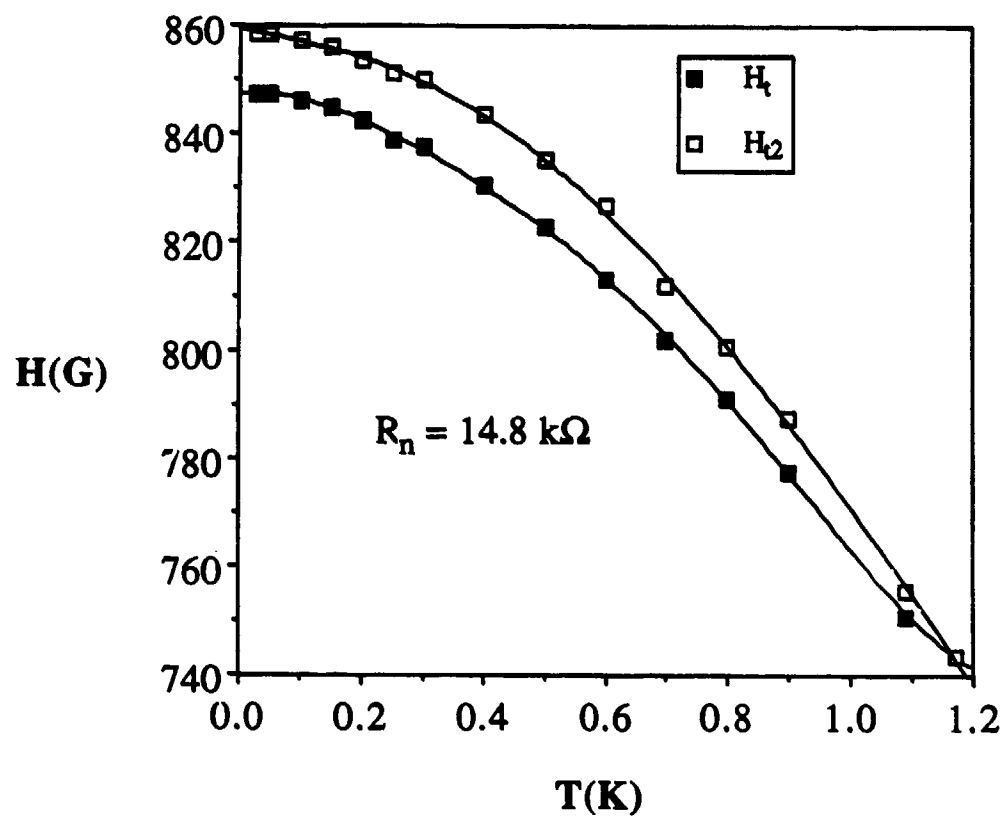


Fig. 4.15: Threshold fields  $H_1$  and  $H_2$  (defined in the text) vs.  $T$ .

#### 4.2.3 Normal - insulator - normal junction regime

If the field is increased beyond the critical field of the tin electrodes, the device becomes a normal - insulator - normal tunnel junction. The effect of charging energy can then be studied without the added complications of superconductivity. We find however, that the high magnetic fields necessary to destroy the superconductivity also appear to affect the I-V curve of the device, adding new complications to the problem.

The field is applied to the junctions in a direction parallel to the plane of the electrodes. In a thin superconducting film, the parallel critical field  $H_{c\parallel}$  is given by

$$H_{c\parallel} = 2\sqrt{6} \frac{H_c \lambda}{d} \quad (4.1)$$

where  $d$  is the film thickness, and  $\lambda$  is the penetration depth at zero field. For a thin film, the parallel critical field can thus be considerably larger than  $H_c$ . For our samples, we found  $H_{c\parallel}$  between 0.3 and 0.7 tesla which, combined with a typical  $d$  of about 700 Å, gives us  $\lambda$  in the neighborhood of 2000 Å, assuming a tin bulk critical field  $H_c = 305$  G.

Fig.4.16 is a plot of the gap voltage  $V_g$  as a function of magnetic field for a sample with  $R_n$  equal to  $8.3 \text{ k}\Omega$ .<sup>§</sup>  $V_g$  is at first strongly dependent on  $H$ , as appropriate for the dependence of the superconducting energy gap, but bottoms out at higher fields to a constant value. We attribute this to the effect of the Coulomb blockade; we interpret the remnant gap on the I-V curve as corresponding to  $e/2C$ , with  $C$  corresponding to  $C_i$  (within 20 - 50%) for all our measured samples. An I-V curve of a device in this regime, showing the remnant gap, was shown in Fig. 1.5.

---

<sup>§</sup> This data was taken by A. T. Johnson.

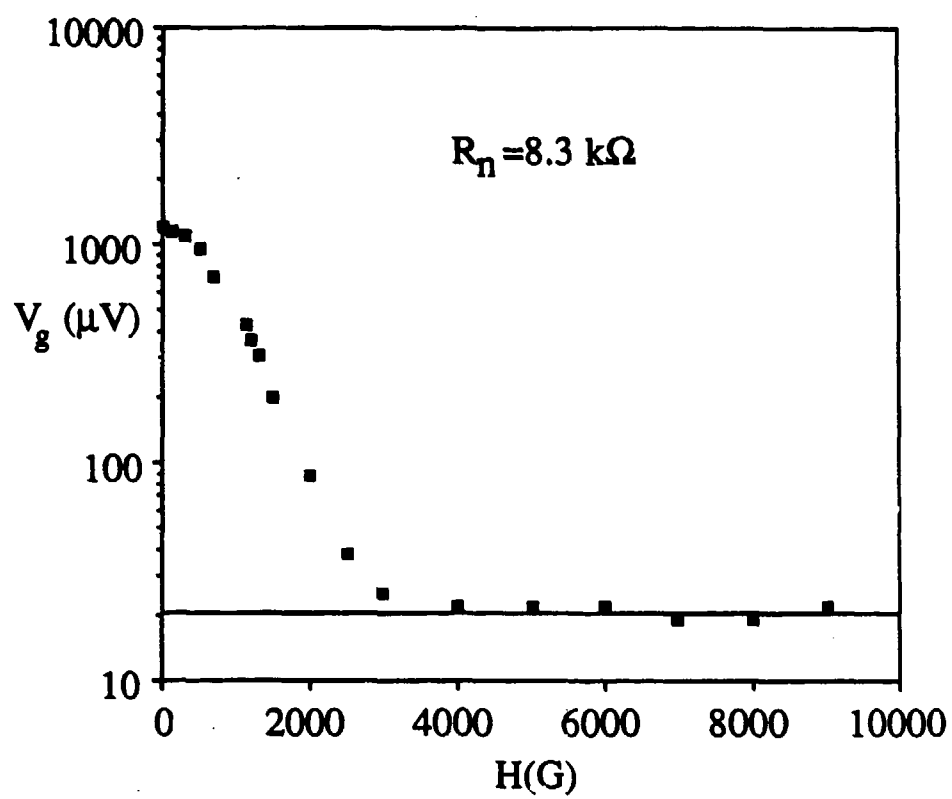


Fig. 4.16: Gap voltage  $V_g$  vs.  $H$ , for the sample with  $R_n = 8.3 \text{ k}\Omega$ .

Even though the magnitude of the remnant gap agrees with that expected from charging effects, the shape of the I-V curve is a bit washed out, when compared to the  $I \propto V^2$  ideal [Averin and Likharev, 1986] Coulomb blockade dependence. Moreover, if the magnetic field is increased further the effect of the Coulomb blockade eventually becomes even less marked, as shown in Fig. 4.17. We believe that the Coulomb blockade is rendered less effective by level broadening by spin alignment energies in the presence of spin-orbit scattering processes.

To find the level broadening, we need to estimate<sup>†</sup> the dephasing time  $\tau_\phi$  due to the spin-orbit scattering process. The dephasing time can be defined as the amount of time elapsed for the phase to change by a significant amount, say  $\pi$ . The energy broadening  $\Delta E$  is then simply  $\sim \hbar \tau_\phi^{-1}$ . The energy difference between the two spin-flipped states is  $2\mu_B H$ . The average time between spin-flip events is the spin-orbit scattering time  $\tau_{so}$ . The amount of phase deviation between spin-flips will then be  $(2\mu_B H / \hbar) \tau_{so}$ . The number of flips made for a length of time equal to the dephasing time is, on the average,  $\tau_\phi / \tau_{so}$ . If we assume that the flip process is random, the total net phase deviation will be given by the phase deviation per flip times the square root of the number of flips. Since in one dephasing time, the net phase deviation accomplished is by definition  $\pi$ , we can write

$$\tau_{so} \left( \frac{2 \mu_B H}{\hbar} \right) \sqrt{\frac{\tau_\phi}{\tau_{so}}} = \pi \quad (4.2)$$

so that we can solve for  $\tau_\phi$  and estimate

$$\Delta E \sim \hbar \tau_\phi^{-1} = \frac{\pi^2}{4} \frac{(\mu_B H)^2}{\hbar} \tau_{so} \quad (4.3)$$

---

<sup>†</sup> M. Tinkham, private communication.

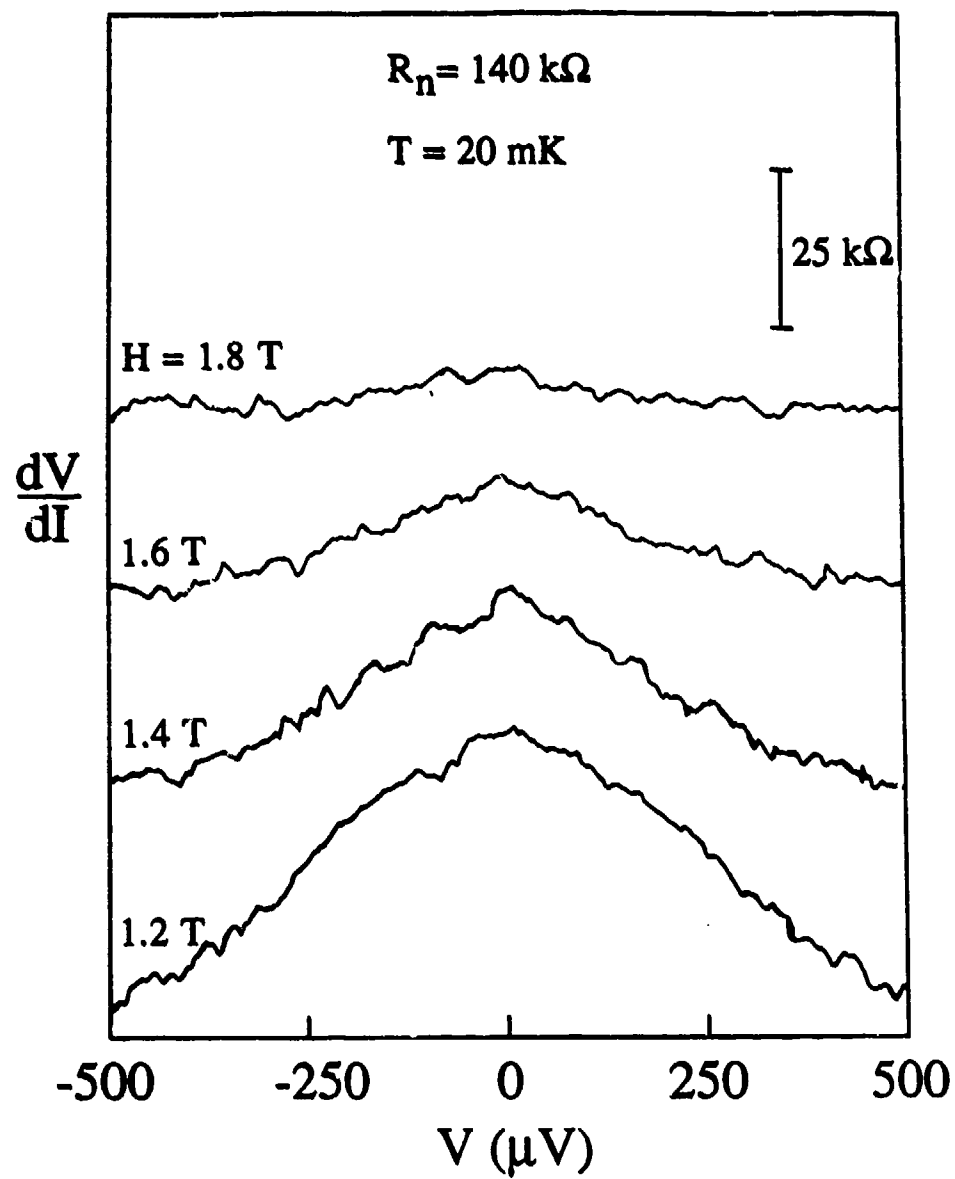


Fig. 4.17:  $dV/dI$  vs.  $V$ , for different magnetic field values, for the sample with  $R_n = 140 \text{ k}\Omega$ .

If this energy width becomes comparable to the charging energy, we would expect the effect of the Coulomb blockade to be washed out. At  $H \sim 2 T$ , the field scale on which the  $dV/dI$  vs.  $V$  peak is flattening out in Fig. 4.17,  $\mu_B H$  is  $1.5 K$ . A typical value of  $\tau_{SO}$  for Sn is  $\sim 10^{-12}$  sec [see Van Haesendonck, 1985]. Therefore, at  $2 T$ ,  $\Delta E \sim 0.8 K$ , which is indeed very close to the charging energy ( $E_c \sim 0.9 K$ ) for the sample with  $R_n = 140 k\Omega$ .

#### 4.3 Measurement of Eleven-Junction Array

As we discuss further in the next chapter, one of our most puzzling observations is that the capacitance of one of our junctions does not seem to be strongly affected by the large parasitic capacitance of the leads. To investigate the effect of the leads on the behavior of our junctions, we fabricated a sample consisting of eleven junctions in series. If the leads strongly affect the dynamics of our devices, then the behavior of the smallest junction (fabricated in the center of the array), should be qualitatively different from the behavior of our single and double junction samples, described above.

A typical low temperature I-V curve of the eleven junction array is shown in Fig. 4.18, taken at  $T = 50 mK$ . The return branch of the I-V curve shows eleven small plateaus, the evidence of eleven gap voltage jumps. On the other branch, all junctions appear to switch simultaneously: apparently the switching of the junction with the smallest  $I_c$  triggers switching in all the other junctions as well. The behavior of the array is similar to that of single and double junction samples: The critical current is considerably reduced below the Ambegaokar Baratoff value  $I_{c0}$  at low temperature, and the I-V curve is resistive at all currents. A lot of effort was spent searching for a region of negative resistance at low currents, which has been predicted by various authors [see, for example, Likharev and Zorin, 1985]. As in the single and double junction samples, no such region was detected.



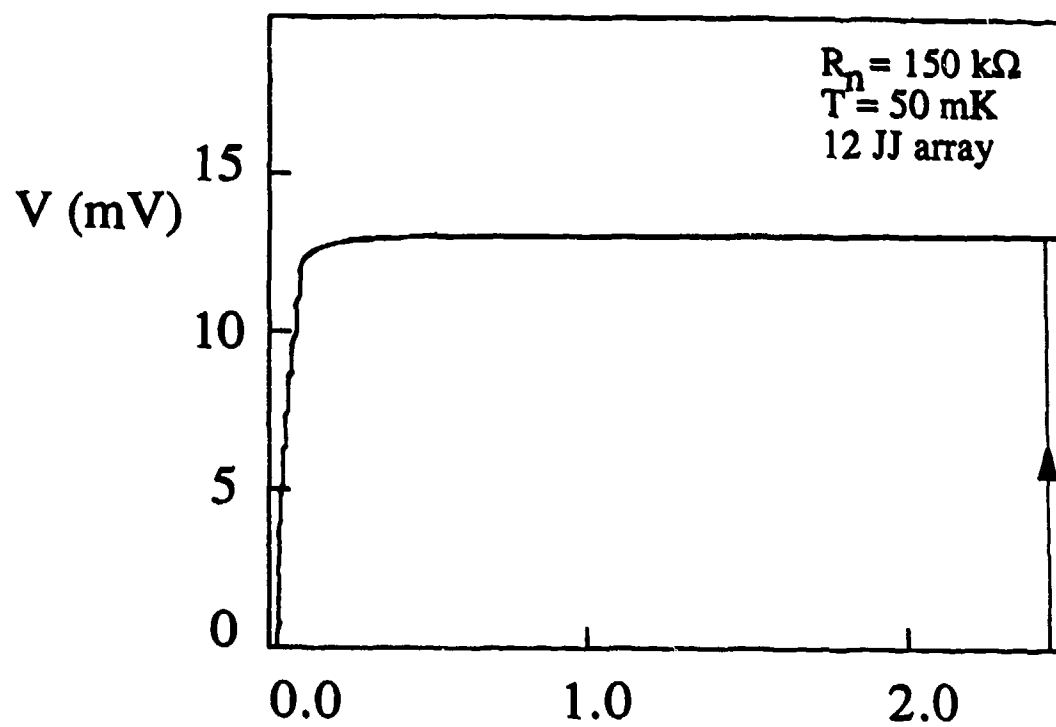


Fig. 4.18: Low temperature I-V characteristic of the eleven-junction array.

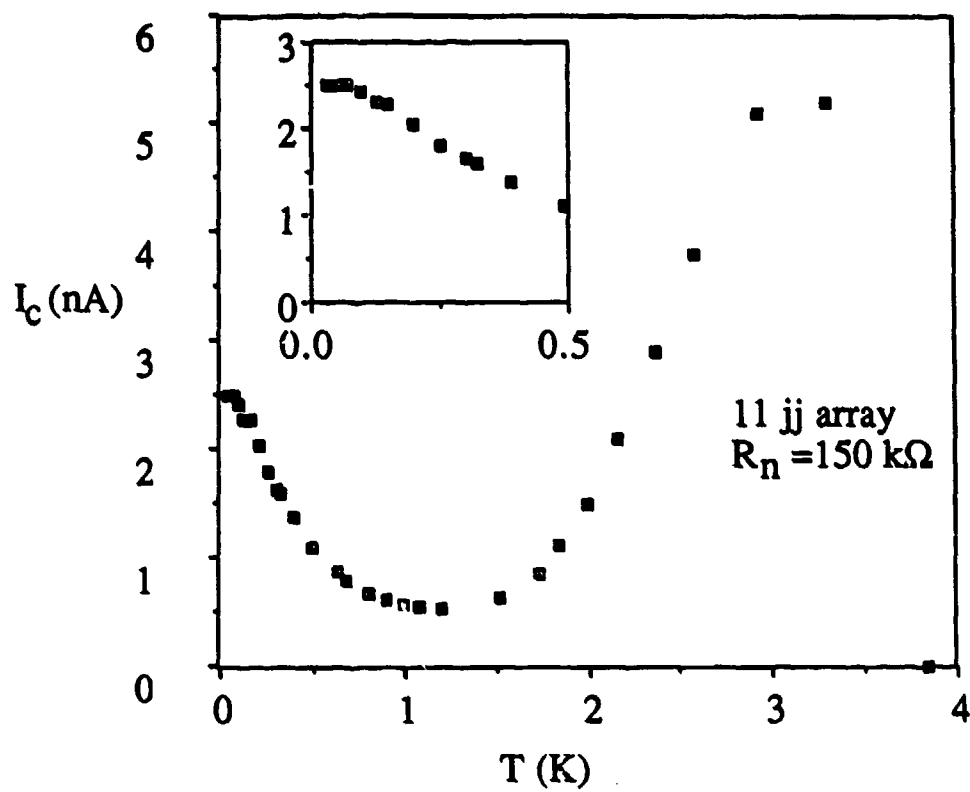


Fig. 4.19:  $I_c$  vs.  $T$  for the eleven-junction array.

Fig. 4.19 is a plot of the critical current of the array vs. temperature, the former defined as the first (smallest) critical current on the I-V curve. We interpret the measured  $I_c$  as arising from the response of the lowest  $I_c$  junction in the array. The qualitative features of Fig. 4.19 are very similar to those typical of a single junction sample, shown in Fig. 4.3. The only qualitative difference is that the flat region at low temperature appears considerably broader, extending as far as  $100\text{ mK}$ .

To investigate the possible reason of this difference we can apply a field to the sample, much in the same fashion as we did in Section 4.2.1. The results are plotted in Fig. 4.20. In this case, the application of a field does not affect the width of the flat region, as is shown especially well in Fig. 4.20(b). Using the same arguments outlined in Section 4.2.1 we believe, in this case, that the flat region is not due to quantum fluctuations, since reducing the Josephson coupling energy by a magnetic field does not affect its width. Moreover, we believe that it is not due to extrinsic noise, since the shielding is the same as in the single junction samples. The heat sinking of the smallest junction in the array, on the other hand, is much worse than in the single junction samples, since its leads include five other highly resistive tunnel junctions.<sup>†</sup> Thus, our interpretation is that this time we are witnessing the effect of heating on the sample.

---

<sup>†</sup> We discussed in Chapter 3 that we believe that the leads appear to be the most effective heat sinking mechanism for the junctions.

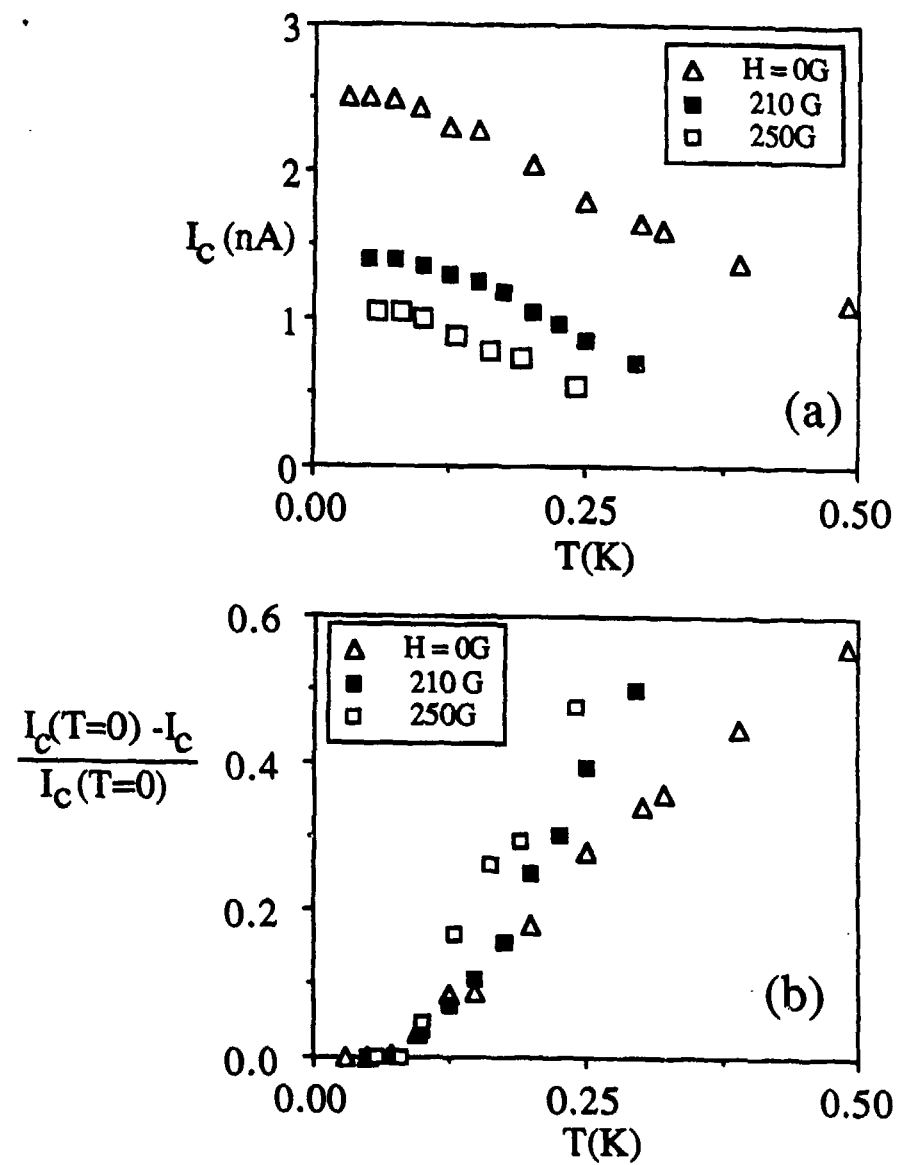


Fig. 4.20: Low temperature  $I_c$  vs.  $T$  for the eleven-junction array, for different magnetic field values. (a) and (b) share the horizontal scale.

#### 4.4 Summary of Experimental Results

In this chapter we have outlined a number of initially puzzling experimental results. For some of the results, a brief interpretation has already been provided. The next two chapters are devoted to the more complete interpretation of the major results. These are:

1. The existence and magnitude of  $R_o(T)$ .
2. The reentrant temperature dependence of  $I_c$  and  $I_r$ .
3. The reduction of  $I_c$  by an order of magnitude relative to  $I_{co}$ , while maintaining a narrow switching distribution.
4. The coexistence, at intermediate fields, of features common to the Coulomb blockade and Josephson tunneling.

In Chapter 5, we attempt to stretch existing classical models to analyze our results. In Chapter 6, we examine the consequences of a more fully quantum-mechanical picture. Whereas the classical approach proves most successful in the higher temperature regimes, the quantum approach is more appropriate at low temperatures.

## **CHAPTER 5**

### **DISCUSSION: THE CLASSICAL REGIME**

In the next two chapters, we describe an interpretation of the salient features of our measurements. We begin in this chapter by discussing in Section 5.1 the basic assumptions underlying our presentation. In Section 5.2, we go on to discuss the failure of the most standard models, which successfully describe conventional high capacitance Josephson devices. We then present the first part of our interpretation in Section 5.3, which is an extension of the basic classical RCSJ model described in Chapter 2. The range of validity of a classical approach is limited for our samples, since the significant charging energy of the devices is expected to cause large quantum fluctuations in the phase, as discussed in Chapter 2. On the other hand, the semiclassical approach provides a very useful heuristic start for our interpretation, and appears to give semi-quantitative agreement above 1 K for our lower resistance samples, in which quantum fluctuations are not expected to be as large. The second part of our interpretation is given in Chapter 6, in which we discuss a quantum mechanical approach, used in explaining our lower temperature results.

#### **5.1. Definition of the Basic Model**

This first section is a discussion of the assumptions we make in our interpretation. It applies equally well to the classical treatment, presented in the remainder of this chapter, and to the quantum treatment of Chapter 6.

Our basic model is the usual resistively and capacitively shunted Josephson junction (RCSJ) model discussed in Chapter 2, and shown schematically in Fig. 5.1. A complete description of the model involves characterizations of the Josephson coupling channel by a

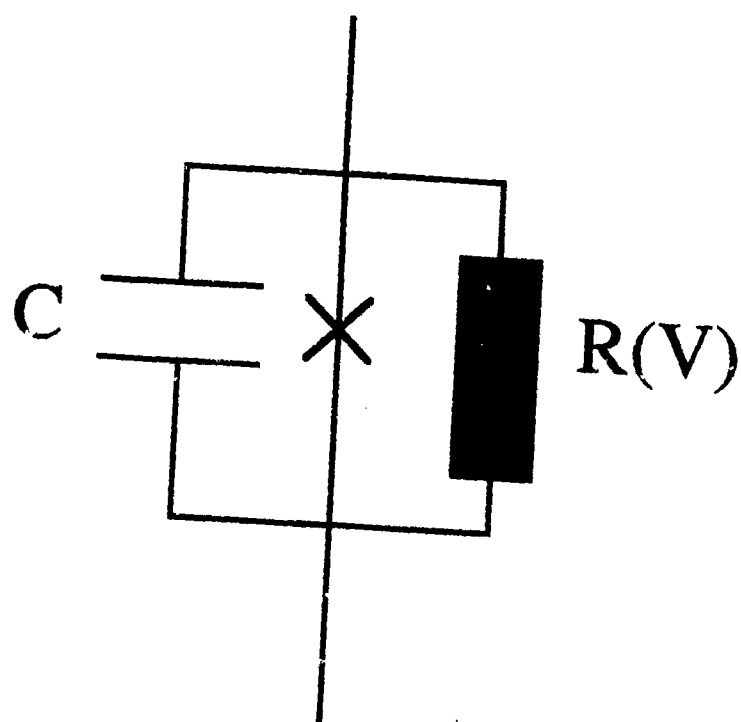


Fig. 5.1: Schematic of the equivalent junction circuit used in the RCSJ model.

definition of  $E_J$ , of the capacitive channel by the definition of  $C$ , and of the dissipative channel by the definition of  $R(V)$ .

We assume that  $E_J$  is given by  $E_J = \hbar I_{co}/2e$ , where  $I_{co}$  is given by the Ambegaokar-Baratoff relation [Ambegaokar and Baratoff, 1962]:

$$I_{co} = \frac{\pi \Delta}{2 e R_n} \tanh\left(\frac{\Delta}{2 k_B T}\right) \quad (5.1)$$

This formula has been found to give excellent agreement with critical current measurements on large low resistance ( $R_n < 5 \Omega$ ) Sn-SnOx-Sr junctions, where thermal and quantum fluctuation effects are expected to be negligible [Danchi, 1982]. These samples were fabricated by our research group with the same equipment and techniques as those used in the fabrication of the small high-resistance samples which are the subject of this study.

We also assume that  $C$  can be approximated by the intrinsic capacitance  $C_i$  and that the relevant resistance  $R(V)$  is given by  $R_L$  for  $|V| < 2\Delta/e$ , and by  $R_n$  otherwise. While it may seem surprising that the extensive distributed capacitance of the leads does not overwhelm the small intrinsic capacitance, there is significant experimental justification for our assumption. For example, van Bentum et al.[1987] and Hartmann et al.[1988] recently performed Coulomb blockade measurements in a scanning tunneling microscope (STM) with normal electrodes: their measured capacitance values in the neighborhood of  $10^{-18} F$  were unaffected by the very large distributed capacitance of the STM apparatus.

To test the effect of lead impedance on the dynamics of our devices, we have fabricated junctions in single-, double-, and eleven-junction configurations. As we discussed in Chapter 4, the behavior of the smallest junction in each of the measured configurations appeared mostly unaffected (except for heating effects) by the presence of companion junctions in the leads, whose capacitance and inductance would grossly affect the lead impedance. Thus it appears that the dynamics of our junctions depend mainly on



their *intrinsic* impedance. While this is in apparent contrast with the observations of Martinis *et al.* [1985] on much larger junctions, we believe that the different behavior may be due to the importance of *single* electron effects in our devices. As the energy change due to the tunneling of a single electron becomes dominant, the problem will become more microscopic in nature, and the timescale fast. The timescale for the dynamics of a conventional semiclassical Josephson junction [of the kind used by Martinis *et al.*, 1985] is given by the Josephson plasma frequency, typically of order  $10^9 - 10^{11}$  Hz. In the opposite regime, when the charging energy is completely dominant [as is the case in the observations of van Benthum, *et al.*, 1987], the characteristic frequency is thought to be the inverse of the electron tunneling time, typically of order  $10^{15}$  Hz. The faster the time scale the higher the impedance of the inductive leads. These arguments do not show that the devices will be *completely* independent of the leads; we believe, however, that the parasitic contributions are small, and that the intrinsic capacitance  $C_i$ , in our system, is a reasonable estimate of the total effective capacitance of the device. This position will be further justified *a posteriori* by comparing the predictions of this model with our data.

Finally, since we believe that the low temperature behavior of our devices is not dominated by dissipation in the leads, it is important to consider the nature of the intrinsic dissipation,  $R(V)$ . Since dissipation in an ideal Josephson device is determined by the tunneling of quasiparticles, the discrete nature of the charge transfer in the tunneling process will become important. We consider this especially in the last sections of Chapter 6, when we analyze the coexistence of the Coulomb blockade with some features of Josephson tunneling. One interesting aspect of our measurements of  $R_L$ , the low voltage part of  $R(V)$ , is that its temperature dependence follows quasiparticle thermal activation at higher temperatures, but flattens off at low- $T$ , as described by (4.1). We believe that the existence of a finite  $R_L$  as  $T \rightarrow 0$  is not due to metallic whiskers partially shorting out the barrier, since  $R_L(0)$  is very large, typically of order  $10^8 \Omega$ ; since the whisker's length would be equal to the barrier thickness ( $\sim 25 \text{ \AA}$ ), a resistance of  $10^8 \Omega$  would require a

resistivity much larger than  $1 \Omega\text{-cm}$ , even for a diameter as small as one atomic spacing. This appears unlikely, and we believe that this temperature independent dissipation term may instead be due to a tunneling mechanism.

The apparent proportionality of the residual leakage resistance to  $R_n^2$  (see Fig. 4.8), suggests that a possible source of low T dissipation may reside in the effect of Andreev reflections on the tunneling I-V response. This was analyzed by Blonder, Tinkham, and Klapwijk [BTK, 1982], who showed that the Andreev channel should have a probability going as the square of the probability of charge transfer in the normal channel. If we extrapolate the square law relationship back, we find that  $R_n \sim R_L(0)$  for a resistance of order  $100 \Omega$ . In the BTK theory, the point at which the normal and leakage resistance are approximately equal corresponds to a device of "barrier strength"  $Z$  [see BTK, 1982] of order one: i.e. a device whose barrier is very weak, and whose I-V characteristic begins to resemble a microbridge rather than a tunnel junction. A resistance of  $100 \Omega$  appears high for a device with microbridge characteristics. However, this apparent inconsistency can be resolved if we remember that there is evidence (from the magnetic field data, for example) that the oxide barrier may be quite nonuniform. Since the Andreev term is proportional to the *square* of the tunneling probability, a small fraction of the junction with a thinner barrier may dominate in the leakage term.

## 5.2 Failure of Standard Approaches

As we described in Sections 2.6.2 and 2.6.3, if  $kT$  or  $E_c$  are significant in comparison with  $E_J$ ,  $I_c(T)$  is no longer expected to closely follow  $I_{c0}(T)$ . It is now well established, both experimentally and theoretically,<sup>†</sup> that thermally activated "escape" from

---

<sup>†</sup> See, for example, Fulton and Dunkelberger [1974], Naor, Tesche, and Ketchen [1982], Danchi *et al.* [1984], Silvestrini *et al.*, [1988], and Silvestrini, Liengme, and Gray [1988], for experimental treatments,

the minimum of the tilted cosine potential causes "premature switching" to the finite voltage regime. An expression for the thermal escape rate was given by (2.57). For an order of magnitude estimate, ignoring the effect of damping on the prefactor and the current dependence of the attempt frequency, we can write

$$\tau^{-1} \sim \frac{\omega_p}{2\pi} e^{-\frac{\Delta U}{k_B T}} \quad (5.2)$$

The plasma frequency is given by  $\omega_p = (8E_c E_J)^{1/2} / \hbar$ , and is typically of order  $10^{10}$  Hz. As a result, in experiments with current sweep times of order 1 second, escape will occur as soon as  $\Delta U(I)/kT \approx \ln v_p \approx 20 \gg 1$ . Taking account of the fact that  $\Delta U(I) \approx 2E_J(1 - I/I_{co})^{3/2}$  to a good approximation, one expects switching to occur when this  $\Delta U(I) \sim 20 kT$ . A better approximation for the average  $I_c$  expected from this model was given in (2.58), and depended logarithmically on the current sweep rate.

Since the escape is stochastic, there will be a distribution of switching currents, whose width was given in Chapter 2 to be:

$$\delta I_c = \frac{\frac{2}{3}(I_{co} - I_c)}{\ln\left(\frac{\omega_p \delta I_c}{\frac{dI}{dt}}\right)} \quad (5.3)$$

In our samples,  $I_c \sim 0.1 I_{co}$ , and the logarithm is of order 20, so that (5.3) would give  $\delta I_c \approx 0.03 I_{co}$ . This result is inconsistent by an order of magnitude with the new data, in which  $\delta I_c \approx 0.003 I_{co}$ . The switching distribution is simply too narrow to be compatible with an

---

and Kramers [1940], Ambegaokar and Halperin [1969], P.A. Lee [1971], J. Kurkijärvi [1972], Büttiker, Harris and Landauer [1983], and Barone, Cristiano, and Silvestrini [1985], for theoretical treatments.

explanation of the depression of the observed  $I_c$  so far below  $I_{c0}$  by premature switching. Put another way, for  $I$  so far below  $I_{c0}$ , the cosine potential is barely tilted, and the height of the barrier is almost independent of current. Hence a small change in current could hardly account for a sudden onset of switching out of the zero-voltage state. Moreover, this picture of stochastic escape is qualitatively incompatible with the finite voltage below  $I_c$ , which implies a steady-state phase evolution, rather than metastable locking in position in a single well until the escape.

As one goes down in temperature, eventually this thermally activated escape becomes less likely than escape by macroscopic quantum tunneling (MQT) through the barrier. This mechanism already takes us beyond the classical regime, but in the junctions studied previously,\* this escape probability was sufficiently low that one could still treat the phase as a rather localized semiclassical quantity, which occasionally made a probabilistic transition through the barrier into a free-running finite voltage state. In this regime, it was shown that there is a crossover temperature given roughly by

$$k_B T_{\text{cross}} = \hbar \omega_p / 2\pi = (8E_c E_J)^{1/2} / 2\pi \quad (5.4)$$

as we discussed in Chapter 2. Below this temperature, the same qualitative probabilistic switching should occur as in the thermally activated regime, except that the constant  $T_{\text{cross}}$  replaces the actual temperature. Thus, the same inconsistency between a narrow switching distribution and a huge depression of  $I_c$  below  $I_{c0}$  exists in this regime as in the thermally activated one, and a more appropriate explanation must be found.

---

\* See den Boer and de Bruyn Ouboter [1980], Prance *et al.* [1981], Voss and Webb [1981], Jackel *et al.* [1981], Washburn *et al.* [1985], Schwartz *et al.* [1985], Martinis, Devoret, and Clarke [1985], Devoret, Martinis, and Clarke [1985].

### 5.3 Extension of Standard Models

In the previous section, we have argued that the usual dynamics describing Josephson junction behavior do not apply to our observations. The common situation of a constant  $\phi$  value at  $I < I_c$  followed by a probabilistic switching into the finite voltage "running" state is simply inconsistent with our measurements. Since the observed I-V curves are resistive, even at the lowest currents, it seems very plausible that the dynamics of the system are characterized by very frequent phase-slips, which would give rise to dissipation, and thus to  $R_0$ . Mechanisms of these frequent phase slips would be thermal activation (since for our devices typical heights of the Josephson potential are of order  $IK$ ), and quantum tunneling (since  $E_c$  is of order  $E_J$ ). However, since a current bias tilts the Josephson potential, the system would possibly exhibit no critical current at all, since once the first phase-slip occurs, the subsequent ones become easier. To account for the observations, therefore, we need to consider the effect of damping, as a retrapping mechanism.

Qualitatively, the dynamics of our devices may be described as follows: At  $I < I_c$ , the phase frequently escapes from its potential well. The energy it acquires in a  $2\pi$  phase-slip, however, is lost through damping, and the phase retraps in a subsequent well. This process goes on until  $I = I_c$ , at which point one of two things happens. Either the potential tilt becomes enough for the system to acquire more energy than it loses from damping, or some intrinsic limit to the maximum Josephson current is exceeded. We believe the first situation to be valid at higher temperatures, in what we call the "semiclassical regime", and the second situation to be valid at low temperatures, in what we call the "quantum regime".

### 5.3.1 The Role of Damping in the Semiclassical Case

It is well known that so long as a junction is underdamped, the amount of damping affects the escape rate only through a change in the prefactor in (5.2). Since this factor only enters logarithmically in the depression of  $I_c$ , this change is usually unimportant. However, the amount of damping is the *crucial* factor in determining the retrapping current  $I_r$ . Because  $I_c$  and  $I_r$  coincide above  $\sim 2/3 T_c$  in the new data, where they are both strongly reentrant, it is appropriate to review the physics of what is going on with  $I_r$  as well as  $I_c$ .

In Chapter 2, we discussed that in the simple RCSJ model, the retrapping current is given by the following expression, if we ignore thermal fluctuations:

$$I_r = \frac{4}{\pi} \frac{I_{co}}{\sqrt{\beta_c}} \frac{1}{R(T)} \sqrt{\frac{I_{co}(T)}{C}} \quad (5.5)$$

Here the temperature dependence of  $I_{co}$  is given by (5.1), which monotonically increases as  $T$  is decreased. Accordingly, if (5.5) is to describe the temperature dependence of  $I_r$  in this reentrant regime below  $\sim 0.9 T_c$ , it must result from the temperature dependence of  $R(T)$ . In fact, if we substitute the leakage resistance approximated by (4.8), an approach justified in Section 2.6.1, we find excellent agreement with the *shape* of the temperature dependence, as shown in Fig. 5.2. [The magnitude is too small by a factor  $\sim 7$ , but we shall see that that discrepancy can be accounted for largely by fluctuation effects which are not included in the Stewart-McCumber analysis which gives rise to (5.5).]

### 5.3.2 The Effect of Thermal Fluctuations on the Critical Currents

It is well known, as noted above, that thermal fluctuations have the effect of reducing the measured  $I_c$  by inducing premature switching out of the zero-voltage state. It is less well known that thermal fluctuations have the opposite effect on  $I_r$ , i.e., they *increase* it. This point has been made by various authors, recently by Cristiano and

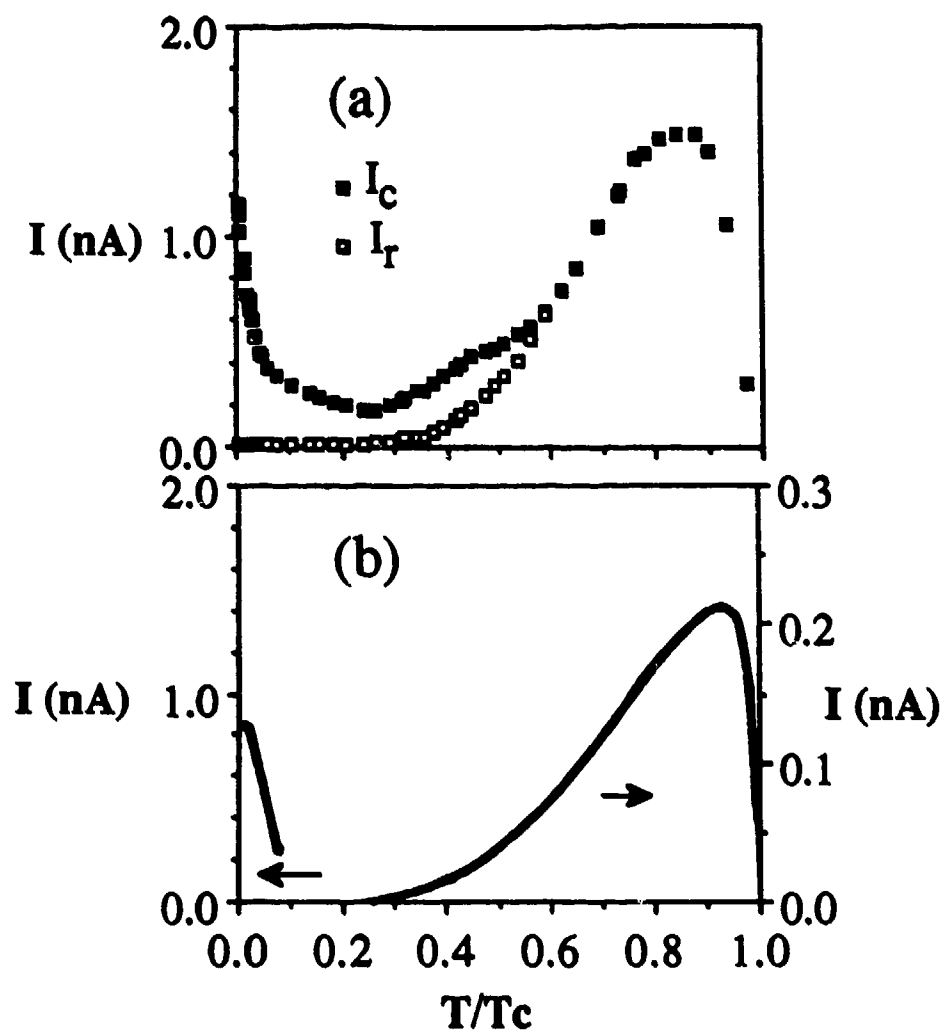


Fig. 5.2: (a)  $I_c$  and  $I_r$  vs.  $T$  for the sample with  $R_n = 70 \text{ k}\Omega$ . (b) Left: predicted low temperature  $I_c$ , due to Zener tunneling and thermal activation, as described in Chapter 6. Right: predicted  $I_r(T)$ , described in the text.

Silvestrini [CS, 1986; 1987] who also presented the results of numerical calculations. Since this result seems counter-intuitive to many, it is worthwhile to give a simple physical argument \* which establishes the correctness of the sign of the effect.

Consider Fig. 5.3 (a), which depicts the tilted washboard potential at the current corresponding to  $I_r$  in the absence of fluctuations. On the vertical axis, we plot the total energy, kinetic plus potential, so that without dissipation the representative point follows a horizontal trajectory. At this current value, the representative point, starting at the top of one barrier follows a trajectory which reaches the corresponding point at the next maximum. Now consider the effect of fluctuations which raise or lower the energy discontinuously at some point on this trajectory. If the initial fluctuation is downward, the trajectory continues downward because energy is dissipated at the rate  $-V^2/R$  and is not recovered from the current drive since the trajectory is confined to a single minimum. On the other hand, if the initial fluctuation is upward in energy, this increases  $1/2 CV^2$  and hence  $V^2/R$ , so that the trajectory falls more steeply, eventually returning to the marginal trajectory on which it started, which it follows stably until the next fluctuation occurs. Since upward fluctuations recover while downward ones cause retrapping, it is clear that the fluctuations tend to make the system *more* stable against runaway. Accordingly, the marginal current value (tilt) giving retrapping is *greater* in the presence of fluctuations than without them, so  $I_r$  is *increased*.

As shown schematically in Fig. 5.3 (b), then, the effect of fluctuations is to induce a convergence of  $I_r$  and  $I_c$  toward a common intermediate value, eliminating hysteresis. Another effect of the fluctuations is to cause both  $I_r$  and  $I_c$  to acquire a probabilistic switching character, as has been mentioned earlier. As the fluctuations increase further in strength beyond that causing the coalescence of  $I_c$  and  $I_r$ , the switching back and forth in the vicinity of this critical current value becomes so rapid compared to experimental time

---

\* M. Tinkham, private communication.



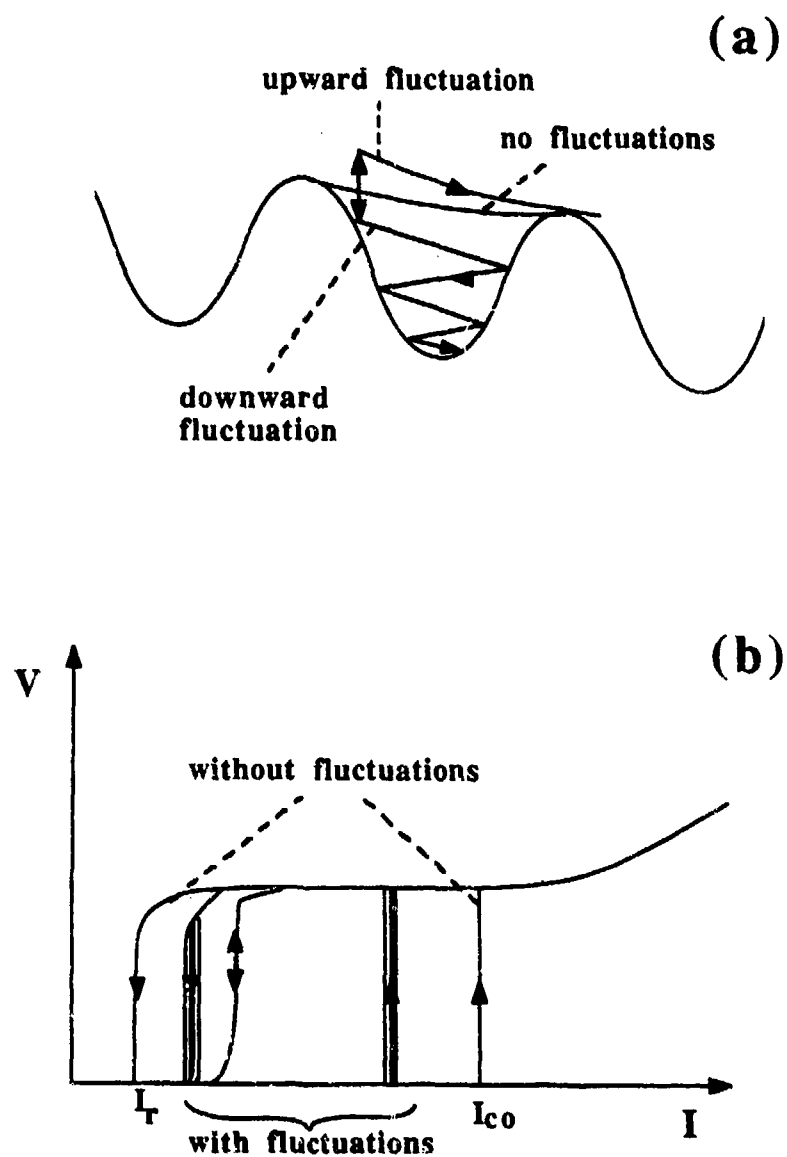


Fig. 5.3: (a) Schematic of the effect of fluctuations on the retrapping process. (b) Sketch of the effect of thermal fluctuations in reducing and eventually eliminating the hysteresis in an underdamped Josephson junction.

scales that the measured voltage averages to give a smooth continuous resistive transition. The value of this coalesced  $I_c = I_r$  can be determined by simulation methods, but one can also reason that it will be determined by the physics of  $I_r$  rather than the physics of  $I_c$ , since when fluctuations are this prominent, the system is activated out of its metastable minima so quickly that "premature" switching is taking place continuously. The crucial question is at what current the damping assisted by fluctuations leads to the retrapped state being the more dynamically stable one, and this is the consideration determining  $I_r$ . We conclude that, in the non-hysteretic regime where fluctuations are dominant, *the measured critical current  $I_c$  should be interpreted as  $I_r$*  as enhanced above the value given by (5.5) by the presence of fluctuations. This theoretical conclusion is confirmed by the experimental observation (see Fig. 5.2) that the temperature dependence trend set by the coalesced  $I_r = I_c$  in the non-hysteretic region continues as that of  $I_r$  when the junction becomes hysteretic.

With the principle established that  $I_r$  (including the major enhancement by fluctuations) determines not only  $I_r$  at all temperatures but also  $I_c$  above the temperature at which hysteresis disappears, we now must estimate how large is the enhancement of (5.5) by fluctuations. The results of CS are restricted to values of  $\gamma = 2E_J/kT = 5 - 50$ , and attempt numbers  $L \sim 10^3 - 10^5$ , whereas in our samples  $\gamma$  is typically less than 1 and the attempt numbers are of order  $10^{10}$ . Still, we can use their results by noting that they show that the enhancement of  $I_r$  varies approximately linearly with the logarithms of  $L$  and  $\gamma$ . Using this observation, if one extrapolates their results to  $\gamma \leq 1$  and  $L \sim 10^{10}$ , one estimates an enhancement factor of roughly 5 or greater; for comparison, the largest enhancement for the parameters considered by CS is about 3, so this extrapolation is not terribly extensive. It is reassuring, nonetheless, that our direct simulations also give enhancements by similar factors. Since it appears that the enhancement factor should not depend strongly on  $\gamma$  so long as it is less than or of order unity, nor on  $L$  so long as it is within an order of magnitude of  $10^{10}$ , we conclude that the temperature dependence of the observed  $I_r$  should be very similar to that of the unfluctuated result (5.5), but that the magnitude should be

larger by a factor of order 5 because of the fluctuations. Considering the uncertainties in parameter values (especially  $C$ ) and in this extrapolation, this estimate is quite consistent with the observation that the measured  $I_r$  is roughly 6-7 times the value given by (5.5), and has essentially the same temperature dependence.

### 5.3.3 Classical estimates of $R_0$

Another interesting feature of our observations is the presence of a resistive state at currents below the measured  $I_c$ . At higher temperatures, the I-V curve is not hysteretic, and the presence of a dissipative branch is not surprising. We have seen that damping appears to play a key role in the determination of the critical current in this regime. We believe that the observation of a nonzero  $R_0$  is also primarily due to damping.

For almost all our junctions, at temperatures above 1 K, thermal fluctuations are very large compared to the Josephson coupling energy. The escape out of the Josephson potential well is thus very rapid, with rates of the order of the Josephson plasma frequency  $\omega_p$ . The "phase point" is thus constantly out of the Josephson potential well, and gradually slips downhill. At currents less than the retrapping current  $I_r$ , however, the escape of the phase point over many wells is not energetically favorable: it loses energy through dissipation faster than it gains energy from the motion downhill. The phase point will thus retrap in a subsequent well.

It would be desirable to compare the observed values of  $R_0$  with estimates extracted from theoretical calculations of the rates of escape out of the Josephson potential. Unfortunately standard theoretical estimates for the escape rate out of a metastable potential break down when  $k_B T$  becomes greater than the barrier height. Moreover, we cannot interpret our low temperature data in this fashion, since below 1 K we expect quantum tunneling to be very important. Our comparison with accepted thermally activated escape theories is thus limited; we can only expect quantitative agreement from our lowest resistance sample ( $R_n=550\Omega$ ,  $E_J=45K$ ), for which the Josephson coupling energy is

reasonably large compared to  $k_B T$  even at relatively high temperatures. For this sample, at temperatures above 2K, the contribution of quantum tunneling should be minor, but the ratio of  $E_J$  to  $k_B T$  is still large.

As we point out above, the existence of substantial resistive voltage even for  $I \ll I_c$  indicates that the phase variable is steadily evolving in time, at an average rate  $d\phi/dt = 2eV/\hbar$ . In the presence of a current, the successive minima drop in energy by  $\hbar I/2e$ , and the barrier heights for escape in the uphill and downhill directions are shifted by  $\pm \hbar I/4e$  with respect to the zero-current case. As a result the escape probability is greater in the downhill direction than in the uphill one, and there is a *net* rate of downhill tunneling proportional to  $I$  (for small  $I$ ). Hence there is a voltage  $V \propto d\phi/dt \propto I$ , which can be described by the resistance  $R_o = V/I$ . We assume that the system will lose energy by dissipation and retrap in the adjacent well, making the phase slip per activation event approximately equal to  $2\pi$  at low current.

We now need to calculate the difference between uphill and downhill escape rates. We define  $\Gamma^+$  to be the escape rate to the right (downhill) and  $\Gamma^-$  to be the value of the escape rate to the left. Expanding around  $I=0$  the following estimate is obtained.

$$R_o = \frac{\hbar}{2e} \frac{1}{I} \frac{d\phi}{dt} \approx \frac{\hbar}{2e} \frac{1}{I} (2\pi) (\Gamma^+ - \Gamma^-) \quad (5.6)$$

To estimate the escape rates we assume that  $\Gamma^+$  and  $\Gamma^-$  are independent: i.e. we assume that  $\Gamma^+$  is only dependent on the barrier height to the right, and not affected by the fact that escape to the left is also possible.  $\Gamma^+$  and  $\Gamma^-$  can then be estimated by using results from thermally activated escape theories. They are functions of the uphill and downhill barrier heights, respectively, and the resistance and capacitance of the device. For the parameters of our lowest resistance junction ( $R_n = 550 \Omega$ ), the differences in the estimates for the Kramers [1940], Büttiker, Harris and Landauer [1983], and Barone, Cristiano, and

Silvestrini[1985] theories are small. We use the last approach for our actual estimates since it is valid closer to the breakdown at  $E_J \sim k_B T$ . The escape rate is thus given by [Barone, Cristiano, and Silvestrini, 1985]

$$\Gamma = \frac{1}{RC} \sum_{n=1}^{\infty} \frac{1}{n!} \frac{1}{n} \left[ \left( \frac{\gamma U_o}{2} \right)^n - \left( \frac{\gamma E_o}{2} \right)^n \right] \quad (5.7)$$

where  $U_o$  is the barrier height (in the uphill or downhill direction) and  $E_o$  is the initial energy of the representative phase point, both normalized to  $E_J$ , while  $\gamma = 2E_J/k_B T$ .  $E_o$  is not a well known parameter for the system: however, it is reasonable [Barone, Cristiano, and Silvestrini, 1985], in the large  $\gamma$  limit, to assume that  $E_o \sim 2/\gamma$ , which corresponds to the particle having initial energy equal to  $k_B T$ . For large  $\gamma$ , therefore,  $E_o$  is small, and (5.7) is easily applied.

Using (5.6) and (5.7), we can now estimate the low current resistance  $R_o$  for our lowest resistance (largest  $\gamma$ ) sample. The agreement is excellent, as shown in the Arrhenius plot of Fig. 5.4, using the estimated *intrinsic* capacitance  $C_i$ , the leakage resistance given by (4.8), and no adjustable parameters. We can use the same approach to estimate  $R_o$  for intermediate resistance samples (having lower  $\gamma$ ). However, (5.7) becomes much more sensitive to  $E_o$ , and the approach only works as an order of magnitude estimate.

For our higher resistance samples, standard models of thermally activated escape no longer apply. For the sample with  $R_n = 140 k\Omega$ , for example, the Josephson coupling energy  $E_J$  only corresponds to  $0.3K$ . Except at the lowest temperatures, the representative phase point is constantly thermally activated out of the potential well. The motion of the phase point, therefore, might resemble more a diffusive random walk, than a sequence of well-defined activated jumps from well to well. Unfortunately, to our knowledge, this regime has not yet received extensive theoretical scrutiny, in the underdamped case. To obtain a simple phenomenological prediction, we assume that the rate of motion downhill is

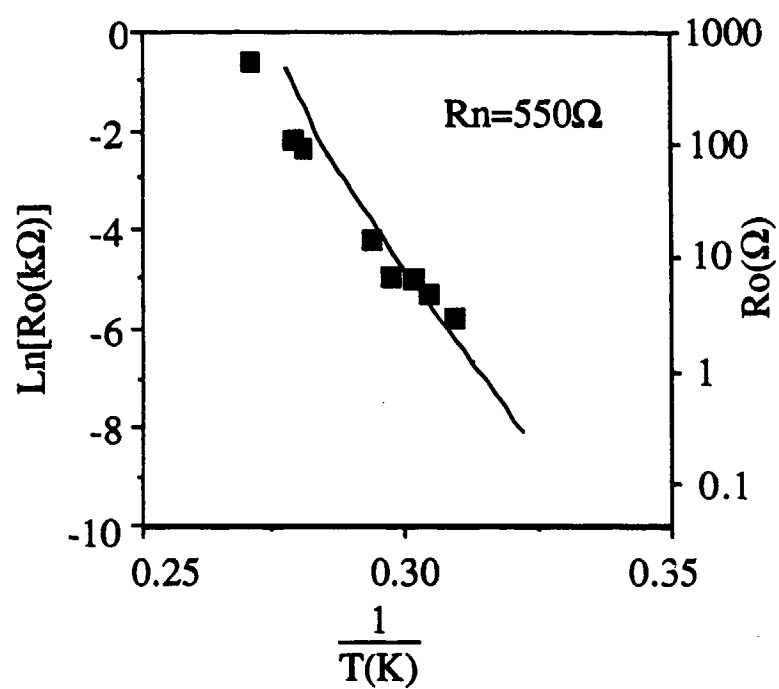


Fig. 5.4:  $R_0$  vs.  $T^{-1}$  for the sample with  $R_n = 550 \Omega$ . The line is a theoretical fit with no adjustable parameters using theory outlined in the text.

proportional to the amount of time the system spends above the barrier. The proportionality constant must reduce to  $R_n$  as  $T \rightarrow T_c$ . We write

$$R_o \approx R_{qtm} + (R_n - R_{qtm}) e^{-\Delta U / kT} \quad (5.8)$$

where  $R_{qtm}$  is the contribution of quantum tunneling, estimated below in section VIII. The activation energy  $\Delta U$ , given by the barrier height  $\sim 2E_J$  in a classical treatment, might be reduced in a more complete quantum treatment, since part of the Josephson potential well is below the lowest quantum state. This rough phenomenological estimate (5.8) is good enough to give an order of magnitude estimate, and an idea of the general trend of the data, as shown in Fig. 5.5, where  $R_{qtm}$  was chosen to fit the limit as  $T \rightarrow 0$ . A more complete treatment will be required to obtain quantitative agreement.

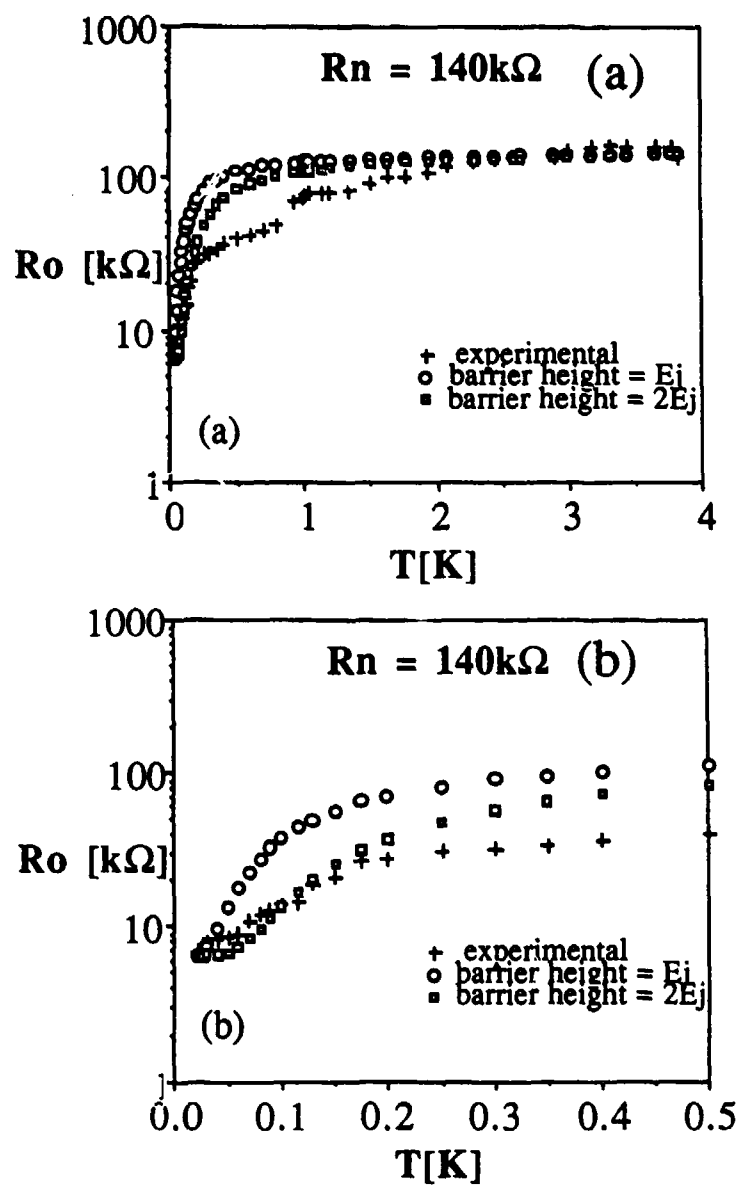


Fig. 5.5: Comparison of experimental and model dependences of  $R_o$  vs.  $T$  for the sample with  $R_n = 140 \text{ kΩ}$ . The horizontal scale is expanded in (b).



#### 5.4 Summary and First Conclusions

From the above, we conclude that the semiclassical model can account for the entire  $I_T(T)$  and for the  $I_C(T)$  (and  $R_0$ , qualitatively) in the non-hysteretic temperature range, provided:

- (a) the effective capacitance in the RCSJ model has a value  $\sim 1\text{-}2\text{ fF}$ , as estimated from the geometry with little allowance for capacitance contributed by the leads.
- (b) The temperature-dependent damping is governed (at least in the frequency range relevant to  $I_T$ ) by the leakage resistance (4.8), which agrees with the measured value of  $R_L$ ;
- (c) Thermal fluctuation effects enhance the  $I_T$  given by (5.5) by a factor of order 5, as expected from simulations.

However, the semiclassical model can *not* account for the low temperature data, where  $I_C > I_T$ , with a measurable resistive voltage at all current levels, including  $I < I_C$ . The possibility that quantum effects provide the explanation is suggested by the fact that for  $C \sim 1\text{ fF}$ , as found above, the Coulomb charging energy  $E_C = e^2/2C \sim 1\text{ K}$ , which is comparable with  $E_J$ . In the next chapter, we will explore this possibility.

## CHAPTER 6

## DISCUSSION: THE QUANTUM REGIME

In the preceding chapter we have given a phenomenological classical treatment of the behavior of a Josephson junction when  $E_J$  is of order  $k_B T$ . In our devices, however, the estimated charging energy is also of order the Josephson coupling energy, which should cause very large quantum phase uncertainties, as discussed in Chapter 2. As the ratio of charging to Josephson energy becomes of order one, the width of the ground state wavefunction in  $\phi$  space approaches the width of the Josephson potential well, and the tunneling rate from well to well becomes very rapid, of order the plasma frequency  $\omega_p$ , where  $\hbar\omega_p = (8E_C E_J)^{1/2}$ . Therefore, to understand our measurements, especially as thermal fluctuations freeze out for  $T < 1K$ , it is necessary to extend our treatment to include the quantum mechanical nature of the phase.

We begin this chapter by using a model in  $\phi$ -space to obtain some estimates for  $R_0$  and  $I_c$  in Sections 6.1 and 6.2. Sections 6.3 and 6.4 analyze the consequences of a simple  $Q$ -space treatment which should be more appropriate in the large  $E_C/E_J$  limit.

6.1 Interpretation of the Resistance  $R_0$ 

Our treatment of this problem in the quantum regime is quite similar to that given in Chapter 5, for the classical case. For the lower voltage branch of the I-V curve, at  $I < I_c$ , the expectation value of the phase tunnels from well to well, evolving in time at a rate  $d\phi/dt = 2eV/\hbar$ . To develop an interpretation of this voltage in the  $\phi$ -space framework, we assume that the degree of delocalization is sufficiently small that we can reasonably represent  $\psi(\phi, t)$  by a function localized in one well, which occasionally tunnels into an *adjacent* well. (For the present, we assume  $T = 0$ , so there are no thermally activated hops.) In the presence of a current, the tunneling probability is greater in the downhill direction than in the uphill

one, and there is a *net* rate of downhill tunneling proportional to  $I$  (for small  $I$ ). Hence there is a voltage  $V \propto d\phi/dt \propto I$ , which can be described by the resistance  $R_0 = V/I$ . While perhaps *qualitatively* appropriate for all samples, this picture can only be expected to be *quantitatively* correct for the samples with  $x < 1$  ( $x = E_C/E_J$ ), so that the phase uncertainty is still not large compared to  $2\pi$ . The sample with  $R_n = 14.8 \text{ k}\Omega$ , and  $x \sim 0.25$  thus appears to be a good example for testing the accuracy of this model.

We implicitly assume that there is sufficient damping present that, after each tunneling event, the system equilibrates into the lowest quantum state in the well into which it has just tunneled, before tunneling again. If the system did *not* lose energy in this way, it would run away, since in successive wells (in the downhill direction) it would experience lower and lower barriers, and tunnel ever more readily, until it was above the barrier entirely. Of course damping also reduces the tunneling rate, as we discussed in Chapter 2, but a calculation of the tunneling rate in the absence of damping provides a useful starting point, giving an upper bound on the resistance  $R_0$ . We also ignore any effect of phase coherent reflections from subsequent wells of the Josephson potential. This is expected to be a significant source of error, especially for values of  $x > 1$ , in which case  $\psi(\phi)$  is expected to be significantly spread out over more than one potential well.

We assume that  $\Gamma^+$ , the tunneling rate to the right (downhill) and  $\Gamma^-$ , the tunneling rate to the left are independent. We obtain, as in the classical case,

$$R_0 = \frac{\hbar}{2e} \frac{1}{I} \frac{d\phi}{dt} \approx \frac{\hbar}{2e} \frac{1}{I} (2\pi) (\Gamma^+ - \Gamma^-) \quad (6.1)$$

To obtain a first estimate of  $R_0$  we use the WKB approximation result for  $\Gamma$ . The WKB tunneling rate was given in Chapter 2

$$\Gamma = \frac{\omega_0}{2\pi} \chi \sqrt{v} e^{-vs} \quad (6.2)$$

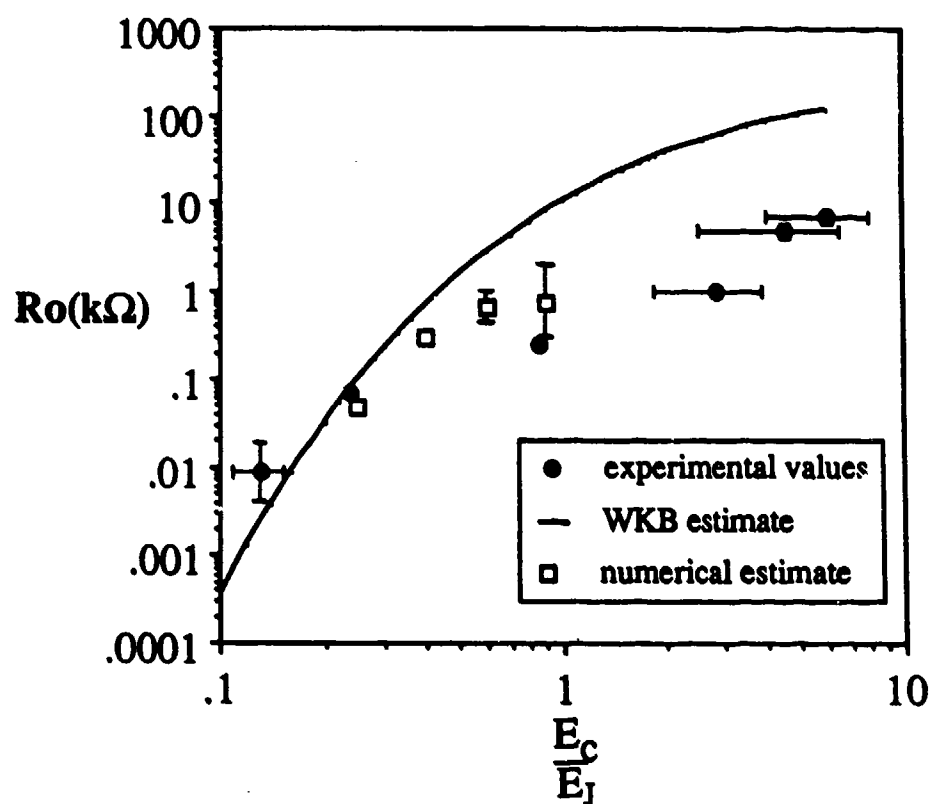


Fig. 6.1:  $R_0$  vs.  $x = E_C/E_J$ . Comparison of experimental values, values obtained using the WKB approximation, and values obtained numerically. The dashed horizontal value indicates the value of the quantum resistance  $R_Q = h/4e^2$ .

where  $\nu = (V_b/\hbar\omega_o)^{1/2}$ ,  $V_b$  is the barrier height, equal to  $2E_J \pm \hbar I/4e$ ,  $\omega_o$  is the classical resonant frequency of the well,  $\hbar\omega_o = \hbar\omega_p = (8E_J E_C)^{1/2}$ , at  $I \ll I_{co}$ .  $\chi$  and  $s$  are numerical constants, which are functions of the shape of the potential and of the damping. For the cubic potential approximation, and assuming low damping  $\chi \approx 52.1$ ,  $s \approx 7.2$ . Combining (6.1) and (6.2), we obtain an analytical estimate for  $R_o$ , which we compare with the measured low temperature values in Fig. 6.1. While the value of  $R_o$  for the sample with  $R_n = 14.8 \text{ k}\Omega$  ( $x \approx 0.25$ ) is in good agreement with the estimate, the samples with large  $x$  exhibit values of  $R_o$  considerably lower than the estimate.

In the large  $E_C$  limit, it seems apparent from Fig. 6.1 that characteristic low- $T$  values of  $R_o$  approach a value of order  $R_Q = \hbar/4e^2 \approx 6.1 \text{ k}\Omega$ . We do not believe this to be fortuitous. If we take a maximum reasonable energy level width equal to the barrier height  $\delta E \approx 2E_J \pm \hbar I/4e$ , the net escape rate to the right becomes  $\Gamma^+ - \Gamma^- = (2\pi)\hbar/2e$ . Using (6.3), we have  $R_o = (\hbar/2eI)(2\pi)\hbar/2e = (2\pi)\hbar/4e^2$ , which is in reasonably good agreement with the trend in Fig. 6.1.

One large source of discrepancy in some of our comparisons is the inaccuracy of WKB tunneling estimates for values of  $x > 1$ . In this range, the width of  $\psi(\phi)$  becomes comparable to the well spacing, and only one energy level is found in the well. Thus the semiclassical WKB approximation is no longer appropriate. To obtain a better estimate for the tunneling rate in the regime with  $x$  near 1, we have carried out a numerical calculation. We isolate a single well of the Josephson potential by considering the potential  $U_A$  shown in Fig. 6.2. For any energy, one can integrate the Schrödinger equation to find the resulting wavefunction  $\psi_E(\phi)$ . We consider an initial condition  $\psi(t=0) = \psi_o$  chosen to be essentially localized in the potential well;  $\psi_o$  is defined by us as the ground state of the potential  $U_B$  shown in Fig. 6.2. We then expand  $\psi_o$  using the  $\psi_E(\phi)$  wavefunctions, and compute the time evolution  $\psi(t)$ . Finally, we can extract the probability that the system has

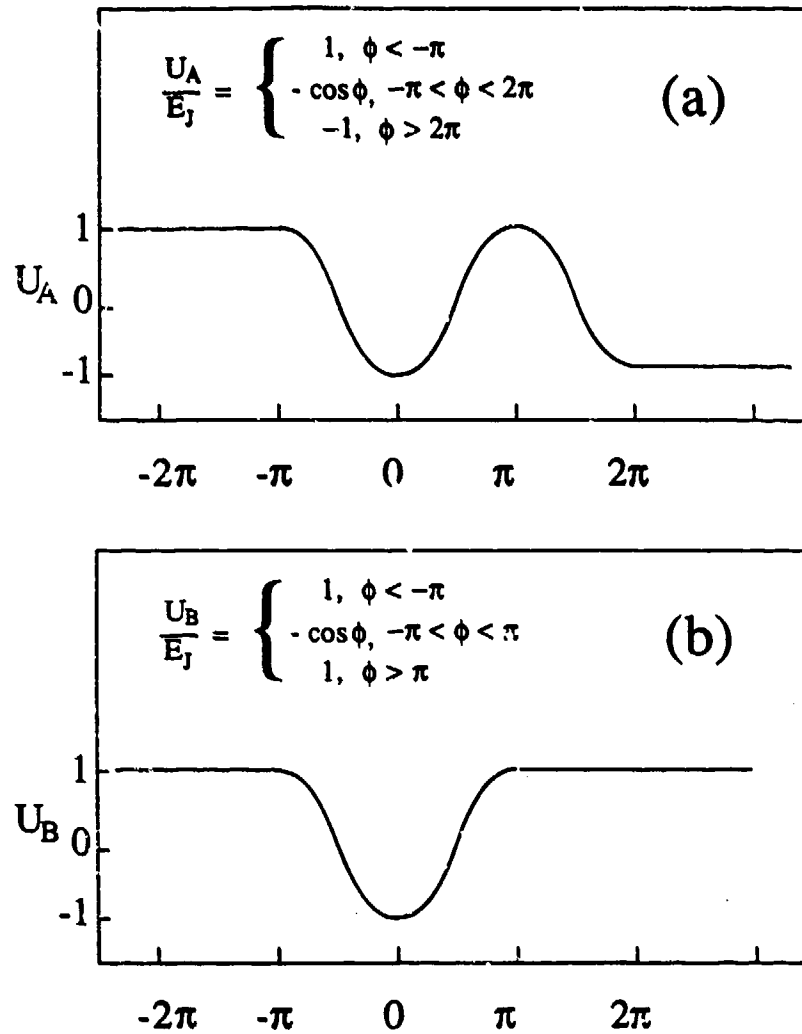


Fig. 6.2: The two different potentials used in the numerical calculations of  $R_0$ . (a) Metastable potential, used to calculate  $\psi_E$ . (b) Stable potential, used to calculate  $\psi_0$ .

not tunneled, which we call  $P(t)$ , from the projection of  $\psi(t)$  on  $\psi_0$ ;  $P(t) \propto |\int \psi_0^* \psi(t)|^2$ .

We define a normalized spectral weight

$$f(E) = \frac{|\int \psi_0^* \psi_E|^2}{A} \quad (6.3)$$

where  $A$  is the normalization constant given by  $A = \int \psi_0^* \psi_0 \int \psi_E^* \psi_E$ . We then have

$$P(t) = \left| \int dE f(E) e^{-iEt/\hbar} \right|^2 \quad (6.4)$$

Insofar as the shape of  $f(E)$  is approximately Lorentzian, with full width at half maximum of  $\delta E$ , then we may approximate  $P(t)$  by a function of the form  $e^{-t/\tau}$ . The escape rate  $\tau^{-1}$  is then given by

$$\frac{\hbar}{\tau} = \delta E \quad (6.5)$$

Fig. 6.3 shows a comparison of escape rates calculated with the WKB formula (6.2) and by the numerical technique discussed above. We see that, while for values of  $x \ll 1$  the results of the two calculation methods converge, for  $x > 0.5$  there is considerable discrepancy, as expected; the tunneling rate calculated by the wavefunction expansion method outlined above is significantly lower. In particular, note that the numerical estimate yields  $\delta E < E_J$ , which is self-consistent, whereas the WKB escape rates give  $\delta E > E_J$ , which is conceptually inconsistent with the escape out of a well of depth  $E_J$ . This systematic difference in lifetime is also in the right direction to improve the agreement with the observed values of  $R_0$ .

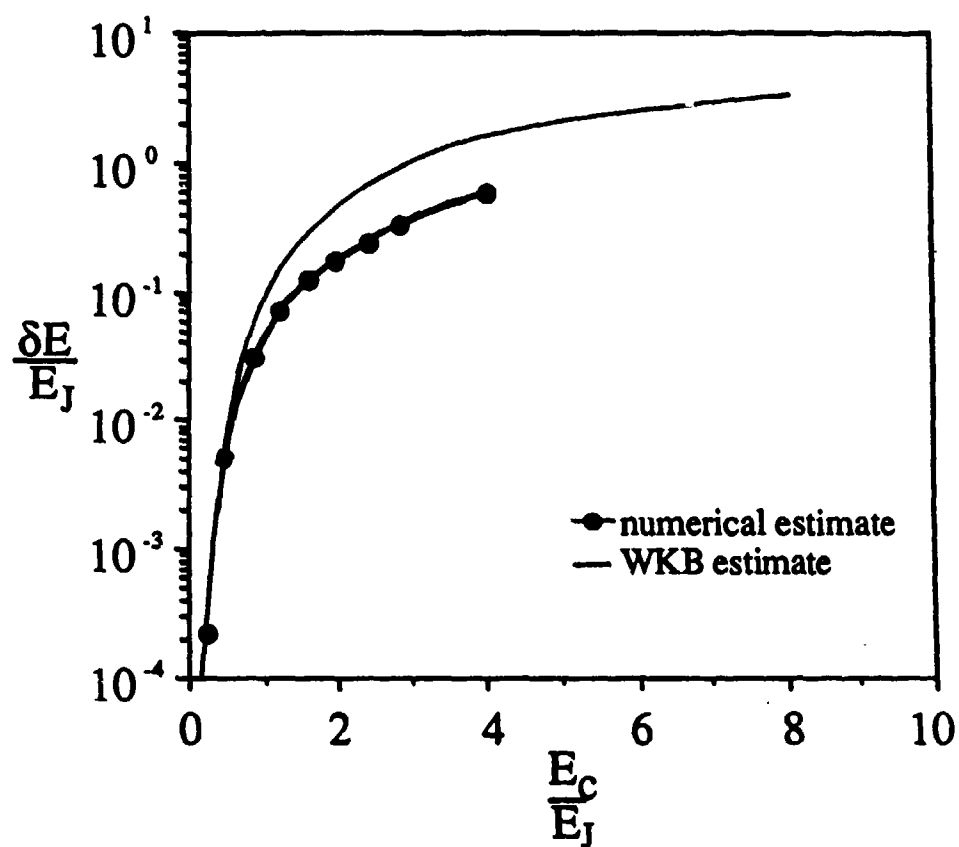


Fig. 6.3: Comparison of WKB and numerical estimates for the escape rate, expressed as a normalized energy width, and therefore only dependent on  $x$ .  $\Delta E = \hbar/\tau$ , where  $1/\tau$  is the escape rate.



We obtain direct numerical estimates for  $R_0$  by calculating the escape rates  $\Gamma^+$  and  $\Gamma^-$  after small positive and negative (respectively) currents have been applied, tilting the potential. The numerical estimates for  $R_0$  are shown in Fig. 6.1, in comparison with the WKB estimates and the experimental values. While the wavefunction expansion method allows us to obtain reasonable estimates in the regime with  $x$  near 1, where WKB methods have broken down, its range of validity is also limited. As  $x$  becomes larger than one, the range of bias current  $I$  giving a constant  $R_0$  is very small, making estimates of  $R_0$  very inaccurate. For  $x$  distinctly larger than one, the calculated  $f(E)$  also no longer resembles a Lorentzian bell shape, and  $P(t)$  can no longer be approximated by a decaying exponential. At this point the quantum phase uncertainty approaches one well spacing, and our assumption of a well defined exponential escape rate necessary for evaluating (6.3) breaks down: other methods must be used to estimate  $R_0$ . The numerical calculations are an improvement over the WKB estimates, but a more refined model, perhaps taking into account coherent reflections between subsequent wells is needed.

While our model is inaccurate for  $x > 1$ , it provides a very good account of the behavior of our sample with normal resistance  $14.8 \text{ k}\Omega$ . For this sample,  $x$  is only about 0.25, so that  $\psi(\phi)$  should have relatively small width compared to the spacing between Josephson potential wells, and our model appears reasonable. As shown in Fig. 6.4, the estimated value is in very good agreement with the low temperature value of  $R_0$ . Moreover, the crossover temperature at which the system apparently goes from this quantum tunneling limit to thermally activated escape is in excellent agreement with the  $T_{\text{cross}} = \hbar\omega_p/2\pi k_B$ , as expected from (2.34). The predicted values of  $R_0(0)$  and of  $T_{\text{cross}}$  contain no adjustable parameters:  $R_n$  is measured, and the capacitance is given by the estimated intrinsic capacitance  $C_i$ . This value of the capacitance is also in agreement with that involving the charging effects described in Chapter 4, and interpreted below in section 6.4.

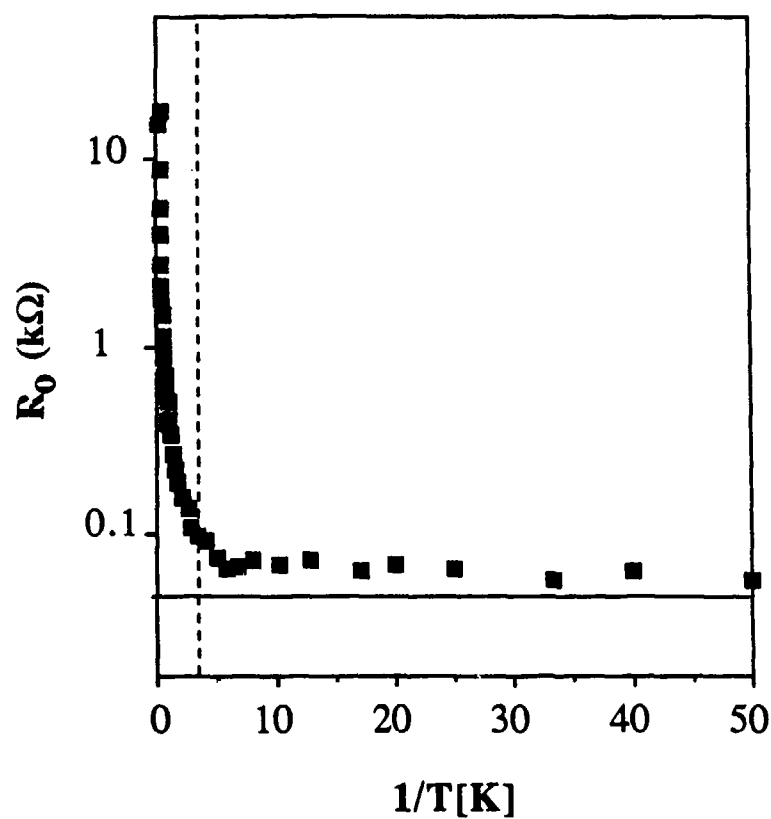


Fig. 6.4:  $R_0$  vs.  $T^{-1}$  for the sample with  $R_N = 14.8 \text{ k}\Omega$ . The horizontal line is the zero temperature estimate obtained by numerical methods. The dashed vertical line corresponds to  $T = \hbar\omega_p/2\pi k_B$ , at which the crossover to the quantum limit should occur.

This success in fitting the measurements performed on the sample with  $R_n = 14.8 k\Omega$ , is perhaps an indication that the simple underdamped arguments used above are indeed appropriate. The effect of damping is, in general, to reduce the tunneling rate and the phase fluctuations. In the semiclassical limit, we discussed in Chapter 2 that for damping to have a significant effect,  $\alpha$  must be of order of or greater than one, where  $\alpha$  is given by

$$\alpha = \frac{1}{\pi\sqrt{2}} \frac{R_Q}{R} \sqrt{\frac{E_c}{E_J}} \quad (6.6)$$

where  $R_Q = h/4e^2$  is the quantum unit of resistance. Using (6.6) as a rough guide, the underdamped results of this section should thus in fact be a good approximation as long as  $R_L$  is used as the resistance  $R$ , as was appropriate in the classical treatment of Chapter 5 since  $E_c \sim E_J$ , and  $R_L \sim 10 - 500 M\Omega \gg R_Q$  at low temperatures.

The success of this simple approach might be misleading. One of the critical steps in our treatment was that even though the tunneling rates were calculated in the underdamped limit, enough damping was assumed to be present to *retrap* the expectation value of the phase in the next well, after the tunneling event had taken place. It is unlikely that if the effect of the quasiparticles is completely described by the high resistance  $R_L$ , enough damping would be present to retrap the phase. Quite possibly, the effective damping resistance seen by the junction is frequency dependent, as was suggested by Ono *et al.* [1986]. A more sophisticated treatment, perhaps involving a time-domain approach to the tunneling process in the presence of damping, is needed to resolve these questions.

## 6.2. Interpretation of the Critical Current $I_c$

Having developed a picture of the evolution of the system which gives rise to a linear resistive voltage at low current values, we now address the question of the critical

current, i.e., up to what current level is this regime of slow phase slippage locally stable? As we have seen in the semi-classical regime, two aspects must be considered. There is an absolute limit ( $I_{co}$  in the semi-classical case) set by the binding energy of the phase-locked state, and there is a dynamic limit ( $I_r$  in the semi-classical case) set by the dissipation which prevents runaway and causes continual retrapping into the slow phase-slip (low voltage) regime. In the quantum regime, we are only able to provide an estimate for the "binding energy" of the phase locked state. Our estimate should thus serve as an approximate upper bound for the actual critical current  $I_c$ . Quantitative estimates for a "dynamic" critical current, which take into account of the device's relaxation by dissipation, are difficult in the quantum regime, and will be left to future work.

Because the state of the system is time-dependent in the presence of a current, which causes phase slippage, there is no simple way to find the analog of the classical maximum supercurrent,  $I_{co}$ , even at  $T = 0$ . However it seems plausible to argue that, just as  $I_{co} = 2eE_J/\hbar$  in that case, where  $E_J$  is the binding energy due to the cosine potential, in this case we might expect  $I_c = (2e/\hbar) \times (B.E.)$  where  $B.E.$  is the binding energy estimated in Chapter 2 by (2.16). The rationale is this: The work done by the current in an incremental phase shift is  $(\hbar/2e) I d\phi$ . For stability, this must be less than  $dE = [dE(\phi)/d\phi] d\phi$ . This leads to  $I < (2e/\hbar) [dE(\phi)/d\phi]_{max}$ , or  $2eE_J/\hbar$  for the classical case  $E(\phi) = -E_J \cos \phi$ . If we assume that the  $B.E.$  is lost for a phase shift  $\Delta\phi \sim 1$  in the quantum case as well, it follows that  $I_c = (2e/\hbar) (B.E.)$ . In particular, in the limit where  $E_J \ll E_c$ , we have  $B.E. = E_J^2/8E_c$  [from (2.16)], which leads to

$$I_c = (E_J/8E_c) I_{co} \quad (6.7)$$

Insofar as this formula is correct, the observed  $I_c$  should scale with  $R_n^{-2}$  rather than with  $R_n^{-1}$  as does  $I_{co}$ . In fact, just such a scaling with  $R_n^{-2}$  of  $I_c$  (extrapolated to  $T = 0$ ) is found for our highest resistance samples as shown in Fig. 6.5. Moreover, the absolute numerical

magnitudes are also in reasonable agreement if  $E_c$  is based on the same capacitance values of 1 - 2 fF used earlier in interpreting  $R_0$ . Again, this must be considered quite satisfactory in view of the approximate nature of the argument.

In a recent Comment on our 1988 *Physical Review Letter* article [Iansiti *et al.*, 1988a] Mirhashem and Ferrell [1988] have suggested a similar estimate for the reduction in  $I_c$  due to quantum phase fluctuations. They estimate the linear response of a Josephson junction by calculating the inverse inductance of the device, given by

$$L^{-1} = (2e/\hbar)^2 E_J \langle \cos \phi \rangle \quad (6.8)$$

where  $\langle \rangle$  denotes the ground state expectation value. As the ratio of  $E_c$  to  $E_J$  increases, quantum fluctuations increase, and  $\langle \cos \phi \rangle$  decreases. Assuming that the critical current scales with the linear response (as it does in the absence of fluctuations) they obtain, at large  $x = E_c/E_J$ ,

$$I_c = (E_J/4E_c) I_{c0} \quad (6.9)$$

which is a factor of 2 larger than (6.7). Fig. 6.6 shows a comparison of these two  $I_c$  estimates calculated for  $0 < x < 7$ , a range covering all our experimental data. While the Mirashem-Ferrell estimate is closer to the experimental values for large  $x$ , both approaches provide reasonably satisfactory agreement, given their approximate nature and the experimental uncertainty in  $C$ .

Insofar as this formula is correct, the observed  $I_c$  should scale with  $R_N^{-2}$  rather than with  $R_N^{-1}$  as does  $I_{co}$ . In fact, just such a scaling with  $R_N^{-2}$  of  $I_c$  (extrapolated to  $T = 0$ ) is found for our highest resistance samples as shown in Fig. 6.5. Moreover, the absolute numerical magnitudes are also in reasonable agreement if  $E_c$  is based on the same capacitance values of  $1 - 2$  fF used earlier in interpreting  $R_0$ . Again, this must be considered quite satisfactory in view of the approximate nature of the argument.

In a recent Comment on our 1988 *Physical Review Letter* article [Iansiti *et al.*, 1988a] Mirhashem and Ferrell [1988] have suggested a similar estimate for the reduction in  $I_c$  due to quantum phase fluctuations. They estimate the linear response of a Josephson junction by calculating the inverse inductance of the device, given by

$$L^{-1} = (2e/\hbar)^2 E_J \langle \cos \phi \rangle \quad (6.8)$$

where  $\langle \rangle$  denotes the ground state expectation value. As the ratio of  $E_c$  to  $E_J$  increases, quantum fluctuations increase, and  $\langle \cos \phi \rangle$  decreases. Assuming that the critical current scales with the linear response (as it does in the absence of fluctuations) they obtain, at large  $x = E_c/E_J$ ,

$$I_c = (E_J/4E_c) I_{co} \quad (6.9)$$

which is a factor of 2 larger than (6.7). Fig. 6.6 shows a comparison of these two  $I_c$  estimates calculated for  $0 < x < 7$ , a range covering all our experimental data. While the Mirhashem-Ferrell estimate is closer to the experimental values for large  $x$ , both approaches provide reasonably satisfactory agreement, given their approximate nature and the experimental uncertainty in  $C$ .

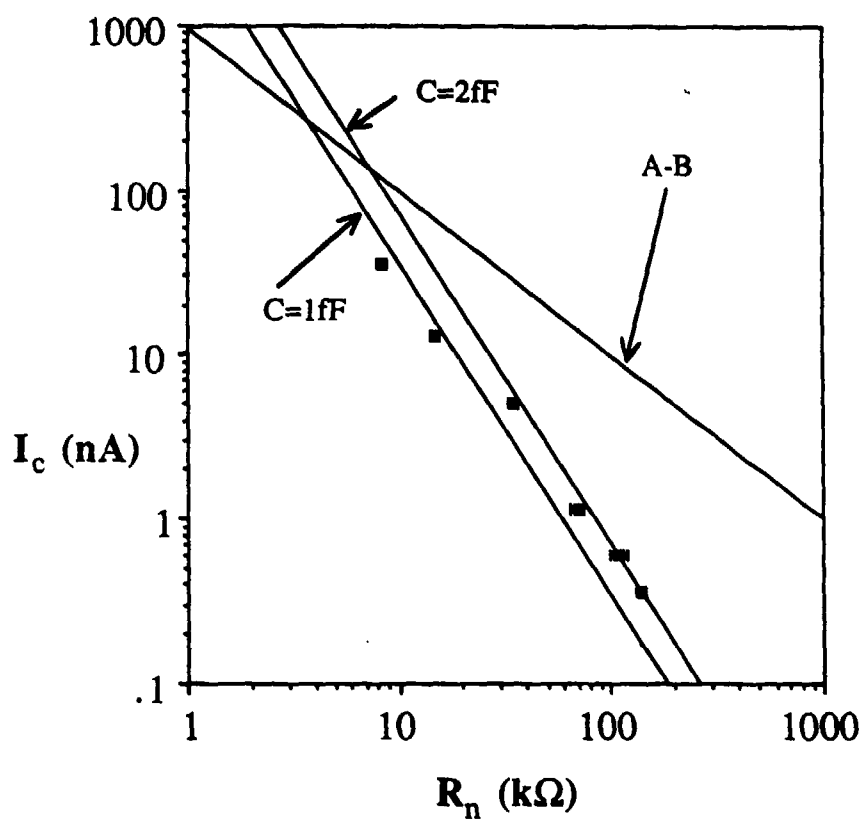


Fig. 6.5: Measured critical current  $I_c$  (at  $H=0$  and  $T=30mK$ ) for six samples (black squares). The A-B line is the Ambegaokar-Baratoff critical current prediction. The other two lines are our estimate (6.10), plotted for two reasonable capacitance values.

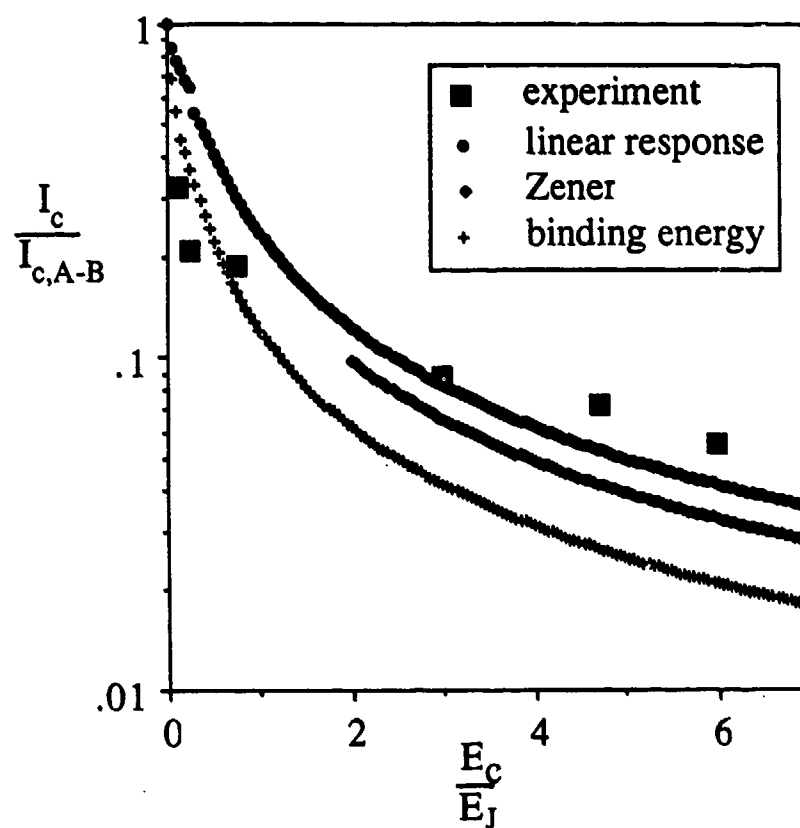


Fig. 6.6: Measured critical current  $I_c$  (at  $H=0$  and  $T=30mK$ ) for six samples (black squares), plotted against the estimated ratio of charging to Josephson coupling energy. Two of the estimates shown are obtained by our binding energy method (6.7), and by the linear response method by Mirhashem and Ferrell [1988] given in (6.9). The third estimate is our Zener tunneling estimate (only valid at large  $E_c/E_J$ ), given by (6.10).



### 6.3. Analysis in Q-space

The simple analysis we have provided in the previous sections is successful in providing a semiquantitative account of our observations in the regime with Josephson energy of order the charging energy ( $x \sim 1$ ). As we decrease the Josephson energy further, quantum phase fluctuations increase, and the behavior of the devices becomes increasingly difficult to characterize by models based in  $\phi$  space. It is useful to consider the opposite viewpoint. Several authors<sup>†</sup> have investigated Josephson junction dynamics in charge space, looking at the behavior of  $Q$ , the quantum mechanical conjugate of  $\phi$ . The energy spectrum of the Josephson device assumes a band-like structure, reminiscent of that of a one dimensional crystal. Such models appear particularly appropriate for the case  $E_C \gg E_J$  (that is,  $x \gg 1$ ), where the band structure approaches that of a free particle, with small energy gaps caused by the periodic Josephson potential. The essence of these models was described in Chapter 2. The dynamics in this limit, when a current is applied to the system, were described in Section 2.4.2, using the approach of Guinea and Schön [GS, 1986; 1987]. The energy spectrum GS derive, shown in Fig. 2.6, is shown again in Fig. 6.7. The current  $I$  equals  $dQ_x/dt$ . Whereas at low currents the system follows the lowest energy bands, at high currents the system begins to Zener tunnel into the higher bands. The Zener tunneling probability, as discussed in Section 2.4.2, is given by  $P_{\text{Zener}} \sim \exp(-I/I_Z)$ , where  $I_Z$  is given by

---

<sup>†</sup> See, for example, Chakravarty, [1982], Schmid, [1985], Likharev and Zorin, [1985], Mullen, Ben-Jacob, and Schuss, [1988], Ben-Jacob, Gefen, Mullen, and Schuss, [1988], Ben-Jacob, Gefen, Mullen, and Schuss, [1985], Widom, Megaloudis, Clark, Prance, and Prance, [1984], and references therein, Fisher and Zwerger, [1985], Zwerger, [1987], Fisher, [1986], Guinea and Schön, [1986; 1987], Büttiker, [1987].

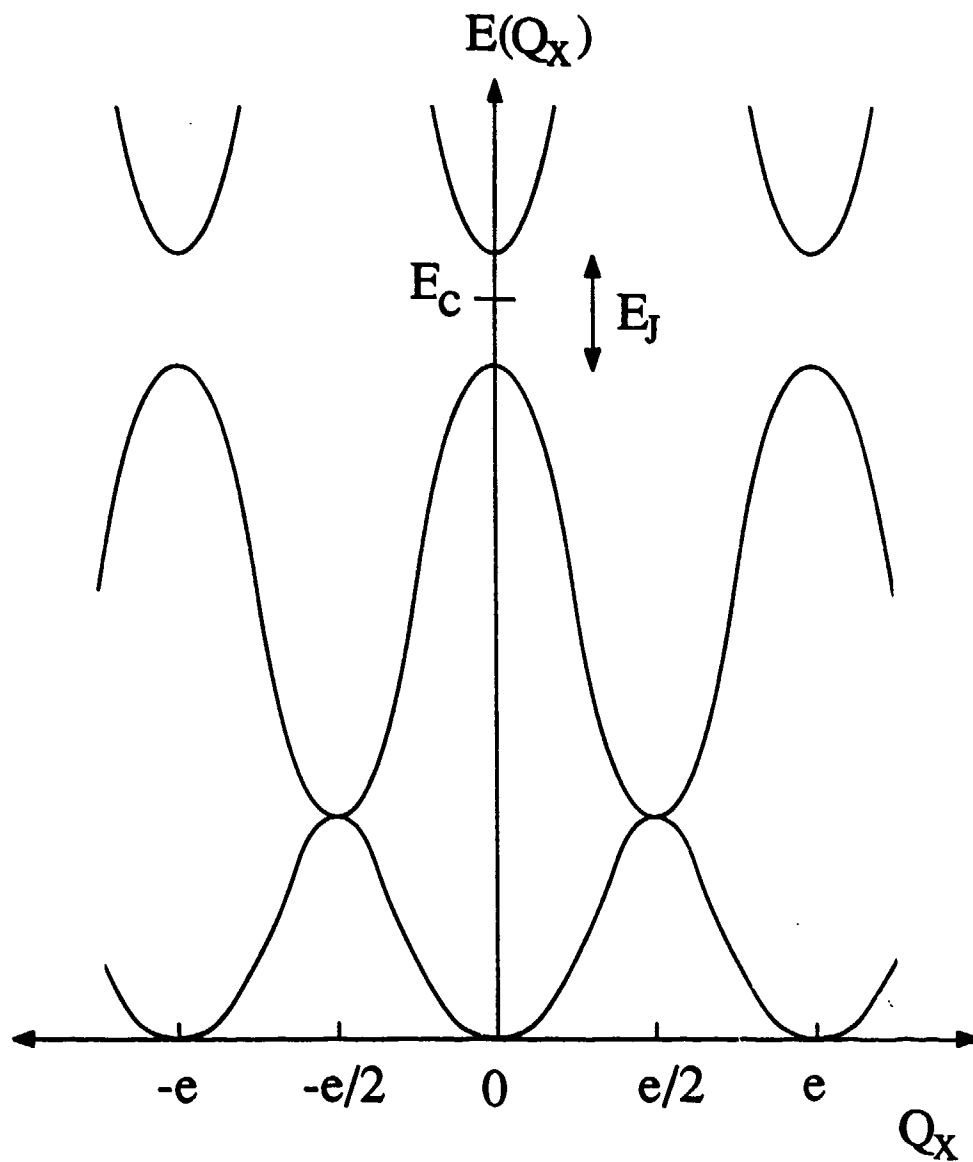


Fig. 6.7: Sketch of the energy spectrum as a function of applied charge derived for a Josephson junction in the large charging energy limit. [After Guinea and Schön, 1987.]

$$I_Z = \pi e E_J^2 / 8 \hbar E_C = I_c = (\pi E_J / 16 E_C) I_{co} \quad (6.10)$$

We associate  $I_Z$  with the observed critical current  $I_c$ . A comparison of this critical current estimate with the experimental values is given in Fig. 6.5. The physical picture we have is that for  $I < I_Z$ , occasional Zener tunneling occurs, but the system quickly relaxes back down to the lowest band. The associated dissipation contributes to the resistance  $R_o$ , but this does not spell the end of the low voltage regime. Rather, we associate the end of this regime with the complete breakdown of the band gap, allowing the system to run up onto the upper, free-particle-like bands, where it acts "normal", i.e., as if  $E_J$  were zero. Because of the exponential dependence, one might expect our criterion to be correct to within a factor of 2; hence the three estimates (6.7), (6.9), and (6.10) are consistent within their expected accuracy. In particular, all three results share the property that  $I_c$  scales with  $E_J^2$  or  $R_n^{-2}$ , rather than with the first powers of these quantities, as does  $I_{co}$ .

At  $T > 0$ , the probability of thermal excitation across the band gap  $E_J$  would be expected to be approximately given by  $e^{-E_J/kT}$  on each cycle of the Bloch oscillation. If this probability is added to that given by (6.10), and the sum set equal to  $1/e$  in analogy to the above argument, we obtain a simple phenomenological estimate for the effect of temperature in reducing  $I_c$ . This argument gives the correct characteristic temperature for substantial reduction in  $I_c$ , namely  $E_J/k$ . This rough estimate was shown in Section 4.2.1 to be representative of our measurements.

In this approach, as in the  $\phi$ -space one, damping during the MQT process is expected to have a strong effect in reducing the tunnel probability, and hence increasing the estimated critical current. The physical arguments of Büttiker and Landauer [1986] suggest that we can still use

$$\frac{dE}{d\phi} = - \frac{\hbar}{2eR} \sqrt{\frac{2(E + E_J \cos \phi)}{C}} \quad (6.11)$$

(which was discussed in Chapter 2 in the classical regime) at least approximately, in the MQT case by taking the absolute value of the quantity under the radical. Thus in the present case it has a similar value in the barrier and in the well. However, the question is what value of  $R$  is physically correct to be inserted into this formula. We can say that  $R \approx R_N$  would be consistent with our data, in that it would introduce rather modest corrections which could be accommodated by choosing a different criterion for  $I_C$ , such as the criterion that  $P_Z$  be set equal to  $e^{-2}$  rather than  $e^{-1}$ . On the other hand,  $R_L$  is so large that its damping effects would be negligible in this regime. Likewise,  $R_O$  is sufficiently below  $R_N$  at low temperatures that it would, if applicable, give such large corrections as to be very difficult to reconcile with the data. Even more inconsistent with the data would be any damping resistance comparable with the impedance of free space  $Z_0 = 377 \Omega$ , such as the characteristic impedance of the leads attached to the junction.

#### 6.4. Coexistence of Coulomb Blockade and Josephson Tunneling

We have provided a number of semiquantitative models accounting for the basic features of our I-V curves observed at zero magnetic field. As described above, however, we also performed a second set of experiments: By applying a magnetic field to the junctions, we depressed the Josephson coupling even further. At low field values we obtained measurements similar to the ones made at zero field, with  $R_O$  increasing and  $I_C$  decreasing, as the field was increased. At higher fields, however, we discovered a new regime, exemplified by the I-V curve shown in Fig. 1.4. As mentioned above, the new striking feature is the *coexistence* of a sharp knee at a voltage corresponding to  $e/2C$ , with a very sharp voltage jump at a "critical current"  $I_C$ .

We have proposed [Iansiti, *et al.*, 1988a; 1988b] the following simplified phenomenological picture: The difference in electrostatic energy due to the transfer of a

single electron is  $e^2/2C$ . In our samples this energy is large, typically of order  $1\text{ K}$ . At low voltages, below  $e/2C$ , the system does not acquire enough energy from the source in the tunneling process to offset the increase in electrostatic energy involved. Tunneling is therefore energetically unfavourable and is inhibited, provided the temperature is low enough for thermal activation processes to freeze out. This yields a static situation; electrons are "trapped" on the junction electrodes and the dynamic resistance is extremely high. As  $V$  becomes greater than  $e/2C$ , on the other hand, a single electron transfer becomes energetically favorable, and the differential resistance decreases, giving rise to a knee in the  $I$ - $V$  curve at that voltage. In this dynamic regime, if the instantaneous voltage increases beyond  $e/C$ , it becomes energetically favorable also for Cooper pairs to tunnel, and the voltage is driven back down. The observed average voltage is thus restricted to a value below  $e/C$ , until the system's ability to transfer Cooper pairs is exceeded at  $I=I_c$ . It thus appears that Josephson tunneling plays an important role in the explanation of the observed plateau in the  $I$ - $V$  curve and the subsequent critical current.

This explanation can be restated in terms of the band model described in Section 4.3. The highly resistive part of the  $I$ - $V$  curve may then be due to the system being trapped at a fixed charge on the lowest band. This configuration is, however, only stable for  $V < e/2C$ . At higher (average) voltages, the system must spend time in higher bands and tends to relax to lower bands by electron tunneling, conducting charge and reducing the differential resistance of the device. This happens until the current is large enough for Zener processes to become so likely that the Josephson band gaps are ineffective at keeping the system in low bands. At this point ( $I=I_c$ ) the voltage rises sharply to the energy gap.

This interpretation raises questions about the most realistic way to model the source of current in the experimental setup. If an *ideal* source were feeding current to the system, charge could not be trapped on the electrodes, and  $Q_x$  could not remain *fixed* on one of the branches of the energy spectrum, at low currents. Our *actual* current source was described in Chapter 3. Naturally, if the leads are included in the treatment, the source acquires a

frequency-dependent impedance. The applied current is then constant only if we average over timescales longer than those characteristic of the leads. At the fast timescales relevant to the dynamics of the device, the characteristic impedance of the source is likely to be much lower than the nominal  $500\text{ M}\Omega$  of the distant room temperature dc biasing circuit. More appropriate characteristic values might depend on the transmission line properties of the leads, and could hardly be expected to be larger than a few  $\text{k}\Omega$ 's. On the other hand, our apparently successful interpretation of the zero-magnetic-field results successfully relied on the assumption that the junctions are in the underdamped limit, which would imply that the characteristic impedance seen by the devices was at least larger than  $R_Q \sim 6\text{ k}\Omega$ .

While these considerations are by no means resolved, it is not inconceivable that, depending on the intrinsic impedance of the junction, charge could either become trapped on the electrodes or flow through the junction at a steady rate. The RCSJ model describes the impedance of the Josephson junction as the parallel combination of three channels. The Josephson channel is inductive, and shorts out the junction at reasonably low frequency. However, in the quantum regime, the Josephson inductance is given by (6.8), which diverges as  $\langle \cos \phi \rangle \rightarrow 0$ , i.e. as quantum phase fluctuations increase. Therefore, as the ratio of charging to Josephson energy increases, the intrinsic impedance of a Josephson device also increases; the room temperature current source might become ineffective, at timescales short compared to the time constant of the experimental set-up<sup>†</sup>. Charge might thus temporarily become trapped on the junction electrodes, giving rise to the very high resistance branch observed on the I-V characteristics at low currents.

---

<sup>†</sup> Which is quite long, of order one msec.

## CHAPTER 7

### CONCLUSIONS

This report describes the first study of submicron thin film devices lithographically patterned in this laboratory. To carry it out, we fabricated high quality high resistance Sn-SnOx-Sn tunnel junctions using an electron-beam patterning facility, which in part was developed and built specifically for this experiment. Samples in single, double, and eleven-junction-array configurations were successfully fabricated. The measurements were performed in a dilution refrigerator, at temperatures between 20 mK and 4.2 K, and at magnetic fields between 0 and 3 T. These experiments yielded some striking results which probe the crossover region between the conventional Josephson regime, in which the Josephson energy  $E_J$  is much larger than the charging energy  $E_C$ , and the opposite regime, in which charging effects are dominant. These results are outlined below:

When the charging and Josephson energy are of comparable magnitude, the measured I-V characteristic is always resistive, even at low currents  $I < I_c$  (where  $R \equiv R_0 < R_N$ ); apparently the very low Josephson barrier height, comparable to  $k_B T$  or to the energy-level width, causes very frequent phase slips, due to thermal activation and/or quantum tunneling. The critical current itself, now defined as the current at which the average phase slip rate sharply increases to the energy gap frequency, is greatly reduced below the unfluctuated Ambegaokar-Baratoff critical current  $I_{c0}$ , even at the lowest temperatures, and apparently scales with the binding energy of the ground state, i.e. with  $R_N^{-2}$  for  $E_C > E_J$ .

If the Josephson energy is reduced to a value much smaller than the charging energy, by applying a magnetic field, we discover a new regime. The I-V characteristic becomes very resistive ( $R \sim R_L \gg R_N$ ) at low currents, with a sharp knee at a voltage apparently corresponding to  $e/2C$ . The average phase slip rate increases very quickly at low currents, as the Josephson potential seems too weak to localize  $\phi$ . While quantum fluctuations in  $\phi$  are presumably large, the charge now seems classically well defined. This

is perhaps demonstrated by the knee at  $e/2C$ , the voltage difference required before the tunneling of a single electron becomes favored despite the capacitive energy  $Q^2/2C$ .

Since we have attempted to explore a relatively new regime in the behavior of Josephson devices, we have raised a number of puzzling and as yet unresolved questions. Among these, perhaps the most striking one relates to the apparent isolation of the devices we studied from the outside environment: why are the contributions of parasitic capacitance, and the impedance of the leads, apparently *not* overwhelming the dynamics of our small junctions? Our findings appear to be in agreement with measurements made on scanning tunneling microscopes [see Van Bentum *et al.*, 1987; Hartmann, *et al.*, 1988]. However, little consensus has been reached on the reason for this puzzling observation. To what extent can the dynamics of a mesoscopic device be accurately modeled using standard circuit techniques? More work, both on the experimental and theoretical side, seems warranted before this controversy is resolved.

A more specific question can be asked about the nature of the damping that is affecting the behavior of our devices. What is the damping mechanism that leads to the observation of the low current resistance  $R_0$ , while the junction I-V curve is still hysteretic? We have provided a few simple phenomenological models which are consistent with our observations, but much additional work is required before comprehensive understanding and a truly quantitative agreement is reached.

At least three broad and separate areas come to mind in which further experimental work could be performed both to attempt to answer some of these questions, and to extend our findings to other areas of current interest. First of all, challenging experimental goals can be set regarding the measurement of the actual high frequency response of our small junctions, and the observation of Bloch oscillations, by synchronizing the passage of electrons through the barrier with external microwave radiation. Such measurements might



provide further confirmation of some of the models presented in this report, and give very useful information on the damping mechanism which governs the behavior of our devices.

A second possible area of extension is the measurement of two dimensional arrays of small Josephson junctions. A number of groups<sup>†</sup> have reported striking observations on *in situ* quench-condensed granular films of Sn and other superconducting materials. Apparently, if the film normal resistance is larger than the quantum resistance ( $R_Q = h/4e^2 \sim 6 \text{ k}\Omega$ ), the film is resistive at all temperatures, independent of the material and grain size (and thus geometrical capacitance). Several theoretical models<sup>‡</sup> have been presented to account for these observations, many of which model the films as an array of Josephson devices. These results are reminiscent of ours, since the junctions we measured were found to be resistive at all currents and temperatures, as long as their normal resistance was larger than a few  $\text{k}\Omega$ 's (see Fig. 4.5). Of course, the models developed in this work relate the behavior of our junctions to the value of their charging energy  $e^2/2C$ , and are thus strongly dependent on the capacitance. Still, our findings might well be related to the granular film measurements, perhaps by interchanging the effect of geometrical capacitance with the effect of ideal low temperature frequency-dependent quasiparticle damping [which contributes an effective capacitance given by (2.38)]. The measurement of 2-d arrays of patterned superconducting junctions might be an effective way to test and extend these ideas and provide information on phase transitions in a two dimensional system in the presence of quantum fluctuations. The fabrication scheme developed in this work would probably lend itself very well to the fabrication of relatively large ( $50 \times 50$ ) arrays of high quality small tunnel junctions which would be well suited for such experiments.

---

<sup>†</sup> See, for example, Orr *et al.*, [1986], Dynes, *et al.*, [1978], Hebard and Paalanen, [1984].

<sup>‡</sup> See, for example, Chakravarty *et al.*, [1986], Fisher [1986], Zwerger [1987], Ferrell [1988].

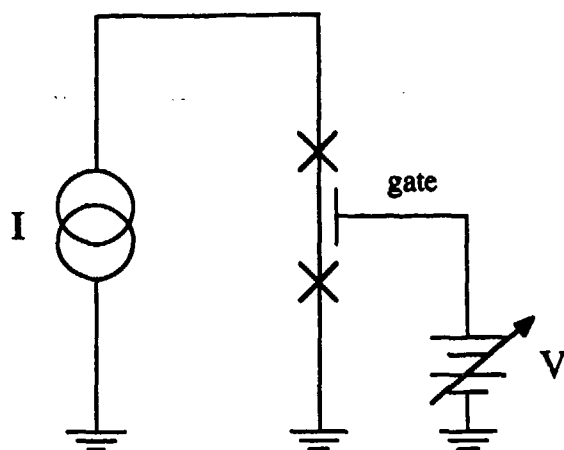


Fig. 7.1: The three terminal configuration of Fulton and Dolan. [After Fulton and Dolan, 1987.] The capacitive electrode was implanted on the back of the substrate.

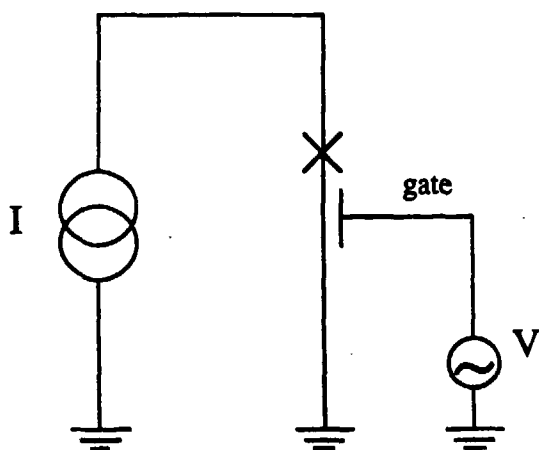


Fig. 7.2: A novel three terminal configuration: The capacitive electrode should be placed as close as possible to the rest of device. The gate voltage, in this case, would have to be provided by an ac source, such as a pulse generator.

The third area of extension regards the possible use of small tunnel junctions in a three-terminal device. Fulton and Dolan [1987] have awakened considerable interest in a clever sample configuration (shown schematically in Fig. 7.1) in which a very small metallic strip is isolated from the environment by two small tunnel junctions. In their case, the junctions are so small that the charging energy overwhelms the Josephson energy of the device. The charge trapped on the strip is modulated by means of a capacitively coupled electrode, the gate. The response of the device, measured across the two junctions, is naturally very nonlinear, by virtue of the sharpness of the superconducting energy gap structure. The dynamic resistance of the device can then be varied over a considerable range by varying the voltage applied to the capacitively coupled electrode. We believe that it would be interesting to study this type of device in the regime where the Josephson and charging energy are comparable. Could one induce a switch between the low voltage branch to the high voltage branch of the I-V curve by applying a voltage to the capacitively coupled electrode? It might also be interesting to consider the simple configuration shown in Fig. 7.2. Only one junction is required in the configuration. Naturally, on long time scales, the capacitance between the gate and the device is very large, since the second junction is not present to isolate the device from the leads. However, on *very* short time scales, enough charge might build up on the gate side of the junction to affect the dynamics of the device, perhaps inducing a switch between branches of the I-V curve.

In conclusion, we have experimentally investigated the competition between charging, Josephson, and thermal energies in mesoscopic tunnel junctions. Furthermore, we have presented a series of simple phenomenological models which provide satisfactory semiquantitative explanations of some of the remarkable phenomena observed experimentally, and may be a useful starting point for more rigorous theoretical treatments. Our observations also raise a number of interesting unresolved questions which provide the incentive for new experimental and theoretical work.

## REFERENCES

- Akoh, H., O. Liengme, M. Iansiti, M. Tinkham, and J. U. Free, Phys. Rev. B33, 2038 (1986).
- Ambegaokar, V., and A. Baratoff, Phys. Rev. Lett. 10, 486 (1963).
- Ambegaokar, V., and B. I. Halperin, Phys. Rev. Lett. 22, 1364 (1969).
- Ambegaokar, V., U. Eckern, and G. Schön, Phys. Rev. Lett. 48, 1745 (1982).
- Averin, D.V., and K. K. Likharev, J. Low Temp. Phys. 62, 345 (1986).
- Barner, J.B., and S. T. Ruggiero, Phys. Rev. Lett. 59, 807 (1987).
- Barone, A., and G. Paterno', *Physics and Applications of the Josephson Effect* (Wiley and Sons, New York, 1982).
- Barone, A., R. Cristiano, and P. Silvestrini, J. Appl. Phys. 58, 3822 (1985).
- Ben Jacob, E., D. J. Bergman, B. J. Matkowsky, and Z. Schuss, Phys. Rev. A26, 2805 (1982).
- Ben-Jacob, E., Y. Gefen, K. Mullen, and Z. Schuss, in *IC SQUID, Berlin, 1985*, H. D. Hahlbohm and H. Lubbig, eds. (deGruyter, Berlin, 1985).
- Ben-Jacob, E., Y. Gefen, K. Mullen, and Z. Schuss, Phys. Rev. B37, 7400 (1988).
- Blonder, G.E., M. Tinkham, and T. M. Klapwijk, Phys. Rev. B25, 4515 (1982).
- Büttiker, M. and R. Landauer, IBM J. Res. Dev. 30, 451 (1986).
- Büttiker, M., E. P. Harris, and R. Landauer, Phys. Rev. B28, 1268 (1983).
- Büttiker, M., Phys. Rev. B36, 3548 (1987).
- Caldeira, A.O., and A. J. Leggett, Ann. Phys. (N.Y.) 149, 374 (1983).
- Caldeira, A.O., and A. J. Leggett, Phys. Rev. Lett. 46, 211 (1981).
- Callan, C. G., and S. Coleman, Phys. Rev. D16, 1762 (1977).
- Cavicchi, R. E., and R. H. Silsbee, Phys. Rev. Lett. 52, 1453 (1985).
- Cavicchi, R.E., and R. H. Silsbee, Phys. Rev. B37, 706 (1988).
- Chakravarty, S., Phys. Rev. Lett. 49, 681 (1982).

Chang, L.D., and S. Chakravarty, Phys. Rev. B29, 130 (1984), and 30, 1566(E) (1984).

Cristiano, R. and P. Silvestrini, IEEE Trans. Magn., MAG-23, 771 (1987).

Cristiano, R. and P. Silvestrini, J. Appl. Phys. 60, 3243 (1986).

Danchi, W.C., J. B. Hansen, M. Octavio, F. Habbal, and M. Tinkham, Phys. Rev. B30, 2503 (1984).

Danchi, W.C., Ph.D. Thesis, Harvard University, unpublished, 1982.

den Boer, W., and R. de Bruyn Ouboter, Physica 98B, 185 (1980).

Devoret, M.H., J. M. Martinis, and J. Clarke, Phys. Rev. Lett. 55, 1908 (1985).

Devoret, M.H., J. M. Martinis, D. Esteve, and J. Clarke, Phys. Rev. Lett. 53, 1260 (1984).

Dolan, G.J., Appl. Phys. Lett. 31, 337 (1977).

Dolan, G.J., R. E. Miller, R. A. Linke, T. G. Phillips, and D. P. Woody, IEEE Trans. Magn. MAG-17, 684 (1981).

Eckern, U., G. Schön, and V. Ambegaokar, Phys. Rev. B30, 6419 (1984).

Fisher, M.P.A., and W. Zwerger, Phys. Rev. B32, 6190 (1985).

Fisher, M.P.A., Phys. Rev. Lett. 57, 885 (1986).

Fulton, T., and L. N. Dunkleberger, Phys. Rev. B9, 4760 (1974).

Fulton, T.A., and G. J. Dolan, Phys. Rev. Lett. 59, 109 (1987).

Giaever, I., and H. R. Zeller, Phys. Rev. Lett. 20, 1505 (1968).

Grabert, H., and U. Weiss, Phys. Rev. Lett. 53, 1787 (1984).

Grabert, H., in *IC SQUID, Berlin, 1985*, H. D. Hahlbohm and H. Lubbig, eds. (deGruyter, Berlin, 1985).

Grabert, H., P. Olschowski, and U. Weiss, Phys. Rev. B36, 1931 (1987).

Guinea, F., and G. Schön, Europhys. Lett. 1, 585 (1986).

Guinea, F., and G. Schön, J. Low Temp. Phys. 69, 219 (1987).

Hartmann, U., R. Berthe, and C. Heiden, to be published, (1988).

- Hänggi, P., *Annals N. Y. Academy of Sciences* **480**, 51 (1986).
- Hu, E.L., L. D. Jackel, and R. E. Howard, *IEEE Trans. on Electron Dev.*, *ED-28*, 1382 (1981).
- Iansiti, M., Q. Hu, R.M. Westervelt, and M. Tinkham, *Phys. Rev. Lett.* **55**, 746 (1985).
- Iansiti, M., A. T. Johnson, W. F. Smith, C. J. Lobb, and M. Tinkham, *Jap. J. of Appl. Phys.* **26**, Suppl 26-3, 1557 (1987), a.
- Iansiti, M., A.T. Johnson, W. F. Smith, H. Rogalla, C. J. Lobb, and M. Tinkham, *Phys. Rev. Lett.* **59**, 489 (1987),b.
- Iansiti, M., A. T. Johnson, C. J. Lobb, and M. Tinkham, *Phys. Rev. Lett.* **60**, 2414 (1988), a.
- Iansiti, M., A. T. Johnson, W. F. Smith, C. J. Lobb, and M. Tinkham, *Phys. Rev B*, submitted (1988), b.
- Jackel, L.D., J. P. Gordon, E. L. Hu, R. E. Howard, L. A. Fetter, D. M. Tennant, R. W. Epworth, and J. Kurkijärvi, *Phys. Rev. Lett.* **47**, 697 (1981).
- Kramers, H.A., *Physica (Utrecht)* **7**, 284 (1940).
- Kurkijärvi, J., *Phys. Rev.* **B6**, 832 (1972).
- Lambe, J., and R. C. Jaklevic, *Phys. Rev. Lett.* **22**, 1371 (1969).
- Lee, P.A., *J. Appl. Phys.* **42**, 325 (1971).
- Lee, P.A., A. D. Stone, and H. Fukuyama, *Phys. Rev.* **B35**, 1039 (1987).
- Likharev, K.K., and A. B. Zorin, *J. Low Temp. Phys.* **59**, 347 (1985).
- Louanasmaa, O.V., *Experimental Principles and Methods Below 1K* (Academic Press, London, 1974).
- Martinis, J.M., M. H. Devoret, and J. Clarke, *Phys. Rev. Lett.* **55**, 1543 (1985).
- McCumber, D.E., *J. Appl. Phys.* **39**, 3113 (1968).
- Mirhashem, B. and R. A. Ferrell, *Phys. Rev. Lett.* comment, submitted, (1988).
- Mullen, K., E. Ben-Jacob, and Z. Schuss, *Phys. Rev. Lett.* **60**, 1097 (1988).
- Naor, M., C. D. Tesche, and M. B. Ketchen, *Appl. Phys. Lett.* **41**, 202 (1982).

- Ono, R.H., M. J. Cromar, R. L. Kautz, R. J. Soulen, J. H. Colwell, and W. E. Fogle, IEEE Trans. Magn., MAG-23, 1670 (1987).
- Ott, H.W., *Noise Reduction Techniques in Electronic Systems* (John Wiley and Sons, New York, 1976).
- Prance, H., R. J. Prance, T. P. Spiller, J. E. Mutton, T. D. Clark, and R. Nest, Phys. Lett. 111A, 199 (1985).
- Prance, R.J., A. P. Long, T. D. Clark, A. Widom, J. E. Mutton, J. Sacco M. W. Potts, G. Megaloudis, and F. Goodall, Nature (Paris) 289, 543 (1981).
- Prance, R.J., T. D. Clark, J. E. Mutton, H. Prance, T. P. Spiller, and R. Nest, Phys. Lett. 107A, 133 (1985).
- Reed, M.A., J.N. Randall, R. J. Aggarwal, R.J. Matyi, T.M. Moore, and A. Wetsel, Phys. Rev. Lett. 60, 535 (1988).
- Richardson, R.C., and E.N. Smith, eds., *Experimental Techniques in Condensed Matter Physics at Low Temperatures* (Addison-Wesley, New York, 1988).
- Schmid, A., Phys. Rev. Lett. 51, 1505 (1985).
- Schwartz, D.B., B. Sen, C. N. Archie, and J. E. Lukens, Phys. Rev. Lett. 55, 1547 (1985).
- Silvestrini, P., O. Liengme, and K. E. Gray, Phys. Rev. B37, 1525 (1988).
- Silvestrini, P., S. Pagano, R. Cristiano, O. Liengme, and K. E. Gray, Phys. Rev. Lett. 60, 844 (1988).
- Skocpol, W.J., et al., Phys. Rev. Lett. 56, 2865 (1986).
- Stewart, W.C., Appl. Phys. Lett. 12, 277 (1968).
- Tinkham, M., *Introduction to Superconductivity* (McGraw-Hill, Inc., New York, 1975).
- Umbach, C.P., S. Washburn, R.B. Laibowitz, and R.A. Webb, Phys. Rev. B30, 4048 (1984).
- Van Bentum, P.J.M., H. van Kempen, L. E. C. van de Leemput, and P. A. A. Teunissen, Phys. Rev. Lett. 60, 369 (1988).

- Van Haesendonck, C., M. Gijs, and Y. Bruynseraede, in *Localization, Interaction, and Transport Phenomena*, B. Kramer, G. Bergmann, and Y. Bruynseraede, eds. (Springer-Verlag, Berlin, 1985), pp. 221-232.
- Voss, R.F., and R. A. Webb, Phys. Rev. Lett. **47**, 265 (1981).
- Wang, T.C., and R. I. Gailey, Phys. Rev. **B18**, 293 (1978).
- Washburn, S., R. A. Webb, R. F. Voss, and S. M. Faris, Phys. Rev. Lett. **54**, 2712 (1985).
- Widom, A., G. Megaloudis, T. D. Clark, H. Prance, and R. J. Prance, J. Low Temp. Phys. **57**, 651 (1984).
- Wittels, N.D., in *Fine Line Lithography*, R. Newman, ed. (North-Holland, New York, 1980).
- Zwerger, W., Phys. Rev. **B35**, 4737 (1987).



## APPENDIX ONE

### THE ELECTRON-BEAM LITHOGRAPHY SYSTEM

The electron-beam system used in the exposure process described in Chapter 3, consists of three components: an old JEOL 31 U scanning electron microscope, an IBM Instruments system 9000 microcomputer, and a box of interface electronics. The pattern to be exposed is loaded into the memory of the microcomputer, and a set of machine language routines<sup>‡</sup> sends out two digital sixteen bit signals, representing the X and Y channels, to the interfacing electronics. The interface box consists essentially of a power supply and two separate sets of Analogic digital/analog converters. The computer enables the D/A converters which interpret the two sixteen bit signals, convert them to voltages and send them to the X-Y driver of the electron microscope. A sketch of the interfacing electronics is given in Figs. A1.1 and A1.2.

---

<sup>‡</sup> Written by Dr. Horst Rogalla.

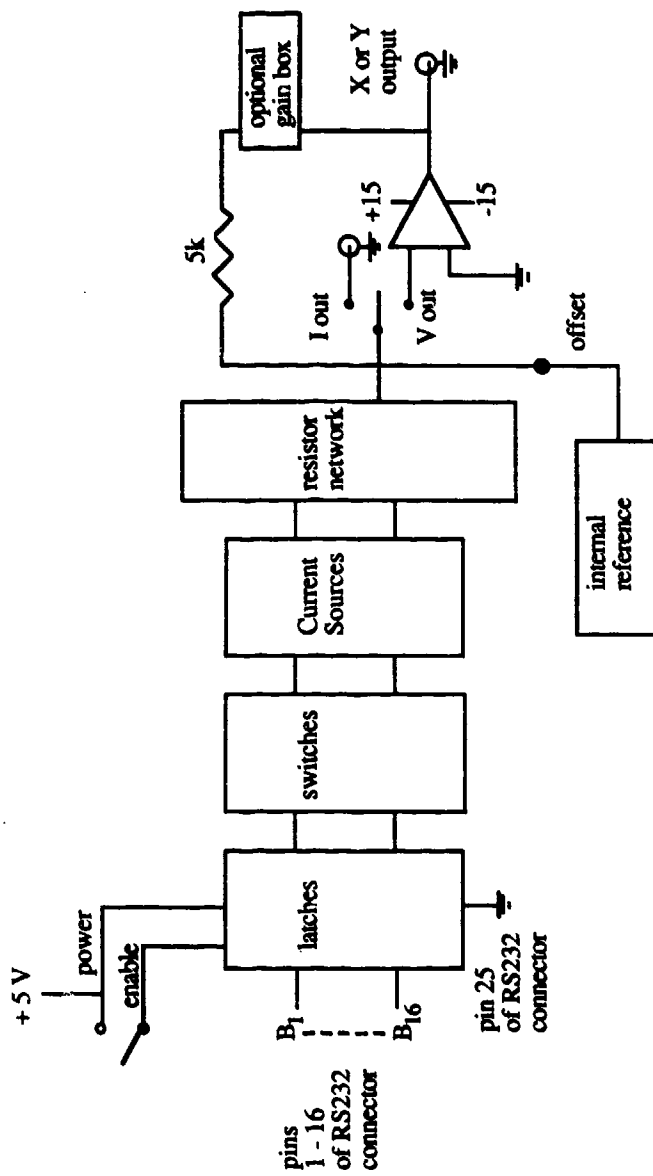


Fig A1.1.1: Schematic of one channel of the driver of the electron-beam writing system.

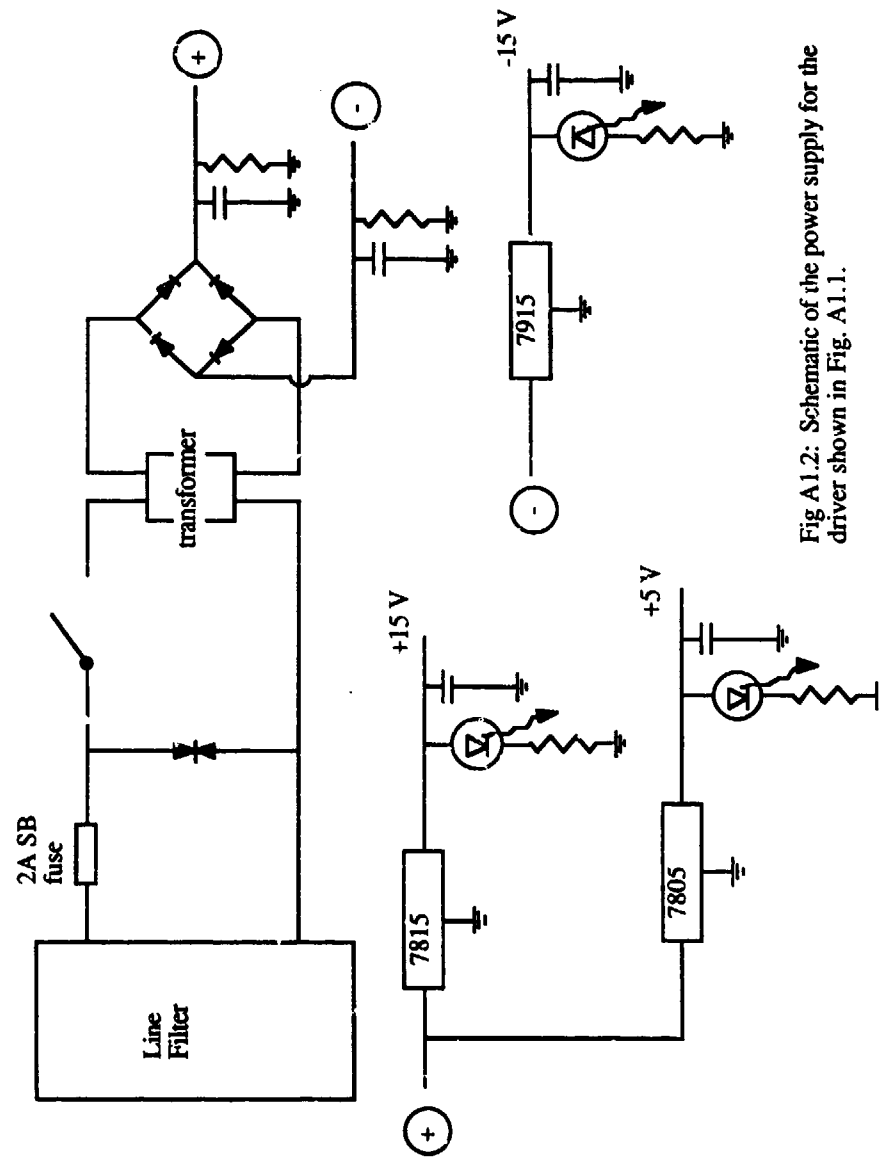


Fig A1.2: Schematic of the power supply for the driver shown in Fig. A1.1.

## APPENDIX TWO

### A SCHEMATIC OF THE COMPUTER CONTROLLED DATA ACQUISITION SYSTEM

A simple sketch of the acquisition system is shown in Fig. A2.1. The system is designed to measure the current at which a junction switches between the low and high voltage branches of the I-V curve, which we define as the critical current  $I_c$  of the device. As we explain in Chapter 2, in the presence of thermal activation or quantum tunneling,  $I_c$  acquires a stochastic character. By repeating the measurement of  $I_c$  many times, data can be accumulated on the switching distribution of the device, which can then be used to obtain information on the dynamics of the junction.

While a computer controlled acquisition system is convenient for the analysis of the data, digital computers tend to be quite noisy, and should be as far removed from the experiment as possible. By using opto-isolators and PAR 113 differential preamplifiers as buffers, as shown in Fig. A2.1, the computer is isolated from the experiment, which is also enclosed in a separate screened room.

To obtain a measurement of the critical current of the device, the computer first sends a low (0 V) trigger signal to the current source, which begins its sweep. the voltage across the Josephson junction will be at first low, for  $I < I_c$ , and switch to a value larger than 1 mV (for a Sn - Sn junction) at  $I = I_c$ . At this point the Schmitt trigger, which is simply a level crossing detector with hysteresis, sends a low signal (0 V) to the current source, which holds its current at a constant value. The Schmitt trigger low signal also enables the computer to perform the measurement of the critical current. The cycle is then repeated, to obtain an accurate distribution of  $I_c$  values. The maximum  $I_c$  sampling rate is about 1 kHz. A plot of the voltages vs. time in key parts of the system is shown in Fig. A2.2. Fig. A2.3 and A2.4 are schematics of the current source and of one of the opto-isolators.

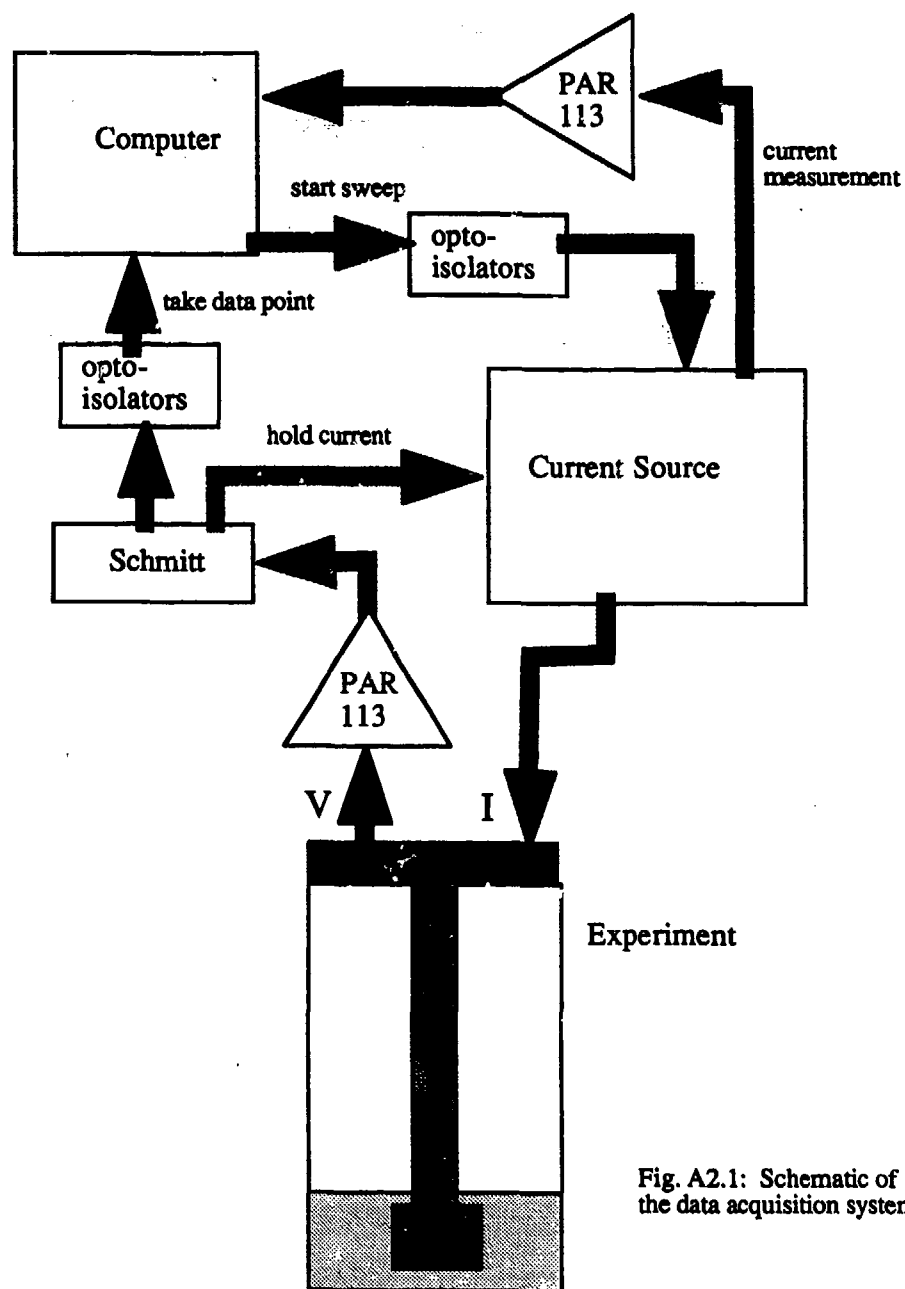


Fig. A2.1: Schematic of the data acquisition system

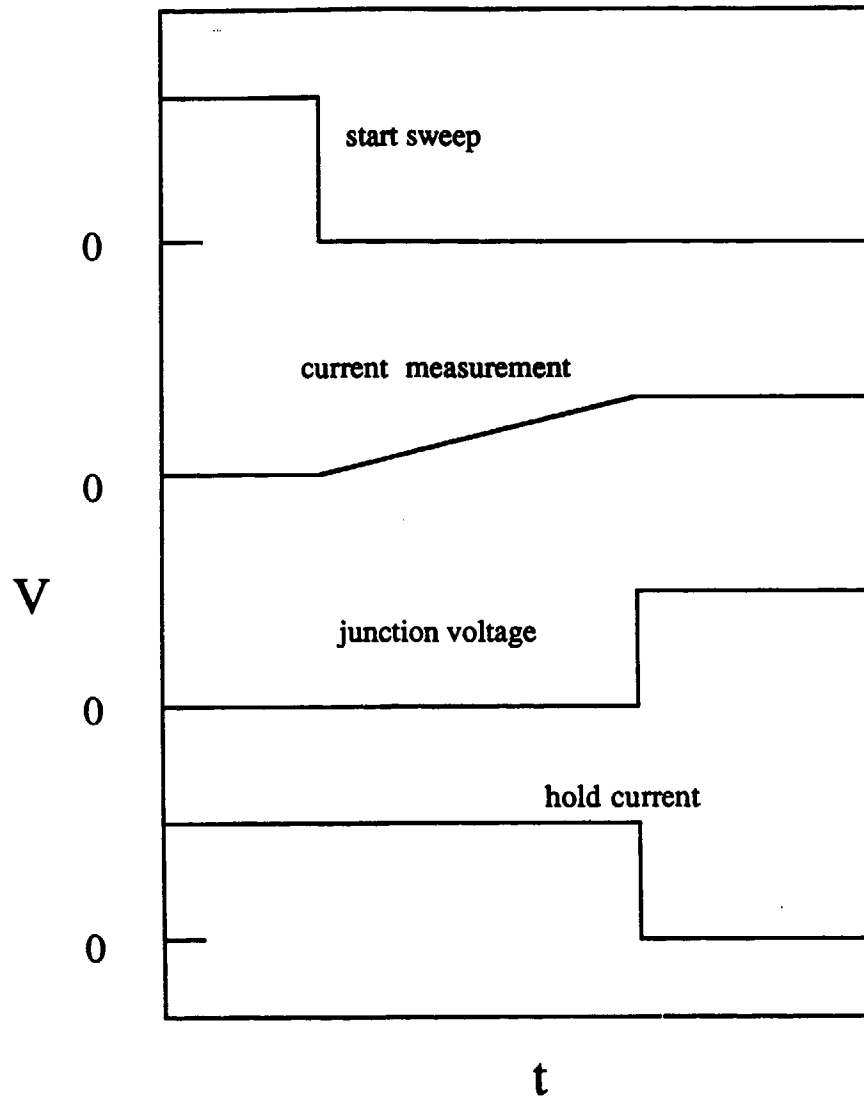
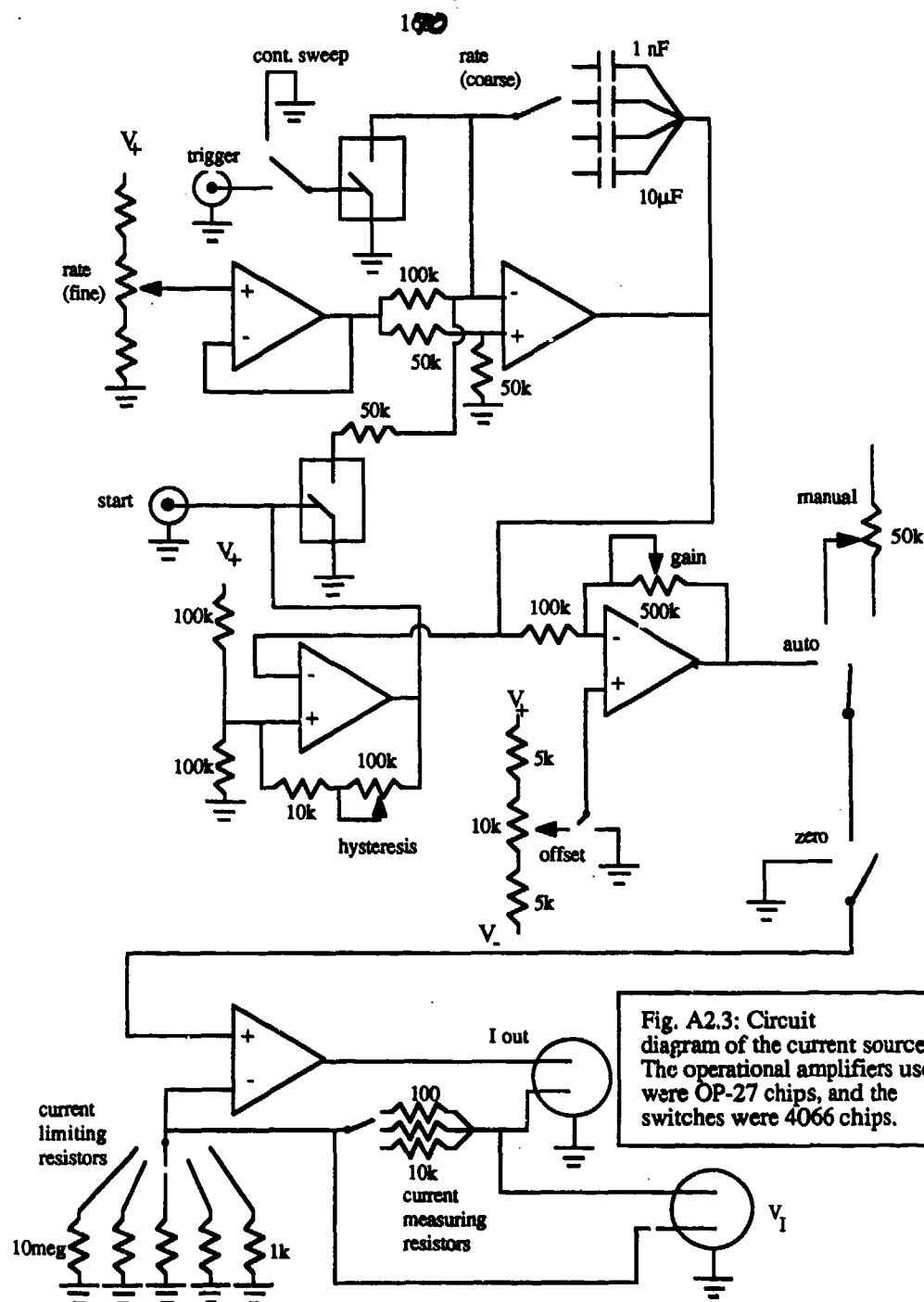


Fig. A2.2: Timing diagram for the data acquisition system.



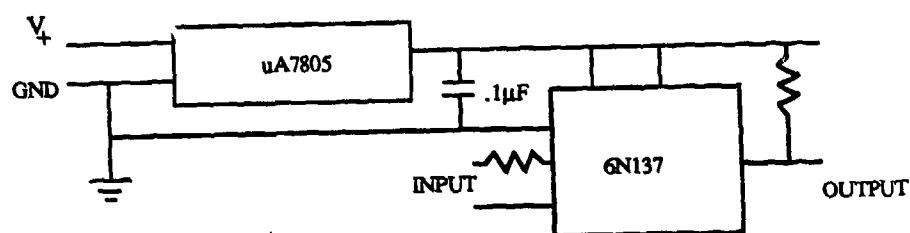


Fig. A2.4: Circuit diagram for one of the opto-isolators. The 6N137 is the opto-isolator chip, while the uA7805 is a voltage regulator.



## ACKNOWLEDGEMENTS

There is a very long list of people who share the credit for this work, and who made my graduate stay at Harvard an enjoyable and valuable experience.

First and foremost I would like to thank my wife Susan, to whom this work is dedicated, whose love, strength, and support have made this work possible. I am also very grateful to my parents, for their love and relentless encouragement. I wouldn't have made it without their help.

I feel I have been extremely fortunate to work with Prof. Michael Tinkham. He has been my advisor for many years, and has been a powerful and kind figure in my life. I believe I have learned a tremendous amount from him, both professionally and personally. Prof. Christopher J. Lobb has been a great supporter and challenger. His candid feedback has stimulated my drive and carried me through a number of difficult times.

Many of the accomplishments of this thesis are shared with other members of the Tinkham/Lobb research group. Charlie Johnson has been a good friend and a stimulating collaborator. His lithographic expertise and keen physical insight have been a great help in this work. Walter Smith's wry smile (it's there, behind the beard!) has at times been almost as much help as his invaluable proficiency with the dilution refrigerator. Gabe Spalding and Sam Benz have contributed greatly to the laboratory facilities used in this work, and have provided me with encouragement and advice. Martin Forrester and Li Ji have been great office mates, patiently tolerating the tidal wave of preprints which constantly covers my desk.

I am also very grateful to a number of visitors and old Tinkham students: Greg Blonder, who gave me a lot of valuable advice when I was an undergraduate, and introduced me to the Tinkham group. Bill Danchi and Juan Aponte, who patiently provided my first instruction on how to use the clean room. Jörn Bindslev Hansen, who

was a great source of encouragement, and helped me to measure my first tunnel junction, back in 1983. Miguel Octavio, who was (and is) a continuous source of ideas, and taught me most of what I know about nonlinear dynamics. Finally, I would like to thank Horst Rogalla, who was a major force in building a new generation of equipment in our laboratory.

I gratefully acknowledge the support of the National Science Foundation (grant DMR-84-04489), the Office of Naval Research (contract N00014-83-K 0383), and the Joint Services Electronics Program (contract N00014-84-K-0465).